HIGH-ORDER UNSTAGGERED CONSTRAINED TRANSPORT METHODS FOR MAGNETOHYDRODYNAMIC EQUATIONS

By

Qi Tang

A DISSERTATION

Submitted to
Michigan State University
in partial fulfillment of the requirements
for the degree of

Applied Mathematics – Doctor of Philosophy

2015

ABSTRACT

HIGH-ORDER UNSTAGGERED CONSTRAINED TRANSPORT METHODS FOR MAGNETOHYDRODYNAMIC EQUATIONS

By

Qi Tang

The ideal magnetohydrodynamic (MHD) equations are one of the most important plasma models. The equations model the dynamics of a perfectly conducting quasi-neutral plasma and provide evolution equations for the macroscopic quantities of mass, momentum, and energy density, as well as the magnetic field. MHD have been used successfully in many plasma physics application areas, including in space weather prediction, astrophysics, as well as in laboratory plasma applications such as flows in tokamaks and stellarators. In this thesis, we focus on the development of high-order numerical methods for the ideal MHD equations and its applications.

In the first part of the thesis, we develop a class of high-order finite difference weighted essentially non-oscillatory (FD-WENO) schemes for solving the ideal MHD equations. In the proposed methods, we control divergence errors in the magnetic field by using a novel high-order constrained transport approach to solve the magnetic potential equations. The potential equations are solved using a modified version of the FD-WENO scheme developed for Hamilton–Jacobi equations. Special limiters based on artificial resistivity are also introduced to help control unphysical oscillations in the magnetic field. Several two-dimensional and three-dimensional numerical examples are presented to demonstrate the performance of the proposed method. Numerical results have shown that with such methods we are able to resolve solution structures that are only visible at much higher grid resolutions with lower-order schemes.

In the second part of the thesis, we focus on the problems involving low density and low pressure in the ideal MHD system. A maximum-principle-preserving flux limiter for scalar hyperbolic conservation laws is extended to a novel positivity-preserving limiter for the ideal MHD equations in this portion. The proposed limiter is applied to the ideal MHD schemes proposed in the first part, resulting in a high-order positivity-preserving scheme. The resulting scheme can achieve high-order accuracy, a discrete divergence-free condition and positivity of the numerical solution simultaneously. Compared to the other positivity-preserving limiter in the literature, our limiter has the advantage that there is no extra CFL restriction from the limiting steps. Numerical examples in one dimension, two dimensions and three dimensions are provided to verify the order of accuracy on smooth test problems and to show the performance when the problems involve low density and/or low pressure.

ACKNOWLEDGMENTS

I would like to begin by expressing my sincere gratitude to my advisor, Andrew Christlieb. This thesis would not have been possible without his expertise, patience, guidance and support over the past five years. His interest in new scientific problems, his insight in the area I studied and his involvement with students were greatly helpful. Learning and working under his guidance was truly an enjoyable experience.

I would like to thank Yingda Cheng for her encouragement and support during my graduate study. She was always available and provided with great ideas and kind help when I was looking for advices. I am also grateful to James Rossmanith for the opportunity to work with him. I want to thank him for his introduction to the topics related to this thesis.

I would like to thank the rest of my thesis committee: Brian O'Shea, Keith Promislow, and Jianliang Qian. I am grateful for the helpful discussions with them about the topics related to this thesis. I would also like to thank some other (previous) faculty members at MSU, including Matt Causley, Yaman Güçlü, Wei Guo, Guanghui Hu, Yuan Liu, Ben Ong, David Seal, Zhengfu Xu, and Xinghui Zhong. I would like to thank my fellow students at math department for their friendship during the last five years. The graduate school would not have been so enjoyable and colorful without them.

Last but not least, I am grateful for the support of my family and friends during the many years as a student. My deepest gratitude goes to my wife Zixuan, for bravely joining in this journey with me, and for always supporting me and loving me. I am greatly thankful to my parents, Weiming Tang and Mingzhu Zhang, for their priceless love and trust. I am also thankful to my families for their support. In particular, I would like to thank my uncle's family: Yanming Zhang and Qun Shi, as well as my two lovely cousins, Danny and Sean.

They were always there to help whenever I needed advices no matter in academic career or personal life.

TABLE OF CONTENTS

LIST OF TABLES

LIST OF FIGURES

Chapter 1

Introduction

1.1 Plasma

In physics, matter in the universe is usually classified into four states: *solid*, *liquid*, *gas* and *plasma*. The fundamental distinctions among those four states are based on difference of the strength of the bonds between the particles of the states. It is also equivalent to say the molecular interrelationships matter. A state is called *solid* if intermolecular attractions keep the molecules in fixed spatial relationships such that the binding forces are very strong. *Liquid* is the state in which the weak attractions keep molecules close, but not in fixed relationships. When molecules are relatively separated and intermolecular attractions are essentially absent, molecules are in the gaseous state. However, *plasma* is an ionized gas that occurs at very high temperatures. The atoms or molecules in this heated gas have so much kinetic energy that they are able to overcome the binding energy of the electrons. Although the transition from a gas to a plasma is not a phase transition in the thermodynamic sense, the distinct intermolecular forces by the heating process leads to the distinct properties of plasma. As a result, plasma is treated as the fourth state of matter. On Earth, the common states of matter are solid, liquid and gas, but most of the matter of the universe is found in the plasma form. For instance, stars are mostly made of plasma. In this thesis, we are generally interested in the fluid models of plasma.

1.2 Models of plasma

There are mainly two distinct types of models for plasma: *kinetic models* and *fluid models*. Both of them describe the particle locations and velocities and the electromagnetic fields in the plasma. The kinetic models describe plasma by a distribution function of particles at each point in the *phase space*, while the fluid models use macroscopic quantities such as mass density and pressure to describe plasma. In general, kinetic models are expected to be more accurate than fluid models. However it is also more computationally expensive due to its higher dimension. In this section we briefly review several kinetic and fluid models.

1.2.1 Kinetic models

In general, kinetic models refer to the methods evolving some representation of particle positions and velocities. One of the most fundamental equations to describe plasma is the *Boltzmann equation*, which describes the evolution of a probability density function $f_\alpha(t, \mathbf{x}, \mathbf{v})$. Here $f_\alpha(t, \mathbf{x}, \mathbf{v})$ is a distribution function of plasma species α in the phase space $(\mathbf{x}, \mathbf{v})$ at a given time t. Mathematically, it is written as follows:

$$\frac{\partial f_\alpha}{\partial t} + \mathbf{v} \cdot \nabla f_\alpha + \mathbf{a}_\alpha \cdot \nabla_{\mathbf{v}} f_\alpha = \left(\frac{\partial f_\alpha}{\partial t} \right)_{\text{coll}} \tag{1.1}$$

In the case where long range interactions between charged particles are described with Maxwell's equations, the acceleration $\mathbf{a}_\alpha$ is typically dependent only on the *Lorentz force* by the electromagnetic field, i.e.,

$$\mathbf{a}_\alpha = \frac{\mathbf{F}_\alpha}{m_\alpha} = \frac{q_\alpha}{m_\alpha}(\mathbf{E} + \mathbf{v} \times \mathbf{B}), \tag{1.2}$$

where m_α represents the mass of species α and q_α represents the charge of α. The term $\left(\frac{\partial f_\alpha}{\partial t}\right)_{\text{coll}}$ in (1.1) represents a general collision operator, which describes the change of plasma due to particle collisions. In particular, the *Vlasov equation* is the case when the collisions between particles are neglected, which can be resulted under certain scaling of the the Boltzmann equation. In other words, we assume $\left(\frac{\partial f_\alpha}{\partial t}\right)_{\text{coll}} = 0$ resulting in the Vlasov equation.

1.2.2 Fluid models

As we mentioned, the kinetic models are numerically expensive to solve due to the high dimension of the phase space. As a result, people simplify the high-dimensional Boltzmann equation by evaluating the moments in the velocity space ($\mathbf{v}$-space). With a proper closure for higher moments used in the process of moment evaluation, the resulting systems become the fluid models whose unknowns only depend on the independent variables of the time t and the space $\mathbf{x}$. In this subsection we briefly present a general procedure to obtain fluid models and and also review several important models of fluid models.

1.2.2.1 Equations of fluid models

In general, the unknowns in fluid models are defined by integral of moments of $\mathbf{v}$ over the velocity space. Their corresponding equations can be obtained by integral of product of the Boltzmann equation (1.1) with those $\mathbf{v}$ moments. For instance, multiplying the above equation by some function $\chi(\mathbf{v})$ and integrating over the whole $\mathbf{v}$-space, we get,

$$\int \chi \frac{\partial f_\alpha}{\partial t}\,\mathrm{d}\mathbf{v} + \int \chi \mathbf{v}\cdot\nabla f_\alpha\,\mathrm{d}\mathbf{v} + \int \chi \mathbf{a}_\alpha\cdot\nabla_{\mathbf{v}} f_\alpha\,\mathrm{d}\mathbf{v} = \int \chi \left(\frac{\partial f_\alpha}{\partial t}\right)_{\text{coll}}\mathrm{d}\mathbf{v}. \tag{1.3}$$

Rearranging the above equation as:

$$\frac{\partial}{\partial t}\int \chi f_\alpha \,\mathrm{d}\mathbf{v} + \nabla\cdot\int \chi \mathbf{v} f_\alpha \,\mathrm{d}\mathbf{v} + \int \chi(\mathbf{a}_\alpha\cdot\nabla_{\mathbf{v}})f_\alpha \,\mathrm{d}\mathbf{v} = \frac{\partial}{\partial t}\int \chi (f_\alpha)_{\mathrm{coll}}\,\mathrm{d}\mathbf{v} \tag{1.4}$$

If we define the notation $< \chi >_\alpha$ as the average over $\mathbf{v}$-space

$$< \chi >_\alpha = \int \chi \ f_\alpha \,\mathrm{d}\mathbf{v},$$

then (1.4) will become a generalized transport equation:

$$\frac{\partial}{\partial t} < \chi >_\alpha + \nabla\cdot(< \chi\mathbf{v} >_\alpha) - < (\mathbf{a}_\alpha\cdot\nabla_{\mathbf{v}})\chi >_\alpha = \frac{\partial}{\partial t}(< \chi >_\alpha)_{\mathrm{coll}} \tag{1.5}$$

As an example, if we let χ be the moments of m_α, $m_\alpha\mathbf{v}$ and $\frac{1}{2}m_\alpha\|\mathbf{v}\|^2$ respectively, we obtain three transport equations from equation (1.5):

$$\frac{\partial\rho_\alpha}{\partial t} + \nabla\cdot(\rho_\alpha\mathbf{u}_\alpha) = \Big(\frac{\partial\rho_\alpha}{\partial t}\Big)_{\mathrm{coll}} \tag{1.6}$$

$$\frac{\partial\rho_\alpha\mathbf{u}_\alpha}{\partial t} + \nabla\cdot(\rho_\alpha\mathbf{u}_\alpha\otimes\mathbf{u}_\alpha) + \nabla\cdot(\mathbf{P}_\alpha) - < \mathbf{F}_\alpha >_\alpha = \mathbf{A}_\alpha \tag{1.7}$$

$$\frac{\partial\epsilon_\alpha}{\partial t} + \nabla\cdot(\epsilon_\alpha\mathbf{u}_\alpha) + \nabla\cdot(\mathbf{P}_\alpha\cdot\mathbf{u}_\alpha) - n_\alpha q_\alpha\mathbf{u}_\alpha\cdot\mathbf{E} = M_\alpha \tag{1.8}$$

Here the fluid unknowns are the mass density $\rho_\alpha = n_\alpha m_\alpha = m_\alpha < 1 >_\alpha$, the momentum density $\rho_\alpha\mathbf{u}_\alpha = \rho_\alpha < \mathbf{v}_\alpha >_\alpha$ and the energy density ϵ_α defined by the pressure p_α and the kinetic energy,

$$\epsilon_\alpha = \frac{p_\alpha}{\gamma - 1} + \frac{1}{2}\rho_\alpha\|\mathbf{u}_\alpha\|^2.$$

with γ being the ideal gas constant. Other terms in the equations are the pressure tensor $\mathbf{P}_\alpha = m_\alpha < (\mathbf{v} - \mathbf{u}_\alpha) \otimes (\mathbf{v} - \mathbf{u}_\alpha) >_\alpha$ and the collision terms,

$$\mathbf{A}_\alpha = m_\alpha \int \mathbf{v} \left(\frac{\partial f_\alpha}{\partial t} \right)_{\text{coll}} \mathrm{d}\mathbf{v}, \qquad M_\alpha = \frac{1}{2} m_\alpha \int \|\mathbf{v}\|^2 \left(\frac{\partial f_\alpha}{\partial t} \right)_{\text{coll}} \mathrm{d}\mathbf{v}.$$

In general, this process can be extended to arbitrary number of moments of $\mathbf{v}$. To obtain a closed system, we have to cut the system for a certain number of moments. However, the transport equation of the highest moment in the resulting system will require an even higher moment in its flux function. This leads to the so-called *closure problem*, in which the flux of the highest moment needs to be approximated by all the moments in the resulting system. This approximation has to be reasonable in the sense that the system is solvable and the solution has physical meaning.

1.2.2.2 Magnetohydrodynamic model

Plasma generally involves multiple species of particles. One species will lead to one system following the procedure discussed in Section 1.2.2.1. In general, those systems influence each other through the collision operator and the electromagnetic field. The magnetohydrodynamic (MHD) equations further assume there is only one fluid in the system due to the scale of the considered problem. In other words, the unknowns in the MHD equations are the summation with respect to of the unknowns from Section 1.2.2.1, for instance, the first two

unknowns are

$$\text{mass density:} \quad \rho(t, \mathbf{x}) = \sum_{\alpha} n_\alpha m_\alpha,$$

$$\text{momentum density:} \quad \rho\mathbf{u}(t, \mathbf{x}) = \sum_{\alpha} n_\alpha m_\alpha \mathbf{u}_\alpha.$$

With the additional assumption to simplify the pressure tensor $\mathbf{P}_\alpha$ (this assumption is actually the closure condition), and no collisions on the right hand side, we can obtain three conservation equations for the mass, momentum and kinetic energy densities by simply summing the corresponding equation for each species. Those three equations are exactly the three conservation laws in the ideal MHD equations.

The last equation of the MHD equations comes from Faraday's law,

$$\frac{\partial \mathbf{B}}{\partial t} + \nabla \times \mathbf{E} = 0.$$

Different from the full Maxwell equation case, the electric field in the MHD equation is directly determined by the Ohm's law.

For instance, we could consider the case when there are only two species, ions and electrons, in the plasma. Following the process in Section 1.2.2.1, we could obtain two systems of transport equations for both species. We further assume the unknowns such as the current density $\mathbf{J}$ and the charge density ρ_c,

$$\mathbf{J} = e(n_i \mathbf{u}_i - n_e \mathbf{u}_e),$$

$$\rho_c = e(n_i - n_e).$$

Additionally, there is another important parameter. The *Debye length* λ_D is defined by the typical number density n_0 and the temperature scale T_0,

$$\lambda_D = \left(\frac{\epsilon_0 k_B T_0}{e^2 n_0} \right)^{\frac{1}{2}}.$$

In the MHD limit, the spatial scale of the problem is much larger than λ_D. From Gauss's law, it is equivalent to assume the plasma is *quasi-neutral*, i.e., $\rho_c = 0$ or $n_i = n_e = n$.

By taking the difference of two momentum transport equations, we could obtain the *generalized Ohm's law* as follows,

$$\begin{aligned} &\frac{\partial \mathbf{J}}{\partial t} + \nabla \cdot \left\{ \left(\frac{e}{m_i} p_i - \frac{e}{m_e} p_e \right) \mathbf{I} + \mathbf{u}\mathbf{J} + \mathbf{J}\mathbf{u} - \frac{\mathbf{J}\mathbf{J}}{en} \left(\frac{m_i - m_e}{m_i + m_e} \right) \right\} \\ &\quad - \frac{\rho e^2}{m_i m_e} (\mathbf{E} + \mathbf{u} \times \mathbf{B}) + \frac{e(m_i - m_e)}{m_i m_e} \mathbf{J} \times \mathbf{B} = 0, \end{aligned} \tag{1.9}$$

which can be rewritten as,

$$\begin{aligned} \mathbf{E} + \mathbf{u} \times \mathbf{B} = &\frac{m_i m_e}{\rho e^2} \left(\frac{\partial \mathbf{J}}{\partial t} + \nabla \cdot \left\{ \left(\frac{e}{m_i} p_i - \frac{e}{m_e} p_e \right) \mathbf{I} + \mathbf{u}\mathbf{J} + \mathbf{J}\mathbf{u} - \frac{\mathbf{J}\mathbf{J}}{en} \left(\frac{m_i - m_e}{m_i + m_e} \right) \right\} \right) \\ &+ \frac{m_i - m_e}{\rho e} \mathbf{J} \times \mathbf{B}. \end{aligned} \tag{1.10}$$

In the ideal MHD limit, the ratio $\frac{m_e}{m_i}$ is assumed to be very small. If we take the limit $\frac{m_e}{m_i} = 0$, the equation (1.10) can be simplified as,

$$\mathbf{E} + \mathbf{u} \times \mathbf{B} = \frac{m_e}{ne^2} \frac{\partial \mathbf{J}}{\partial t} - \frac{1}{ne} \nabla p_e + \frac{m_e}{ne^2} \nabla \cdot \left(\mathbf{u}\mathbf{J} + \mathbf{J}\mathbf{u} - \frac{\mathbf{J}\mathbf{J}}{en} \right) + \frac{1}{ne} \mathbf{J} \times \mathbf{B}. \tag{1.11}$$

In the ideal MHD limit, the right hand side of the equation (1.11) is ignored due to the spatial scale of the problem. One way to justify that is to assume the spatial scale length is

much greater than the ions' inertial length ($\frac{c}{\omega_i} = \sqrt{\frac{m_i}{\mu_0 n e^2}}$). This results in the *ideal Ohm's law*,

$$\mathbf{E} + \mathbf{u} \times \mathbf{B} = 0. \tag{1.12}$$

If other terms in (1.9) are involved in the problem, the system is generally called *extended MHD*. For example, if $\mathbf{J} \times \mathbf{B}$ (Hall term) is included, the whole system is called *Hall MHD*. In this thesis, we only focus on the ideal MHD equations and the extension to other extended MHD equations will be part of our future work.

1.2.2.3 Other fluid models

The MHD equations are still limited in their ability to fully describe a plasma. For instance, in the ideal MHD equations, the magnetic field lines move with the fluid and thus will not change its topology as time evolves. However, due to the momentum of the electrons, the the magnetic field line in many problems can break and reconnect. Since the electrons are massless in the ideal MHD, this effect is apparently beyond the limit of the ideal MHD equations. So to study the problems of this nature, such as these magnetic reconnection problems, other fluid models have been proposed and studied.

A natural generalization of the MHD equations is the *two-fluid model*, where the electrons and ions are modeled by two sets of fluid variables. Depending on the closure of the equations, the two-fluid models have several variations. If the system only evolves the energy or entropy equations separately while still using single-fluid mass and momentum density equations and Ohm's law, the whole system is often called the *two-fluid MHD equations*. However a more general case is to use the full Maxwell equation, in which case the electrons and ions are modeled by completely separate fluid variables. For two-fluid models, Johnson has a good

summary of different models in his thesis [41].

Another approach is to generalize the procedure of the Boltzmann equation to fluid models. Instead of evolving only three conservation variables, the model uses more higher moment of $\mathbf{v}$. This is often called *moment methods*. The motivation of the moment methods is that with more moments introduced, the resulting system will become a better approximation to the Boltzmann equation than the MHD system. It is advantageous that the system still has the same dimension as the MHD equations. Grad's 13-moment system [32] is one of the early works in this area. However there are many difficulties in these methods. For instance, it is generally hard to obtain a hyperbolic system by using the closure to close the system for high moment systems. Recently, there have been some increasing interest in this approach because people proposed novel approaches to close the system, e.g., [46, 72, 74]. But this approach still has a long way to go before it reaches a level of practical application.

1.3 Review of previous work

In this section, we review the previous work related to numerical methods for the MHD equations. We mainly focus on four topics: (1) numerical methods for ideal MHD, (2) adaptive mesh refinement (AMR), (3) numerical methods for the hyperbolic conservation laws, and (4) positivity-preserving limiters.

1.3.1 Numerical methods for ideal MHD

Mathematically, the ideal MHD equations are a set of nonlinear hyperbolic conservation laws with the additional restriction that the magnetic field must remain divergence-free for all time. In fact, at the continuum level, if the initial magnetic field is divergence-free, then

the ideal MHD equations propagate this condition forward for all time. Unfortunately, most standard numerical discretizations based on shock-capturing methods (e.g., finite volume, weighted essentially non-oscillatory, discontinuous Galerkin) do not propagate a discrete version of the divergence-free condition forward in time; and furthermore, there are some observations in the literature that the failure to guarantee $\nabla \cdot \mathbf{B} = 0$ to round-off error can lead to some unphysical solutions. For instance, Brackbill and Barnes [16] find the unphysical flow due to the error from $\nabla \cdot \mathbf{B}$ eventually even terminates the computation. Another example is the Rotor problem in [10] that shows the solutions will be spurious without any divergence cleaning step.

The main challenge in numerically simulating the ideal MHD system is therefore to augment existing schemes so that they satisfy a divergence-free condition of the magnetic field in some way. Roughly speaking, there are four kinds of approaches that have been proposed in the literature: (1) *the 8-wave formulation* [56, 57], (2) *projection methods* [6, 16, 75, 83], (3) *hyperbolic divergence-cleaning methods* [26], and (4) *constrained transport (CT) methods* [3, 10, 22, 25, 28, 29, 34, 51, 52, 60, 62, 71, 75, 73].

The method in [16] is probably the first approach dealing with this constraint using the classical projection method. They used *Hodge decomposition* to project the inaccurate magnetic field to the divergence-free subspace by solving a Poisson equation. However, this projection method is computationally expensive and generally difficult to extend to the AMR frameworks. There are two factors driving here, first the need arises to solve a Poisson equation each time step, second, solving the Poisson equation on an adaptive mesh can be tricky. This treatment is still very popular because of its accuracy and flexibility. For instance, Zachary *et al.* [83] splits the ideal MHD Equations into a conservative part and another advective part, treated as a source. A new Riemann solver was introduced to get

rid of most of unphysical states such as negative pressures and densities, and the projection method was used to make the magnetic field satisfy the constraint. The second approach invented by Powell in [56] is to treat the ideal MHD Equations significantly different, by adding an additional source term (it is proportional to the divergence of the magnetic field) to the MHD equations. Consequently, the original ideal MHD equations with the constraint is changed into a 8×8 hyperbolic system with a source term and no constraint. Therefore, this system is easier to solve and the resulting *8-wave scheme* is very robust and extension to an AMR framework is much easier for this method. The drawback of this approach is also very clear. The divergence is not enforced to machine precision and the new system is not conservative any more due to the additional source term. It has been observed in [75] that this non-conservation drawback can produce incorrect jumps in a rotated shock tube problem. Another class of methods is the *hyperbolic divergence-cleaning method* first proposed by Dedner *et al.* [26], which has a similar idea as the projection method. Instead of solving an elliptic equation in the projection method, a mixed hyperbolic and parabolic equation is introduced and solved for the divergence error of magnetic field. The method damps the divergence errors away, instead of getting an exact divergence-free magnetic field. The advantage of this method is that it is fully explicit, thus, efficient and fast, but the disadvantage is that it has two tunable parameters: the speed of propagation of the error and the rate at which the divergence error is damped.

In this thesis we focus on the CT methodology for producing a magnetic field that satisfies a discrete divergence-free condition. The CT method was originally introduced by Evans and Hawley [28], and, in their formulation, staggered electric and magnetic fields are used to create appropriate mimetic finite difference (FD) operators that ultimately lead to an exactly divergence-free magnetic field. Their constrained transport framework can be

thought as a modification of the popular Yee scheme [82] from electromagnetics.

Since the introduction of the CT methodology, there have been many modifications and extensions, especially in the context of high-resolution shock-capturing schemes. DeVore [27] developed a flux-corrected transport implementation of the constrained transport approach. Balsara and Spicer [10], Dai and Woodward [25], and Ryu *et al.* [62], all developed various strategies for constructing the electric field via Ohm's law in the CT framework. Londrillo and Zanna [51, 52] proposed a high-order version of the Evans and Hawley approach. De Sterck [71] developed a similar CT method on unstructured triangular grids. Balsara [1] developed from the CT framework an AMR scheme that also included a globally divergence-free magnetic field reconstruction. There is a careful description and comparison of several of these methods in the article of Tóth [75], in which he also showed that a staggered magnetic field is not necessary, and then introduced several unstaggered CT methods.

In recent years, unstaggered CT methods have attracted considerable interest due to their ease of implementation and applicability to AMR strategies. For instance, Fey and Torrilhon [29] presented a way to preserve divergence-free condition through an unstaggered upwind scheme. Rossmanith [60] developed an unstaggered CT method for the 2D MHD equations on Cartesian grids based on the wave-propagation method [45]. Helzel *et al.* [34, 35] extended this unstaggered CT method to the 3D MHD equations and to mapped grids.

In addition to the above mentioned papers, several other high-order methods have been proposed in recent years for the ideal MHD equations using a variety of discretization techniques. Balsara [4] developed a weighted essentially non-oscillatory (WENO) method for ideal MHD using a staggered magnetic field to reconstruct a globally divergence-free magnetic field. Balsara *et al.* [7, 8] developed a class of high-order ADER-WENO schemes, again using a staggered magnetic field to reconstruct a globally divergence-free magnetic field. Li

et al. [49] and Cheng *et al.* [19] introduced a class of central discontinuous Galerkin schemes that evolves the MHD equations on a primal as well as a dual mesh, and by intertwining these two updates, they showed that a globally divergence-free magnetic field could be obtained. Kawai [42] devloped a high-order finite difference method with artificial resistivity, where the finite difference operators were specifically constructed to guarantee that an appropriate definition of the magnetic field divergence is propagated forward in time by the numerical scheme.

1.3.2 Numerical methods for hyperbolic conservation laws

In this thesis, we use the *method of lines* approach to solve the hyperbolic conservation laws. The idea of this approach is first to discretize the time-involved PDEs only in space to generate a semi-discretized system of ODEs, and then to apply an ODE solver to the resulting system. Many numerical methods have been developed for spatial discretization of the conservation law over the recent decades, such as the discontinuous Galerkin method [23], the finite volume/finite difference ENO schemes [33, 69, 70], and finite volume/finite difference WENO schemes [39, 50]. Among various methods, WENO schemes are shown to be very robust and efficient especially when solutions may contain discontinuities, sharp gradient regions and other complicated solution structures. In this thesis, we use WENO method to service as a fundamental solver for the ideal MHD equations.

For the time integrators, the non-oscillatory property is desired for the problems of the conservation laws, such as Euler equations and MHD equations. Thus, strong stability preserving Runge–Kutta (SSP-RK) methods (also called total-variation-diminishing in the earlier literature) are very popular for those problems. SSP methods are higher-order methods that preserve the strong stability properties of first-order Euler time stepping for the

spatial discretization. The optimal third order SSP-RK method (SSP-RK3) is given by [69]

$$\begin{aligned} q^{(1)} &= q^n + \Delta L(q^n) \\ q^{(2)} &= \frac{3}{4}q^n + \frac{1}{4}q^{(1)} + \frac{1}{4}\Delta L(q^{(1)}) \\ q^{n+1} &= \frac{1}{3}q^n + \frac{2}{3}q^{(2)} + \frac{2}{3}\Delta L(q^{(2)}) \end{aligned} \tag{1.13}$$

In Chapter 4, we use the above SSP-RK3 method as our time integrator to design a positivity-preserving limiter. In Chapter 3, we use a low-storage fourth-order SSP-RK method to solve the problems, which is presented in the work [43].

1.3.3 Positivity-preserving limiter

Another major focus of this thesis is the design of high-order schemes that preserve the positivity of the density and pressure of the MHD system. Even with divergence-free methods, negative density or/and pressure can still be observed in numerical simulations, such as those simulating the low-β plasma. This negative quantity can lead to a complex wave speed that breaks the hyperbolicity of the system and causes the numerical simulations to break down. A lot of effort has been dedicated to addressing this issue in the literature. For instance, Balsara and Spicer [9] proposed a strategy to maintain the positivity of pressure by switching the Riemann solvers based on different wave situations. Janhunen [37] designed a new Riemann solver for the modified ideal MHD equations and demonstrated its positivity-preserving property numerically. In [76], a conservative second-order MUSCL-Hancock scheme was shown to be positivity-preserving for the 1D ideal MHD equations and the extension to multidimensional (multi-D) cases was constructed based on similar ideas as Powell's 8-wave formulation [56, 57]. Balsara [5] developed a high-order positivity-preserving scheme for ideal

MHD through limiting high-order numerical solutions by a conservative bounded solution. Another class of important methods for the ideal MHD equations is discontinuous Galerkin (DG) methods [47, 48, 49, 61, 81]. Recently, Cheng *et al.* proposed positivity-preserving DG and central DG methods for the ideal MHD equations [19], in which they generalized Zhang and Shu's positivity-preserving limiters for the compressible Euler equations [84]. In [19], it was proved that the first-order Lax-Friedrichs scheme is positivity-preserving for the 1D MHD under the restriction CFL$\leq$ 0.5. This first-order scheme also serves as the building block for the positivity-preserving limiter in this thesis.

Besides the aforementioned work for MHD equations, several high-order positivity-preserving schemes have been developed recently for compressible Euler equations. Zhang and Shu developed arbitrary-order positivity-preserving finite volume WENO and DG methods by limiting the underlying polynomials around cell averages [84]. A flux cut-off limiter was proposed by Hu *et al.* [36] for finite difference WENO schemes to maintain positivity of density and pressure for the compressible Euler equations. Recently, Xu has proposed a maximum-principle-preserving flux limiter for finite difference WENO schemes for the scalar conservation laws in [79]. This limiter has later been extended to a positivity-preserving limiter for finite difference WENO schemes [78]. In the recent work of [20], we generalized this limiter to high order finite volume WENO schemes on triangular meshes for the scalar conservation laws and Euler equations. In another recent work [65], we successfully applied the above positivity-preserving limiter to the single-step method for Euler equations [63]. The approach developed in [20, 65, 78] is novel because the parametrized limiter maintains the accuracy of the base scheme without sacrificing the CFL excessively and is more efficient than the other versions of the limiters [36, 84].

1.3.4 Adaptive mesh refinement

The AMR algorithm was first developed for hyperbolic conservation laws in [15]. The original idea is to refine the mesh around complicated solutions structure, such as shocks, resulting in a better resolution and decrease of computational effort. In [15], a fundamental framework of patch-based AMR has been established. The original method starts from a uniform rectangular mesh, using Richardson extrapolation to estimate local spacial errors to determine the refinement regions. After the regions are refines, the algorithm solves the original hyperbolic equations locally with appropriate local boundary conditions. Since the algorithm also refines time steps locally, the computation is very efficient because the CFL of the coarse meshes is not restricted by the CFL of the finer meshes.

Since then, the AMR algorithm has been very popular in a large variety of areas such as space physics, atmospheric modeling and aerospace engineering. Accompany with the applications, there are also many efforts on developing the theories of AMR algorithms. In [13], Berger and Colella investigated the global conservation of the solution in AMR, achieved by the modification of the updating flux on the interface between fine and coarse grids. Later, Bell *et al.* [12] extended this idea to 3D hyperbolic conservation laws. In [14], this patched-based AMR was also successfully combined with the finite volume wave-propagation method that was proposed by LeVeque in [45].

There have been a lot of studies of AMR algorithm in Euler Equations and MHD Equations. A package called Gerris [55] is designed for incompressible Euler Equation. The algorithm uses the fully threaded tree data structure of [44] and invented a multi-grid Poisson solver to implement the projection method based on Hodge decomposition. For MHD equations simulations, Rossmanith [59] was able to extend the unstaggered CT method to

AMRCLAW framework for 2D ideal MHD equations. Another extension of the CT methods to AMR framework was proposed by Fromang *et al.* [30], in which they use the AMR framework, MUSCL scheme and the standard CT method to evolve the induction equations in time. In [2], the CT method from [10] was also extended to AMR hierarchy by Balsara.

1.4 Outline of the thesis

In the work, we mainly consider two numerical difficulties when solving the ideal MHD equations. First, we would like to solve the ideal MHD equation in such a way as to maintain the divergence-free property of the magnetic field. Second, we would like to maintain the positivity of both density and pressure when the method is used to model any plasma problem.

In Chapter 2 we introduce the mathematical form of the ideal MHD equations. We also present its hyperbolic property by discussing its eigenvalues. We further introduce the general constrained transport method and the 2D and 3D versions of the magnetic potential equations used in this work.

In Chapter 3 we propose a class of novel finite difference schemes for the 2D and 3D magnetic potential equations. The proposed schemes are coupled with regular WENO scheme for hyperbolic conservation laws to obtain a fourth-order finite difference numerical schemes for the ideal MHD equations. The schemes successfully control the oscillations in the solutions thanks to the WENO approach and novel schemes we proposed for the magnetic potential equations. The resulting schemes are tested with several test problems, including 2D and 3D smooth Alfvén wave problems, 2D rotated shock tube problem, Orszag-Tang vortex, and 2D, 2.5D and 3D cloud-shock interaction problems.

In Chapter 4 we propose a positivity-preserving limiter for the schemes we proposed in Chapter 3. The limiter is a natural extension of a similar limiter for the Euler equations. The limiter generally has two steps: first it maintains positivity of the density by a linear process, and then it modify the flux to keep the pressure positive by a nonlinear process. After the proposed limiter is applied to the constrained transport schemes in Chapter 3, the resulting scheme can solve the problems with low density and pressure with a CFL number of 0.5. We further test it with several problems, including 1D and 2D vacuum shock tube problems, torsional Alfvén wave pulse problem, smooth vortex problems, and 2D and 3D blast problems.

Chapter 2

Ideal MHD equations

2.1 The ideal MHD equations

The ideal MHD equations in conservation form can be written as

$$\frac{\partial}{\partial t}\begin{bmatrix}\rho\\ \rho\mathbf{u}\\ \mathcal{E}\\ \mathbf{B}\end{bmatrix}+\nabla\cdot\begin{bmatrix}\rho\mathbf{u}\\ \rho\mathbf{u}\otimes\mathbf{u}+(p+\frac{1}{2}\|\mathbf{B}\|^2)\mathbf{I}-\mathbf{B}\otimes\mathbf{B}\\ \mathbf{u}(\mathcal{E}+p+\frac{1}{2}\|\mathbf{B}\|^2)-\mathbf{B}(\mathbf{u}\cdot\mathbf{B})\\ \mathbf{u}\otimes\mathbf{B}-\mathbf{B}\otimes\mathbf{u}\end{bmatrix}=0, \tag{2.1}$$

$$\nabla\cdot\mathbf{B}=0, \tag{2.2}$$

where ρ, $\rho\mathbf{u}$, and $\mathcal{E}$ are the total mass, momentum and energy densities of the system, $\mathbf{B}$ is the magnetic field, and p is the hydrodynamic pressure. The total energy density is given by

$$\mathcal{E}=\frac{p}{\gamma-1}+\frac{1}{2}\rho\|\mathbf{u}\|^2+\frac{1}{2}\|\mathbf{B}\|^2, \tag{2.3}$$

where $\gamma=5/3$ is the ideal gas constant. Here $\|\cdot\|$ is used to denote the Euclidean vector norm. A complete derivation of the MHD system (2.1)–(2.2) can be found in many standard plasma physics textbooks (e.g., pages 165–190 of [54]).

This chapter previously appeared in [22]: A.J. Christlieb, J.A. Rossmanith and Q. Tang. Finite difference weighted essentially non-oscillatory schemes with constrained transport for ideal magnetohydrodynamics. *J. Comput. Phys.,* 268: 302–325, 2014.

2.2 Hyperbolicity of the governing equations

Equations (2.1), along with the equation of state (2.3), form a system of hyperbolic conservation laws:

$$\frac{\partial q}{\partial t} + \nabla \cdot \mathbf{F}(q) = 0, \tag{2.4}$$

where $q = (\rho, \rho\mathbf{u}, \mathcal{E}, \mathbf{B})$ are the conserved variables and $\mathbf{F}$ is the flux tensor (see (2.1)). Under the assumption of positive pressure ($p > 0$) and density ($\rho > 0$), the flux Jacobian in some arbitrary direction $\mathbf{n}$ ($\|\mathbf{n}\| = 1$), $A(q; \mathbf{n}) := \mathbf{n} \cdot \frac{\partial \mathbf{F}}{\partial q}$, is a diagonalizable matrix with real eigenvalues. In particular, the eigenvalues of the flux Jacobian matrix in some arbitrary direction $\mathbf{n}$ ($\|\mathbf{n}\| = 1$) can be written as follows:

$$\lambda^{1,8} = \mathbf{u} \cdot \mathbf{n} \mp c_f \quad : \text{fast magnetosonic waves,} \tag{2.5}$$

$$\lambda^{2,7} = \mathbf{u} \cdot \mathbf{n} \mp c_a \quad : \text{Alfvén waves,} \tag{2.6}$$

$$\lambda^{3,6} = \mathbf{u} \cdot \mathbf{n} \mp c_s \quad : \text{slow magnetosonic waves,} \tag{2.7}$$

$$\lambda^{4} = \mathbf{u} \cdot \mathbf{n} \quad : \text{entropy wave,} \tag{2.8}$$

$$\lambda^{5} = \mathbf{u} \cdot \mathbf{n} \quad : \text{divergence wave,} \tag{2.9}$$

where

$$a \equiv \sqrt{\frac{\gamma p}{\rho}}, \tag{2.10}$$

$$c_a \equiv \sqrt{\frac{(\mathbf{B}\cdot\mathbf{n})^2}{\rho}}, \tag{2.11}$$

$$c_f \equiv \left\{ \frac{1}{2}\left[a^2 + \frac{\|\mathbf{B}\|^2}{\rho} + \sqrt{\left(a^2 + \frac{\|\mathbf{B}\|^2}{\rho} \right)^2 - 4a^2 \frac{(\mathbf{B}\cdot\mathbf{n})^2}{\rho}} \right] \right\}^{\frac{1}{2}}, \tag{2.12}$$

$$c_s \equiv \left\{ \frac{1}{2}\left[a^2 + \frac{\|\mathbf{B}\|^2}{\rho} - \sqrt{\left(a^2 + \frac{\|\mathbf{B}\|^2}{\rho} \right)^2 - 4a^2 \frac{(\mathbf{B}\cdot\mathbf{n})^2}{\rho}} \right] \right\}^{\frac{1}{2}}. \tag{2.13}$$

The eight eigenvalues are well-ordered in the sense that

$$\lambda^1 \le \lambda^2 \le \lambda^3 \le \lambda^4 \le \lambda^5 \le \lambda^6 \le \lambda^7 \le \lambda^8. \tag{2.14}$$

2.3 Magnetic potential in 3D

Although there are many available numerical methods for solving hyperbolic systems (e.g., finite volume, WENO, and discontinuous Galerkin) and most of them can in principle be directly used to simulate the MHD systems, the main challenge in numerically solving the MHD equations is related to the divergence-free condition on the magnetic field. First, we note that the MHD system (2.1) along with (2.3) is already a closed set of eight evolution equations. Second, we note that $\nabla \cdot \mathbf{B} = 0$ is an *involution* instead of a constraint (see page 119–128 of [24]), because if $\nabla \cdot \mathbf{B} = 0$ is satisfied initially ($t = 0$), then system (2.1) guarantees that $\nabla \cdot \mathbf{B} = 0$ is satisfied for all future time ($t > 0$). Unfortunately, most numerical discretizations of MHD do not propagate some discrete version of $\nabla \cdot \mathbf{B} = 0$ forward

in time. As has been shown repeatedly in the literature, failure to adequately control the resulting divergence errors can lead to numerical instability (see e.g., [6, 47, 56, 60, 71, 75]). To address this issue, we will make use of the magnetic potential in the numerical methods described in this work.

Because it is divergence-free, the magnetic field can be written as the curl of a magnetic vector potential:

$$\mathbf{B} = \nabla \times \mathbf{A}. \tag{2.15}$$

Furthermore, we can write the evolution equation of the magnetic field in the MHD systems (2.1) in curl form:

$$\frac{\partial \mathbf{B}}{\partial t} + \nabla \times (\mathbf{B} \times \mathbf{u}) = 0, \tag{2.16}$$

due to the following relation

$$\nabla \cdot (\mathbf{u} \otimes \mathbf{B} - \mathbf{B} \otimes \mathbf{u}) = \nabla \times (\mathbf{B} \times \mathbf{u}). \tag{2.17}$$

Using the magnetic vector potential (2.15), evolution equation (2.16) can be written as

$$\nabla \times \left\{ \frac{\partial \mathbf{A}}{\partial t} + (\nabla \times \mathbf{A}) \times \mathbf{u} \right\} = 0. \tag{2.18}$$

The relation (2.18) implies the existence of a scalar function ψ such that

$$\frac{\partial \mathbf{A}}{\partial t} + (\nabla \times \mathbf{A}) \times \mathbf{u} = -\nabla \psi. \tag{2.19}$$

In order to uniquely (at least up to additive constants) determine the additional scalar function ψ, we must prescribe some gauge condition.

After investigating several gauge conditions, Helzel et al. [34] found that one can obtain stable solutions by introducing the Weyl gauge, i.e., setting $\psi \equiv 0$. With this gauge choice, the evolution equation for the vector potential becomes

$$\frac{\partial \mathbf{A}}{\partial t} + (\nabla \times \mathbf{A}) \times \mathbf{u} = 0, \tag{2.20}$$

which can be rewritten as a non-conservative quasilinear system,

$$\frac{\partial \mathbf{A}}{\partial t} + \mathbf{N}_1 \frac{\partial \mathbf{A}}{\partial x} + \mathbf{N}_2 \frac{\partial \mathbf{A}}{\partial y} + \mathbf{N}_3 \frac{\partial \mathbf{A}}{\partial z} = 0, \tag{2.21}$$

where

$$\mathbf{N}_1 = \begin{bmatrix} 0 & -u^y & -u^z \\ 0 & u^x & 0 \\ 0 & 0 & u^x \end{bmatrix}, \mathbf{N}_2 = \begin{bmatrix} u^y & 0 & 0 \\ -u^x & 0 & -u^z \\ 0 & 0 & u^y \end{bmatrix}, \mathbf{N}_3 = \begin{bmatrix} u^z & 0 & 0 \\ 0 & u^z & 0 \\ -u^x & -u^y & 0 \end{bmatrix}. \tag{2.22}$$

One difficulty with system (2.21)–(2.22) is that it is only weakly hyperbolic [34]. In order to see this weak hyperbolicity, we start with the flux Jacobian matrix in some arbitrary direction $\mathbf{n} = (n^x, n^y, n^z)$:

$$n^x \mathbf{N}_1 + n^y \mathbf{N}_2 + n^z \mathbf{N}_3 = \begin{bmatrix} n^y u^y + n^z u^z & -n^x u^y & -n^x u^z \\ -n^y u^x & n^x u^x + n^z u^z & -n^y u^z \\ -n^z u^x & -n^z u^y & n^x u^x + n^y u^y \end{bmatrix}. \tag{2.23}$$

The eigenvalues of matrix (2.23) are

$$\lambda^1 = 0, \quad \lambda^2 = \lambda^3 = \mathbf{n} \cdot \mathbf{u}, \tag{2.24}$$

and the matrix of right eigenvectors can be written as

$$\mathbf{R} = \left[\begin{array}{c|c|c} & & \\ r^{(1)} & r^{(2)} & r^{(3)} \\ & & \end{array}\right] = \begin{bmatrix} n^x & n^y u^z - n^z u^y & u^x(\mathbf{u}\cdot\mathbf{n}) - n^x \|\mathbf{u}\|^2 \\ n^y & n^z u^x - n^x u^z & u^y(\mathbf{u}\cdot\mathbf{n}) - n^y \|\mathbf{u}\|^2 \\ n^z & n^x u^y - n^y u^x & u^z(\mathbf{u}\cdot\mathbf{n}) - n^z \|\mathbf{u}\|^2 \end{bmatrix}. \tag{2.25}$$

If we assume that $\|\mathbf{u}\| \neq 0$ and $\|\mathbf{n}\| = 1$, the determinant of matrix R is

$$\det(\mathbf{R}) = -\|\mathbf{u}\|^3 \cos(\alpha)\sin(\alpha), \tag{2.26}$$

where α is the angle between $\mathbf{n}$ and $\mathbf{u}$. In particular, there exist four degenerate directions, $\alpha = 0, \pi/2, \pi,$ and $3\pi/2$, in which the eigenvectors are incomplete. Hence, the system (2.21) is only weakly hyperbolic.

2.4 Magnetic potential in 2D

A special case of the situation described above is the MHD system in 2D. In particular, what we mean by 2D is that all eight conserved variables, $q = (\rho, \rho\mathbf{u}, \mathcal{E}, \mathbf{B})$, can be non-zero, but each depends on only three independent variables: t, x, and y. From the point-of-view of the magnetic potential, the 2D case is much simpler than the full 3D case, due to the fact

that the divergence-free condition simplifies to

$$\nabla \cdot \mathbf{B} = \frac{\partial B^x}{\partial x} + \frac{\partial B^y}{\partial y} = 0. \tag{2.27}$$

It can be readily seen that solving B^3 by any numerical scheme will not have any impact on the satisfaction of the divergence-free condition (2.27). In other words, using the magnetic potential to define B^3 is unnecessary. Instead, in the 2D case, we can write

$$B^x = \frac{\partial A^z}{\partial y} \quad \text{and} \quad B^y = -\frac{\partial A^z}{\partial x}, \tag{2.28}$$

which involves only the third component of the magnetic potential, thereby effectively reducing the magnetic *vector* potential to a *scalar* potential. Consequently, the CT method in 2D can be simplified to solving an advection equation for the third component of the vector potential:

$$\frac{\partial A^z}{\partial t} + u^x \frac{\partial A^z}{\partial x} + u^y \frac{\partial A^z}{\partial y} = 0. \tag{2.29}$$

This has the added benefit that (2.29) is *strongly* hyperbolic, unlike its counterpart in the 3D case.

2.5 General framework of CT algorithm

In the unstaggered CT method for the ideal MHD equations [35], Helzel *et al.* coupled a conservative finite volume hyperbolic solver for the MHD equations with a non-conservative finite volume solver for the vector potential equation to solve the ideal MHD systems. Using

their approach as the basic framework for our 2D and 3D schemes, the work in this paper is mainly focused on extending the 3rd-order finite volume CT method to a high-order and computationally efficient finite difference CT method but still keeping all the advantages of the unstaggered CT method. In this section, we will summarize the general unstaggered CT method briefly.

Assume the semi-discrete form of MHD equations (2.1) has a general form

$$Q'_{\mathrm{MHD}}(t) = \mathcal{L}(Q_{\mathrm{MHD}}(t)) \tag{2.30}$$

and the semi-discrete form of the evolution equation of the magnetic potential ((2.21) for 3D case and (2.29) for 2D case) has a form

$$Q'_{\mathrm{A}}(t) = \mathcal{H}(Q_{\mathrm{A}}(t), \mathbf{u}(t)) \tag{2.31}$$

where the abstract A is introduced to denote the vector potential $\mathbf{A}$ in 3D case or the scalar potential A^z in 2D case, $Q_{\mathrm{MHD}}(t)$ represents the grid function at time t of conserved quantities in the ideal MHD system and $Q_{\mathrm{A}}(t)$ represents the grid function of the magnetic potential $\mathbf{A}$ or A^z.

For simplicity, we only present the CT schemes coupled with forward Euler stepping to solve the MHD systems. When the problem is solved from the current state $t = t_n$ to a new state $t = t_{n+1}$, a single time step of the CT method consists of the following substeps:

0. Start with Q^n_{MHD} and Q^n_{A} (the solutions at t_n or the initial condition at t_0)

1. Build the right hand sides of both semi-discrete systems (2.30) and (2.31) by some

spatial discretizations and update the systems by

$$\begin{aligned} Q^*_{\text{MHD}} &= Q^n_{\text{MHD}} + \Delta t\, \mathcal{L}(Q^n_{\text{MHD}}) \\ Q^{n+1}_{\text{A}} &= Q^n_{\text{A}} + \Delta t\, \mathcal{H}(Q^n_{\text{A}}, \mathbf{u}^n) \end{aligned} \tag{2.32}$$

where $Q^*_{\text{MHD}} = (\rho^{n+1}, \rho\mathbf{u}^{n+1}, \mathcal{E}^*, \mathbf{B}^*)$, $\mathbf{B}^*$ means the predicted magnetic field without satisfying the divergence free constraint and $\mathcal{E}^*$ will be updated based on the option in Step 4.

2. Correct $\mathbf{B}^*$ by the magnetic potential Q^{n+1}_{A} at new stage by a discrete curl operator

$$\mathbf{B}^{n+1} = \nabla \times Q^{n+1}_{\text{A}} \tag{2.33}$$

3. Set the total energy density $\mathcal{E}^{n+1}$ based on the following options:

   Option 1: Keep the total energy conserved:

$$\mathcal{E}^{n+1} = \mathcal{E}^* \tag{2.34}$$

   Option 2: Keep the pressure the same after the correction of magnetic field:

$$\mathcal{E}^{n+1} = \mathcal{E}^* + \frac{1}{2}(\|\mathbf{B}^{n+1}\|^2 - \|\mathbf{B}^*\|^2) \tag{2.35}$$

   This helps preserve the positivity of the pressure for low pressure problems, which increase the stability of the numerical solver, although it sacrifices energy conservation.

Chapter 3

FD-WENO with constrained transport for ideal MHD

In this chapter, we develop a class of high-order finite difference weighted essentially non-oscillatory schemes for solving the ideal MHD equations in 2D and 3D. The philosophy of this work is to use efficient high-order WENO spatial discretizations with high-order SSP-RK time-stepping schemes. Numerical results show that with such methods we are able to resolve solution structures that are only visible at much higher grid resolutions with lower-order schemes. The key challenge in applying such methods to ideal MHD is to control divergence errors in the magnetic field. We achieve this by augmenting the base scheme with a novel high-order constrained transport approach that updates the magnetic vector potential. The predicted magnetic field from the base scheme is replaced by a divergence-free magnetic field that is obtained from the curl of this magnetic potential. The non-conservative weakly hyperbolic system that the magnetic vector potential satisfies is solved using a version of FD-WENO developed for Hamilton–Jacobi equations. The resulting numerical method is endowed with several important properties: (1) all quantities, including all components of the magnetic field and magnetic potential, are treated as point values on the same mesh (i.e., there is no mesh staggering); (2) both the spatial and temporal orders of accuracy are

This chapter previously appeared as [22]: A.J. Christlieb, J.A. Rossmanith and Q. Tang. Finite difference weighted essentially non-oscillatory schemes with constrained transport for ideal magnetohydrodynamics. *J. Comput. Phys.,* 268: 302–325, 2014.

fourth-order; (3) no spatial integration or multidimensional reconstructions are needed in any step; and (4) special limiters in the magnetic vector potential update are used to control unphysical oscillations in the magnetic field.

The outline of this chapter is as follows. In Sections 3.1-3.4, we describe different parts of the numerical discretization of the proposed method. In Section 3.1 we detail the 5th-order FD-WENO spatial discretization for the MHD system. In Section 3.2 we outline the time stepping techniques. In Section 3.3 we describe the spatial discretization of the 2D scalar potential evolution equations and the 3D vector potential equations. The numerical curl operator and its properties are then discussed in Section 3.4, which completes all the steps of our CT methods. The resulting 2D and 3D schemes are implemented and tested on several numerical examples in Section 4.4.

3.1 Spatial discretization of ideal MHD

In this section, we describe the semi-discrete finite difference weighted essentially non-oscillatory scheme that comprises the *base scheme* in the constrained transport framework described in Section 2.5. Our method of choice is the FD-WENO method developwed by Jiang and Wu [40]. We will refer to this method as the WENO-HCL[1] scheme. In what follows, we describe the basic WENO-HCL scheme in one space dimension for the ideal MHD equations. We then briefly discuss the straightforward extension to higher dimensions.

We write the MHD system (2.1) in 1D as follows:

$$\frac{\partial q}{\partial t} + \frac{\partial \mathbf{f}(q)}{\partial x} = 0, \tag{3.1}$$

[1]WENO-HCL := Weighted Essentially Non-Oscillatory for Hyperbolic Conservation Laws.

where

$$q = (\rho, \rho u^x, \rho u^y, \rho u^z, \mathcal{E}, B^x, B^y, B^z)^T, \tag{3.2}$$

$$\begin{aligned}\mathbf{f}(q) = \Bigg(&\rho u^x, \rho u^x u^x + p + \frac{1}{2}\|\mathbf{B}\|^2 - B^x B^x, \rho u^x u^y - B^x B^y, \rho u^x u^z - B^x B^z, \\ &u^x \left(\mathcal{E} + p + \frac{1}{2}\|\mathbf{B}\|^2\right) - B^x(\mathbf{u}\cdot\mathbf{B}), 0, u^x B^y - u^y B^x, u^x B^z - u^z B^x\Bigg)^T.\end{aligned} \tag{3.3}$$

For convenience, we also introduce

$$w = (\rho, u^x, u^y, u^z, p, B^x, B^y, B^z)^T \tag{3.4}$$

to denote the vector of primitive variables.

Due to the hyperbolicity of the MHD systems, the flux Jacobian matrix $\frac{\partial \mathbf{f}}{\partial q}$ has a spectral decomposition of the form

$$\frac{\partial \mathbf{f}}{\partial q} = \mathbf{R}\mathbf{\Lambda}\mathbf{L}, \tag{3.5}$$

where $\mathbf{\Lambda}$ is the diagonal matrix of real eigenvalues, $\mathbf{R}$ is the matrix of right eigenvectors and $\mathbf{L} = \mathbf{R}^{-1}$ is the matrix of left eigenvectors.

We consider the problem on a uniform grid with $N+1$ grid points as follows:

$$a = x_{\frac{1}{2}} < x_{\frac{3}{2}} < \cdots < x_{N+\frac{1}{2}} = b, \tag{3.6}$$

and we denote

$$I_i = [x_{i-\frac{1}{2}}, x_{i+\frac{1}{2}}], \qquad x_i = \frac{1}{2}(x_{i-\frac{1}{2}} + x_{i+\frac{1}{2}}), \qquad \Delta x_i = \Delta x = \frac{b-a}{N}.$$

Let $q_i(t)$ denote the approximate solution of the MHD system at the point $x = x_i$. The WENO-HCL scheme for system (3.1) can be written in the following flux-difference form:

$$\frac{dq_i(t)}{dt} = \frac{1}{\Delta x}\left(\hat{\mathbf{F}}_{i+\frac{1}{2}} - \hat{\mathbf{F}}_{i-\frac{1}{2}}\right). \tag{3.7}$$

To obtain the numerical flux, $\hat{\mathbf{F}}_{i+\frac{1}{2}}$, in the above semi-discrete form, the following WENO procedure is used:

1. Compute the physical flux at each grid point:

$$\mathbf{f}_i = \mathbf{f}(q_i). \tag{3.8}$$

2. At each $x_{i+\frac{1}{2}}$:

   (a) Compute the average state $w_{i+\frac{1}{2}}$ in the primitive variables:

$$w_{i+\frac{1}{2}} = \frac{1}{2}\left(w_i + w_{i+1}\right). \tag{3.9}$$

   (b) Compute the right and left eigenvectors of the flux Jacobian matrix, $\frac{\partial \mathbf{f}}{\partial q}$, at $x = x_{i+\frac{1}{2}}$:

$$\mathbf{R}_{i+\frac{1}{2}} = \mathbf{R}\left(w_{i+\frac{1}{2}}\right) \quad \text{and} \quad \mathbf{L}_{i+\frac{1}{2}} = \mathbf{L}\left(w_{i+\frac{1}{2}}\right), \tag{3.10}$$

   where $\mathbf{L}_{i+\frac{1}{2}} = \mathbf{R}^{-1}_{i+\frac{1}{2}}$.

(c) Project the solution and physical flux into the right eigenvector space:

$$V_j = \mathbf{L}_{i+\frac{1}{2}}\, q_j \quad \text{and} \quad \mathbf{G}_j = \mathbf{L}_{i+\frac{1}{2}}\, \mathbf{f}_j, \tag{3.11}$$

for all j in the numerical stencil associated with $x = x_{i+\frac{1}{2}}$. In the case of the fifth-order FD-WENO scheme: $j = i-2, i-1, i, i+1, i+2, i+3$.

(d) Perform a Lax-Friedrichs flux vector splitting for each component of the characteristic variables. Specifically, assume that the m^{th} components of V_j and $\mathbf{G}_j$ are v_j and g_j, respectively, then compute

$$g_j^{\pm} = \frac{1}{2}\left(g_j \pm \alpha^{(m)} v_j\right), \tag{3.12}$$

where

$$\alpha^{(m)} = \max_k \left|\lambda^{(m)}(q_k)\right| \tag{3.13}$$

is the maximal wave speed of the m^{th} component of characteristic variables over all grid points. Note that the eight eigenvalues for ideal MHD are given in Section 2.2.

(e) Perform a WENO reconstruction on each of the computed flux components $g_j^{\pm}$ to obtain the corresponding component of the numerical flux. If we let Φ_{WENO5} denote the fifth-order WENO reconstruction operator (see Appendix for a detailed

description), then the flux is computed as follows:

$$\hat{g}^{+}_{i+1/2} = \Phi_{\text{WENO5}}\left(g^{+}_{i-2}, g^{+}_{i-1}, g^{+}_{i}, g^{+}_{i+1}, g^{+}_{i+2}\right), \tag{3.14}$$

$$\hat{g}^{-}_{i+1/2} = \Phi_{\text{WENO5}}\left(g^{-}_{i+3}, g^{-}_{i+2}, g^{-}_{i+1}, g^{-}_{i}, g^{-}_{i-1}\right). \tag{3.15}$$

Then set

$$\hat{g}_{i+\frac{1}{2}} = \hat{g}^{+}_{i+\frac{1}{2}} + \hat{g}^{-}_{i+\frac{1}{2}}, \tag{3.16}$$

where $\hat{g}_{i+\frac{1}{2}}$ is the m^{th} component of $\hat{\mathbf{G}}_{i+\frac{1}{2}}$.

(f) Project the numerical flux back to the conserved variables

$$\hat{\mathbf{F}}_{i+\frac{1}{2}} = \mathbf{R}_{i+\frac{1}{2}}\,\hat{\mathbf{G}}_{i+\frac{1}{2}}. \tag{3.17}$$

Remark 3.1.1. *In Step (a), although one could define the average state at $x_{i+\frac{1}{2}}$ using the Roe averages developed by Cargo and Callice [18], we instead define the state at $x_{i+\frac{1}{2}}$ via simple arithmetic averages of the primitive variables (equation* (3.9)*). The arithmetic averages are computationally less expensive to evaluate than the Roe averages and produce good numerical results in practice. It was pointed out in [40] that there is little difference in the numerical results when different approaches for defining the half-grid state are used in the base WENO scheme.*

Remark 3.1.2. *In Step (b) there are several different versions of right eigenvectors scalings [11, 17, 56, 57]. In this work we make use of the eigenvector scaling based on entropy variables proposed by Barth [11]. This approach is advantageous in that it is relatively simple*

to implement and gives the optimal direction-independent matrix norm of the eigenvector matrix.

Remark 3.1.3. *In Step (d) we use a global Lax-Friedrichs flux splitting, meaning that the* $\alpha^{(m)}$*'s are computed as the maximum of the* m^{th} *eigenvalue over the entire mesh. One could just as easily use a local Lax-Friedrichs flux splitting and only maximize the eigenvalue over the stencil on which the flux is defined. In all of the numerical test problems attempted in this work, we found no significant differences between the global and local approaches. In some applications where the eigenvalue changes dramatically in different regions of the computational domain it may be advantageous to switch to the local Lax-Friedrichs approach.*

In the 1D case, we find that the above WENO-HCL scheme applied to MHD can produce high-order accurate solutions for smooth problems and can accurately capture shocks without producing unphysical oscillations around discontinuities. The scheme as described so far can be easily extended to higher dimensions, simply by applying the FD-WENO definition of the numerical fluxes dimension-by-dimension.

The multi-dimensional version of the method described in this section serves as the *base scheme* for our proposed constrained transport method for ideal MHD. However, as has been well-documented in the literature, direct application of only the base scheme will lead to divergence errors in the magnetic field, which in turn will lead to numerical instabilities (e.g., see Example 4.4.2.3 in Section 4.4). In order to overcome this problem, we also need to directly evolve the magnetic potential as outlined in Section 2.5. In Section 3.3 we show how to modify the WENO-HCL scheme to create a high-order accurate numerical update for the magnetic vector potential equation, which will then be used to correct the magnetic field that is predicted by the WENO-HCL base scheme.

3.2 Temporal discretization

In this section we describe the time-stepping procedure used in this work. In our CT methods, we use 5th-order WENO-HCL as our base scheme for the semi-discrete form (3.1). However, it has been pointed out in [77] that it is linearly unstable when 5th-order WENO-HCL is coupled with forward Euler time stepping or many other 2nd-order Runge–Kutta stepping, and we find those methods show instability in the ideal MHD systems as time evolves, even for a smooth problem. Consequently, high-order SSP-RK methods are used for temporal discretization to improve numerical stability. In this work, we use the 10-stage 4th-order SSP-RK scheme with low-storage implementations (SSP-RK4) [43]:

$$
\begin{aligned}
&q^{(1)} = q^n,\ q^{(2)} = q^n,\\
&\text{for } i = 1:5\\
&\qquad q^{(1)} = q^{(1)} + \frac{1}{6}\Delta t\mathcal{L}(q^{(1)}),\\
&\text{end}\\
&q^{(2)} = \frac{1}{25}q^{(2)} + \frac{9}{25}q^{(1)},\\
&q^{(1)} = 15q^{(2)} - 5q^{(1)},\\
&\text{for } i = 6:9\\
&\qquad q^{(1)} = q^{(1)} + \frac{1}{6}\Delta t\mathcal{L}(q^{(1)}),\\
&\text{end}\\
&q^{n+1} = q^{(2)} + \frac{3}{5}q^{(1)} + \frac{1}{10}\Delta t\mathcal{L}(q^{(1)}).
\end{aligned}
$$

We remark here since the SSP-RK4 method is a convex combination of Forward Euler operators, coupling it with the CT steps turns out to be straightforward. In addition, the

corrections of $\mathbf{B}^*$ and $\mathcal{E}^*$ (Step 2 and 3 in Section 2.5) are performed in each stage of SSP-RK4 in this work. For smooth problems, this overall procedure gives a solution of 4th-order accuracy in time. This will be confirmed numerically by convergent studies in Section 4.4. The readers are referred to [35] for more details of the CT methods coupled with Runge–Kutta time stepping.

When solving 1D shock-tube problem [17], we find SSP-RK4 coupled with WENO performs very well for the CFL number up to 4.5. In Section 4.4, we use a CFL number of 3.0 for most of the numerical examples and obtain satisfactory results. The 4-stage 4th-order non-TVD/SSP Runge–Kutta method (RK44) is also coupled with WENO for ideal MHD systems in [40]. The typical CFL number of RK44 is 0.8 in that method. Consequently, even through SSP-RK4 has 10 stages, which is more than what RK44 has, SSP-RK4 is still more efficient than RK44 due to a much larger CFL number in SSP-RK4. Besides, any non-TVD/SSP time stepping has a risk to introduce more spurious oscillations than SSP time stepping, which is important for problems involving shocks and discontinuities in the MHD systems. Another important feature of SSP-RK4 is its low-storage property, which will be a great advantage for a 3D simulations or GPU implementation. Due to the above reasons, we choose SSP-RK4 as our time integrator in this work.

3.3 Spatial discretization of the magnetic potential equation

In this section we discuss a novel approach for discretizing the magnetic potential equations in 2D and 3D. There are two main challenges in obtaining such discretizations: (1) we must design a high-order finite difference method capable of solving the non-conservative

and weakly hyperbolic system that the magnetic potential satisfies; and (2) we must design appropriate limiting strategies that act on the update for the magnetic potential, but which control unphysical oscillations in the magnetic field. The approach we develop is a modification of the WENO method of Jiang and Peng [38], which was designed for Hamilton–Jacobi equations. We begin by describing the 1D version of WENO scheme of Jiang and Peng [38], then show how to modify this approach to solve the scalar 2D magnetic potential equation (2.29), and finally describe how to generalize this to the more complicated systems 3D magnetic potential equation (2.21).

3.3.1 WENO for 1D Hamilton–Jacobi

Consider a 1D Hamilton–Jacobi equation of the form

$$\frac{\partial q}{\partial t} + H\left(t, x, q, \frac{\partial q}{\partial x}\right) = 0, \tag{3.18}$$

where q is a scalar solution to the equation and H is the Hamiltonian. Jiang and Peng [38] developed a semi-discrete approximation to (3.18) of the following form:

$$\frac{dq_i(t)}{dt} = -\hat{H}\left(t, x_i, q_i, q_{xi}^-, q_{xi}^+\right), \tag{3.19}$$

where $\hat{H}$ is the numerical Hamiltonian and is consistent with H in the following sense:

$$\hat{H}\left(t, x, q, u, u\right) = H\left(t, x, q, u\right), \tag{3.20}$$

and q^-_{xi} and q^+_{xi} are left and right-sided approximations of $\frac{\partial q}{\partial x}$ at $x = x_i$. The values of q^-_{xi} and q^+_{xi} are obtained by performing WENO reconstruction as follows:

$$q^-_{xi} = \Phi_{\text{WENO5}}\left(\frac{\Delta^+ q_{i-3}}{\Delta x}, \frac{\Delta^+ q_{i-2}}{\Delta x}, \frac{\Delta^+ q_{i-1}}{\Delta x}, \frac{\Delta^+ q_i}{\Delta x}, \frac{\Delta^+ q_{i+1}}{\Delta x}\right), \tag{3.21}$$

$$q^+_{xi} = \Phi_{\text{WENO5}}\left(\frac{\Delta^+ q_{i+2}}{\Delta x}, \frac{\Delta^+ q_{i+1}}{\Delta x}, \frac{\Delta^+ q_i}{\Delta x}, \frac{\Delta^+ q_{i-1}}{\Delta x}, \frac{\Delta^+ q_{i-2}}{\Delta x}\right), \tag{3.22}$$

where

$$\Delta^+ q_i := q_{i+1} - q_i, \tag{3.23}$$

and Φ_{WENO5} uses the same formula as the one for WENO-HCL (see Appendix). The difference here is that the reconstructions (3.21) and (3.22) are applied to the central derivative of the solution q, while the reconstruction in WENO-HCL is applied to the fluxes on grid points. The new reconstruction helps us control unphysical oscillations in $\frac{\partial q}{\partial x}$ not q. This is in an important distinction since with Hamilton–Jacobi we are solving for a potential, the derivatives of which produce a physical variable.

As described in detail in Appendix, the WENO reconstruction formulas, Φ_{WENO5}, depend on smoothness indicators, β, that control how much weight to assign the different finite difference stencils. In the standard WENO-HCL framework, the weights are chosen so as to control unphysical oscillations in the conserved variables. In WENO-HCL the smoothness indicator is computed as follows [39]:

$$\beta_j = \sum_{\ell=1}^{k} \Delta x^{2\ell-1} \int_{x_{i-\frac{1}{2}}}^{x_{i+\frac{1}{2}}} \left(\frac{d^\ell}{dx^\ell} p_j(x)\right)^2 dx, \tag{3.24}$$

where p_j is an interpolating polynomial of the values q_i in some stencil and k is the degree of p_j. Note that the smoothness indicator is computed by including the normalized total variation of the first derivatives of p_j (i.e., the $\ell = 1$ term), leading to an essentially non-oscillatory solution q_i. However, β_j could be dominated by the total variation of $\frac{d}{dx}p_j(x)$, which is not important in controlling the oscillation of $\frac{\partial q}{\partial x}$.

Based on the above observation about WENO reconstruction, we realize if the reconstruction is applied to $\frac{\Delta^+ q_i}{\Delta x}$ as in (3.21) and (3.22), the new p_j becomes an interpolating polynomial of $\frac{\partial q}{\partial x}$. The same smoothness indicator formula (3.24) evaluates the smoothness of the interpolating polynomial of $\frac{\partial q}{\partial x}$ in this case. So if $\frac{\partial q}{\partial x}$ is not smooth, this procedure will approximate the derivative $q_{xi}^{\pm}$ by essentially using the stencil that has the smoothest derivative. In other words, the oscillations in $\frac{\partial q}{\partial x}$ can be controlled. A similar idea is used in the method of Rossmanith [60], where a TVD limiter is applied to wave differences instead of waves so as to control the oscillation in the computed solution derivatives.

Finally, in order to evaluate the numerical Hamiltonian, $\hat{H}$, Jiang and Peng [38] introduced a Lax-Friedrichs-type definition:

$$\hat{H}\left(t, x, u^-, u^+\right) = H\left(t, x, \frac{u^- + u^+}{2}\right) - \alpha\left(\frac{u^+ - u^-}{2}\right), \tag{3.25}$$

where

$$\alpha = \max_{u \in I(u^-, u^+)} \left|\frac{\partial H}{\partial u}(t, x, q, u)\right|, \tag{3.26}$$

where $I(u^-, u^+)$ is the interval between u^- and u^+.

We refer to the scheme discussed in this section as the WENO-HJ scheme. To compare

the WENO-HJ scheme with the WENO-HCL scheme, we consider a simple test problem on which both WENO-HJ and WENO-HCL can be applied. We consider the 1D linear constant coefficient advection equation,

$$\frac{\partial q}{\partial t} + \frac{\partial q}{\partial x} = 0, \tag{3.27}$$

on $x \in [0, 1]$ with the periodic boundary condition and the following piecewise linear initial condition:

$$q(0,x) = \begin{cases} 0 & \text{if} \quad 0.00 \le x \le 0.25, \\ (x - 0.25)/0.075 & \text{if} \quad 0.25 \le x \le 0.40, \\ 2 & \text{if} \quad 0.40 \le x \le 0.60, \\ (0.75 - x)/0.075 & \text{if} \quad 0.60 \le x \le 0.75, \\ 0 & \text{if} \quad 0.75 \le x \le 1.00. \end{cases} \tag{3.28}$$

This problem was considered by Rossmanith [60], where it was also used to test a limiter especially designed to control oscillations in the derivative of q.

The solutions and their numerical derivatives computed by WENO-HCL and WENO-HJ schemes are presented in Figure 3.1. Both approaches use fifth-order WENO reconstruction in the spatial discretization and SSP-RK4 for the time integrator. We use a CFL number of 1.0 and compute the solution to $t = 4$. Shown in this figure are 3.1 (a) the solution obtained by the WENO-HCL scheme on a mesh with $N = 300$, 3.1(b) the derivative of this solution as computed with a fourth-order central difference approximation, 3.1(c) the solution obtained by the WENO-HJ scheme on a mesh with $N = 300$, and 3.1(d) the derivative of this solution as computed with a fourth-order central difference approximation. Although both solutions

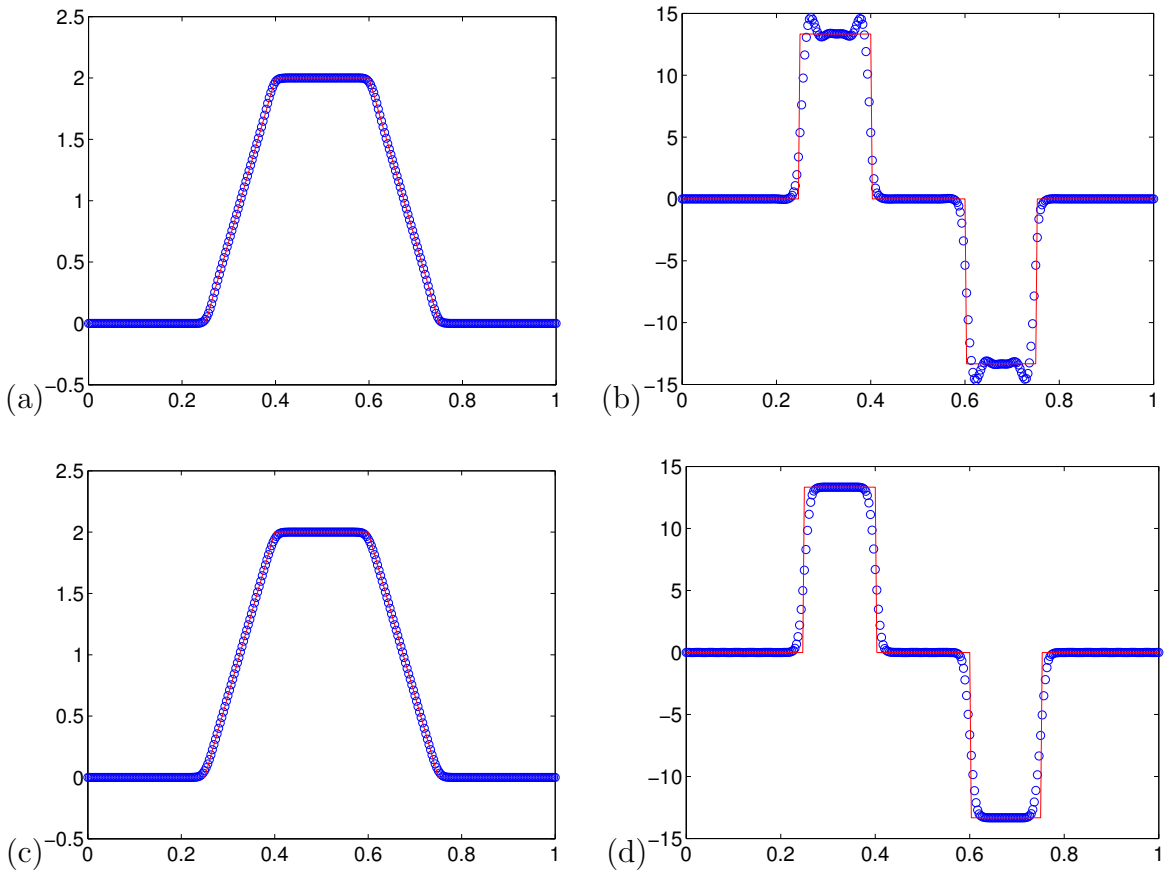

Figure 3.1: 1D advection equation. Shown in these panels are (a) the solution obtained by the WENO-HCL scheme with (b) its derivative, and (c) the solution obtained by the WENO-HJ scheme with (d) its derivative. *For interpretation of the references to color in this and all other figures, the reader is referred to the electronic version of this dissertation.*

agree with the exact solution very well, the computed derivative $\frac{\partial q}{\partial x}(4, x)$ of WENO-HCL is much more oscillatory than that of WENO-HJ. The proposed WENO-HJ scheme is able to control unphysical oscillations both in the solution and its derivative. The result of our new approach is comparable to that of existing finite volume approaches [34, 35, 60].

3.3.2 2D magnetic potential equation

In the CT framework described in Section 2.5, during Step 1 we must update the magnetic potential by solving a discrete version of

$$\frac{\partial A^z}{\partial t} + u^x(x,y)\,\frac{\partial A^z}{\partial x} + u^y(x,y)\,\frac{\partial A^z}{\partial y} = 0, \tag{3.29}$$

where, as described in Section 2.5, the velocity components are given functions from the previous time step (or time stage in the case of higher-order time-stepping). Because u^x and u^y are given, we can view (3.29) as a Hamilton–Jacobi equation:

$$\frac{\partial A^z}{\partial t} + H\left(x, y, \frac{\partial A^z}{\partial x}, \frac{\partial A^z}{\partial y}\right) = 0, \tag{3.30}$$

with Hamiltonian:

$$H\left(x, y, \frac{\partial A^z}{\partial x}, \frac{\partial A^z}{\partial y}\right) = u^x(x,y)\,\frac{\partial A^z}{\partial x} + u^y(x,y)\,\frac{\partial A^z}{\partial y}. \tag{3.31}$$

To solve this equation we can directly apply a two-dimensional version of the WENO-HJ scheme described above (just as with WENO-HCL, the 2D version of WENO-HJ is simply a direction-by-direction version of the 1D scheme). The 2D semi-discrete WENO-HJ can be written as

$$\begin{aligned}
\frac{dA^z_{ij}(t)}{dt} &= -\hat{H}\left(A^{z-}_{xij}, A^{z+}_{xij}, A^{z-}_{yij}, A^{z+}_{yij}\right) \\
&= -u^x_{ij}\left(\frac{A^{z-}_{xij} + A^{z+}_{xij}}{2}\right) - u^y_{ij}\left(\frac{A^{z-}_{yij} + A^{z+}_{yij}}{2}\right) \\
&\quad + \alpha^1\left(\frac{A^{z+}_{xij} - A^{z-}_{xij}}{2}\right) + \alpha^2\left(\frac{A^{z+}_{yij} - A^{z-}_{yij}}{2}\right),
\end{aligned} \tag{3.32}$$

where

$$\alpha^1 = \max_{i,j} \left| u_{ij}^x \right| \quad \text{and} \quad \alpha^2 = \max_{i,j} \left| u_{ij}^y \right|.$$

The approximations $A_{xij}^{3\pm}$ and $A_{yij}^{3\pm}$ are calculated with formulas analogous to (3.21) and (3.22). α^1 and α^2 are chosen as the maximal value over all grid points based on a similar idea of the Lax-Friedrichs flux splitting in Section 3.1. We remark here the scheme (3.32) with this global α^m can be too dissipative for certain pure linear Hamilton–Jacobi equations. Another obvious choice is to evaluate α^m by taking the maximal value on the local stencil. Although this local version of α^m can be much less dissipative for a certain pure Hamilton–Jacobi equation, in numerical experiments for MHD we find that the differences between the local and global approaches are negligible. Therefore, we will only present the numerical results by the global version of α^m in the numerical examples section (Section 4.4).

Except for the last remaining detail about how the discrete curl of A^z is computed (see Section 3.4), this version of the WENO-HJ scheme coupled with the WENO-HCL scheme as the base scheme completes our 2D finite difference WENO constrained transport method. In the numerical examples section, Section 4.4, we will refer to this full scheme as WENO-CT2D.

3.3.3 3D magnetic potential equation

The evolution equation of the magnetic potential (2.21) in 3D is significantly different from the evolution equation of the scalar potential (2.29) in 2D, and hence the scheme discussed in Section 3.3.2 cannot be used directly. As pointed out in Section 2.3, a key difficulty is the weak hyperbolicity of system (2.21). Helzel *et al.* [34] found that the weak hyperbolicity of

(2.21) is only an artifact of freezing the velocity in time, i.e., the full MHD system is still strongly hyperbolic. Furthermore, they found that the magnetic vector potential system can be solved by an operator split finite volume scheme with an additional limiting strategy added in certain directions. Helzel *et al.* [35] handled the weakly hyperblic system (2.21) through a path-conserving finite volume WENO scheme without appeal to operator splitting.

In order to explain the scheme advocated in this work, we take inspiration from the operator split method of Helzel *et al.* [34] and separate system (2.21) into two sub-problems:

Sub-problem 1:

$$\begin{aligned}
&\frac{\partial A^x}{\partial t} + u^y \frac{\partial A^x}{\partial y} + u^z \frac{\partial A^x}{\partial z} = 0, \\
&\frac{\partial A^y}{\partial t} + u^x \frac{\partial A^y}{\partial x} + u^z \frac{\partial A^y}{\partial z} = 0, \\
&\frac{\partial A^z}{\partial t} + u^x \frac{\partial A^z}{\partial x} + u^y \frac{\partial A^z}{\partial y} = 0.
\end{aligned} \tag{3.33}$$

Sub-problem 2:

$$\begin{aligned}
&\frac{\partial A^x}{\partial t} - u^y \frac{\partial A^y}{\partial x} - u^z \frac{\partial A^z}{\partial x} = 0, \\
&\frac{\partial A^y}{\partial t} - u^x \frac{\partial A^x}{\partial y} - u^z \frac{\partial A^z}{\partial y} = 0, \\
&\frac{\partial A^z}{\partial t} - u^x \frac{\partial A^x}{\partial z} - u^y \frac{\partial A^y}{\partial z} = 0.
\end{aligned} \tag{3.34}$$

We emphasis here that our final scheme will not contain any operator splitting, and that the division of the magnetic potential evolution equation into the above two sub-problems is only for the purpose of exposition.

The first sub-problem is a combination of three independent evolution equations, each of which has the same mathematical form as the 2D scalar evolution equation (3.29). Further-

more, this sub-problem is strongly hyperbolic. Thus, at least for this sub-problem, we can simply use the WENO-HJ scheme described in Section 3.3.2 to solve these three equations independently.

The second sub-problem, (3.34), is only weakly hyperbolic. For this problem we apply a WENO finite difference discretization using arithmetic averages to define solution derivatives at grid points. For instance, for the first component A^x in (3.34), the semi-discrete form becomes

$$\frac{d}{dt}A^x_{ijk}(t) = u^y_{ijk}\left(\frac{A^{y-}_{xijk} + A^{y+}_{xijk}}{2}\right) + u^z_{ijk}\left(\frac{A^{z-}_{xijk} + A^{z+}_{xijk}}{2}\right), \tag{3.35}$$

where $A^{\alpha\pm}_{xijk}$ again uses the WENO reconstruction given by (3.21)–(3.22). The semi-discrete forms for the other components in (3.34) are similar.

Note that semi-discrete formula (3.35) lacks the numerical dissipation terms found in (3.32). This is due to the fact that system (3.34) (by itself) does not represent a transport equation. Therefore, the above described discretizations for (3.33) and (3.34) generally do not introduce sufficient numerical resistivity in order to control unphysical oscillations in the magnetic field for a 3D problem. To be more precise, when solving system (3.33), artificial resistivity is introduced from the WENO upwinding procedure (see formula (3.32)), but only in 2 of the 3 coordinate directions (e.g., for A^z there is artificial resistivity in the x and y-directions). When solving system (3.34), no additional artificial resistivity is introduced (e.g., see (3.35)). This lack of numerical dissipation was also pointed out by Helzel *et al.* [34, 35]; they introduced explicit artificial resistivity terms into the magnetic vector potential equation. We follow a similar approach by modifying sub-problem (3.34) as follows:

Sub-problem 2 with artificial resistivity:

$$\begin{aligned}
\frac{\partial A^x}{\partial t} - u^y\frac{\partial A^y}{\partial x} - u^z\frac{\partial A^z}{\partial x} &= \varepsilon^1\frac{\partial^2 A^x}{\partial x^2},\\
\frac{\partial A^y}{\partial t} - u^x\frac{\partial A^x}{\partial y} - u^z\frac{\partial A^z}{\partial y} &= \varepsilon^2\frac{\partial^2 A^y}{\partial y^2},\\
\frac{\partial A^z}{\partial t} - u^x\frac{\partial A^x}{\partial z} - u^y\frac{\partial A^y}{\partial z} &= \varepsilon^3\frac{\partial^2 A^z}{\partial z^2}.
\end{aligned} \tag{3.36}$$

These additional terms give us artificial resistivity in the missing directions (e.g., the equation for A^z now has an artificial resistivity term in the z-direction). In the above expression, the artificial resistivity is take to be of the following form:

$$\varepsilon^1 = 2\nu\gamma^1\frac{\Delta x^2}{\delta + \Delta t}, \tag{3.37}$$

where $0 \leq \delta \ll 1$ is small parameter that can be set to ensure that ε^1 remains bounded as $\Delta t \to 0^+$, γ^1 is the smoothness indicator of A^x, and ν is a constant used to control the magnitude of the artificial resistivity.

In all the simulations presented in this work, we take $\delta = 0$ (Δt and Δx have the same order of magnitude for all the problems considered in this work). The smoothness indicator γ^1 is computed as follows:

$$\gamma^1_{ijk} = \left|\frac{a^-}{a^- + a^+} - \frac{1}{2}\right|, \tag{3.38}$$

where

$$a^- = \left\{\epsilon + \left(\Delta x\, A^{x-}_{xijk}\right)^2\right\}^{-2} \quad \text{and} \quad a^+ = \left\{\epsilon + \left(\Delta x\, A^{x+}_{xijk}\right)^2\right\}^{-2}, \tag{3.39}$$

and ϵ is taken to be 10^{-8} in all of our numerical computations. Here a^- and a^+ are used to indicate the smoothness of A^x in each of the $-$ and $+$ WENO stencils, respectively. The artificial resistivity parameters ϵ^2 and ϵ^3 in the other directions can be computed in analogous ways.

The smoothness indicator γ^i is designed such that sufficient artificial resistivity is introduced to avoid spurious oscillations in the derivatives of A^i when A^i is non-smooth, and high-order accuracy of the scheme is maintained when A^i is smooth. For the case when $\frac{\partial A^x}{\partial x}$ is smooth:

$$A^{x-}_{xijk} - A^{x+}_{xijk} = O(\Delta x^5) \quad \text{and} \quad \gamma^1_{ijk} = O(\Delta x^5).$$

In this case the artificial resistivity term in (3.36) will be of $O(\Delta x^6)$, which will not destroy the fifth-order spatial accuracy of the scheme. For the case when $\frac{\partial A^x}{\partial x}$ is non-smooth:

$$A^{x-}_{xijk} - A^{x+}_{xijk} = O(1) \quad \text{and} \quad \gamma^1_{ijk} \approx \frac{1}{2},$$

which indicates that numerical resistivity should be added. For both the smooth and non-smooth cases, we note that $\gamma^1 < \frac{1}{2}$, which means that for forward Euler time stepping, ν in the range of $[0, 0.5]$ will guarantee that the numerical scheme will be stable up to CFL $= 1$. For the fourth-order 10-stage SSP-RK4 time-stepping scheme, we found that ν in the range of $[0.02, 0.2]$ seems to satisfactorily control the unphysical oscillations in 3D problems.

The constrained transport method that we advocate in this work is a method of lines approach, and thus is not consistent with the operator splitting approach. However, through numerical experimentation, we discovered that operator splitting is not necessary to obtain

accurate and stable solutions, as long as the above artificial resistivity limiting strategy is included in the time evolution. In order to write out the final scheme as advocated, consider for brevity only the first equation in the magnetic vector potential system with artificial resistivity:

$$\frac{\partial A^x}{\partial t} - u^y \frac{\partial A^y}{\partial x} - u^z \frac{\partial A^z}{\partial x} + u^y \frac{\partial A^x}{\partial y} + u^z \frac{\partial A^x}{\partial z} = \epsilon^1 \frac{\partial^2 A^x}{\partial x^2}. \tag{3.40}$$

Using the above discussion about sub-problems 1 and 2 as a guide, we arrive at the following unsplit semi-discrete form for the full A^x evolution equation:

$$\begin{aligned} \frac{dA^x_{ijk}(t)}{dt} =& u^y_{ijk} \left(\frac{A^{y-}_{xijk} + A^{y+}_{xijk}}{2} \right) + u^z_{ijk} \left(\frac{A^{z-}_{xijk} + A^{z+}_{xijk}}{2} \right) \\ &+ 2\nu\gamma^1 \left(\frac{A^x_{i-1jk} - 2A^x_{ijk} + A^x_{i+1jk}}{\delta + \Delta t} \right) \\ &- u^y_{ijk} \left(\frac{A^{x-}_{yijk} + A^{x+}_{yijk}}{2} \right) - u^z_{ijk} \left(\frac{A^{x-}_{zijk} + A^{x+}_{zijk}}{2} \right) \\ &+ \alpha^2 \left(\frac{A^{x+}_{yijk} - A^{x-}_{yijk}}{2} \right) + \alpha^3 \left(\frac{A^{x+}_{zijk} - A^{x-}_{zijk}}{2} \right), \end{aligned} \tag{3.41}$$

where

$$\alpha^2 = \max_{i,j,k} \left| u^y_{ijk} \right|, \quad \text{and} \quad \alpha^3 = \max_{i,j,k} \left| u^z_{ijk} \right|.$$

The semi-discrete forms for A^y and A^z of the system have analogous forms. For brevity we omit these formulas.

Except for the last remaining detail about how the discrete curl of $\mathbf{A}$ is computed (see Section 3.4), this version of the WENO-HJ scheme coupled with the WENO-HCL scheme

as the base scheme completes our 3D finite difference WENO constrained transport method. In the numerical examples section, Section 4.4, we will refer to this full scheme as WENO-CT3D.

Finally, we note that the artificial resistivity terms included in the semi-discrete equation (3.41) with (3.37), (3.38), and (3.39) are specifically designed for solving the ideal MHD equations (2.1). In future work we will consider non-ideal corrections, including physical resistivity and the Hall term. In these non-ideal cases, modifications will have to be made to the artificial resistivity terms advocated in this work.

3.4 Central finite difference discretization of $\nabla \times \mathbf{A}$

During each stage of our CT algorithm, a discrete curl operator is applied to the magnetic potential to give a divergence-free magnetic field. In this section we describe the approach to approximate the curl operator and discuss its important properties.

3.4.1 Curl in 2D

We look for a discrete version of the 2D curl given by (2.28) of the following form:

$$B^x_{ij} := D^y_{ij} A^z \quad \text{and} \quad B^y_{ij} := -D^x_{ij} A^z, \tag{3.42}$$

where D^x and D^y are discrete versions of the operators $\frac{\partial}{\partial x}$ and $\frac{\partial}{\partial y}$. In particular, we look for discrete operators D^x and D^y with the property that

$$\nabla \cdot \mathbf{B}_{ij} := D^x_{ij} B^x + D^y_{ij} B^y = D^x_{ij} D^y_{ij} A^z - D^y_{ij} D^x_{ij} A^z = 0, \tag{3.43}$$

which means that we satisfy a discrete divergence-free condition. In the second order accurate, unstaggered, CT methods developed by Helzel *et al.* [34], Rossmanith [60], and Tóth [75], the obvious choice for D^x_{ij} and D^y_{ij} are second-order central finite differences. In this work, in order to maintain high-order accuracy, we replace second-order central differences with fourth-order central finite differences:

$$D^x_{ij}\, A := \frac{1}{12\Delta x}\left(A_{i-2\,j} - 8A_{i-1\,j} + 8A_{i+1\,j} - A_{i+2\,j}\right), \tag{3.44}$$

$$D^y_{ij}\, A := \frac{1}{12\Delta y}\left(A_{i\,j-2} - 8A_{i\,j-1} + 8A_{i\,j+1} - A_{i\,j+2}\right). \tag{3.45}$$

3.4.2 Curl in 3D

We look for a discrete version of the 3D curl of the following form:

$$B^x_{ijk} := D^y_{ijk}\, A^z - D^z_{ijk}\, A^y, \tag{3.46}$$

$$B^y_{ijk} := D^z_{ijk}\, A^x - D^x_{ijk}\, A^z, \tag{3.47}$$

$$B^z_{ijk} := D^x_{ijk}\, A^y - D^y_{ijk}\, A^x. \tag{3.48}$$

where $D^{\,x}$, $D^{\,y}$, and $D^{\,z}$ are discrete versions of the operators $\frac{\partial}{\partial x}$, $\frac{\partial}{\partial y}$, and $\frac{\partial}{\partial z}$. In particular, we look for discrete operators D^x, D^y, and D^z with the property that

$$\begin{aligned}
\nabla \cdot \mathbf{B}_{ijk} &:= D^x_{ijk}\, B^x + D^y_{ijk}\, B^y + D^z_{ijk}\, B^z \\
&= D^x_{ijk}\, D^y_{ijk}\, A^z - D^x_{ijk}\, D^z_{ijk}\, A^y + D^y_{ijk}\, D^z_{ijk}\, A^x \\
&- D^y_{ijk}\, D^x_{ijk}\, A^z + D^z_{ijk}\, D^x_{ijk}\, A^y - D^z_{ijk}\, D^y_{ijk}\, A^x = 0,
\end{aligned} \tag{3.49}$$

which means that we satisfy a discrete divergence-free condition. To achieve higher-order accuracy we again use fourth-order central finite differences:

$$D^x_{ijk}\, A := \frac{1}{12\Delta x}\left(A_{i-2\,jk} - 8A_{i-1\,jk} + 8A_{i+1\,jk} - A_{i+2\,jk}\right), \tag{3.50}$$

$$D^y_{ijk}\, A := \frac{1}{12\Delta y}\left(A_{i\,j-2\,k} - 8A_{i\,j-1\,k} + 8A_{i\,j+1\,k} - A_{i\,j+2\,k}\right), \tag{3.51}$$

$$D^z_{ijk}\, A := \frac{1}{12\Delta z}\left(A_{i\,j\,k-2} - 8A_{i\,j\,k-1} + 8A_{i\,j\,k+1} - A_{i\,j\,k+2}\right). \tag{3.52}$$

3.4.3 Important properties

For smooth solutions, the spatial accuracy of our overall scheme will be fourth-order accurate. This fact is confirmed via numerical experiments in Section 4.4. Furthermore, for solutions with discontinuities in the magnetic field, the fourth-order central discretization of the magnetic potential curl will introduce spurious oscillations. However, as we demonstrated via numerical experiments, we are able to control any unphysical oscillations in the magnetic fields through the limiting strategy that was designed in Section 3.3 for the WENO-HJ scheme.

Finally, we point out the following property of the proposed scheme:

Claim 3.4.1. *The constrained transport method as described in this work globally conserves the magnetic field from one Runge–Kutta stage to the next.*

Proof. Using the same idea as the proof of the conservation of $\mathbf{B}$ in Rossmanith [60], we can show the total amount of each component of $\mathbf{B}$ can be modified only through loss or gain across its physical boundary. Thus the components of the magnetic field are globally conserved. We omit the details of proof here. □

3.5 Numerical results

In this section, the 2D and 3D WENO-CT schemes are applied to several MHD problems. First, both the 2D and 3D schemes are tested on the 2D and 3D smooth Alfvén wave problems, respectively. These problems are used to demonstrate that the proposed methods are fourth-order accurate. The scheme is also tested on a rotated shock tube problem in order to examine the shock-capturing ability of the method, as well as to demonstrate the success in controlling divergence errors. Also considered are the 2D Orszag-Tang vortex problem and the 2D, 2.5D, and 3D versions of the cloud-shock interaction problem.

For all the examples computed below, the gas constant is $\gamma = 5/3$ and the CFL number is 3.0. In this section, we make exclusive use of **Option 1** and thus conserve the total energy.

3.5.1 Smooth Alfvén wave problem

We first consider 2D and 3D versions of the smooth Alfvén wave problem to demonstrate the order of accuracy of the proposed schemes.

3.5.1.1 2D problem

We perform a convergence study of the 2D scheme for the 2D smooth Alfvén wave problem. The initial conditions and the computational domain for this version are described in detail in several papers (e.g., Section 6.1.1 on page 3818 of Helzel *et al.* [34]). The L_2-errors and L_∞-errors of the magnetic field and the magnetic scalar potential are shown in Tables 3.1. Fourth-order convergence rates of all the quantities are observed when CFL = 3.0, which confirms the temporal and spatial order of accuracy.

Table 3.1: Convergence study of the 2D Alfvén wave for CFL = 3.0. Shown are the L_2-errors and L_∞-errors at time $t = 1$ of the magnetic field and magnetic potential as computed by the WENO-CT2D scheme at various grid resolutions.

Mesh	B^x				B^y			
	L_2-error	order	L_∞-error	order	L_2-error	order	L_∞-error	order
16×32	9.73e-05	-	2.70e-04	-	2.13e-04	-	5.79e-04	-
32×64	4.07e-06	4.58	1.09e-05	4.64	9.34e-06	4.51	2.47e-05	4.55
64×128	2.02e-07	4.33	4.81e-07	4.50	4.62e-07	4.34	1.09e-06	4.50
128×256	1.17e-08	4.11	2.73e-08	4.14	2.60e-08	4.15	6.06e-08	4.17
256×512	7.15e-10	4.03	1.65e-09	4.05	1.55e-09	4.07	3.62e-09	4.07
512×1024	4.44e-11	4.01	1.02e-10	4.01	9.50e-11	4.03	2.22e-10	4.02

Mesh	B^z				A^z			
	L_2-error	order	L_∞-error	order	L_2-error	order	L_∞-error	order
16×32	2.83e-04	-	7.32e-04	-	3.03e-05	-	6.98e-05	-
32×64	9.39e-06	4.91	2.59e-05	4.82	1.37e-06	4.47	3.08e-06	4.50
64×128	2.88e-07	5.03	7.94e-07	5.03	7.07e-08	4.27	1.56e-07	4.30
128×256	9.30e-09	4.95	2.50e-08	4.99	4.14e-09	4.09	9.21e-09	4.09
256×512	3.40e-10	4.77	8.13e-10	4.94	2.54e-10	4.03	5.67e-10	4.02
512×1024	1.55e-11	4.46	3.61e-11	4.49	1.58e-11	4.01	3.53e-11	4.00

3.5.1.2 3D problem

We also perform a convergence study of the 3D scheme on a 3D variant of the smooth Alfvén wave problem. The initial conditions and the computational domain for this version are described in detail in Helzel *et al.* [34] (page 3819 in Section 6.2.1). The results of the 3D scheme are presented in Tables 3.2. Fourth-order accuracy in all components are confirmed by this test problem.

Table 3.2: Convergence study of the 3D Alfvén wave for CFL = 3.0. Shown are the L_2-errors and L_∞-errors at time $t = 1$ of all the magnetic field and magnetic potential components as computed by the WENO-CT3D scheme on various grid resolutions.

Mesh	B^x				B^y			
	L_2-error	order	L_∞-error	order	L_2-error	order	L_∞-error	order
$16 \times 32 \times 32$	6.92e-05	-	3.07e-04	-	1.16e-04	-	5.47e-04	-
$32 \times 64 \times 64$	2.73e-06	4.66	1.20e-05	4.68	4.98e-06	4.54	2.10e-05	4.70
$64 \times 128 \times 128$	1.28e-07	4.41	5.09e-07	4.56	2.45e-07	4.34	9.56e-07	4.46

Mesh	B^z				A^x			
	L_2-error	order	L_∞-error	order	L_2-error	order	L_∞-error	order
$16 \times 32 \times 32$	1.06e-04	-	5.47e-04	-	6.36e-06	-	3.04e-05	-
$32 \times 64 \times 64$	4.27e-06	4.64	1.80e-05	4.93	3.31e-07	4.27	1.28e-06	4.57
$64 \times 128 \times 128$	2.07e-07	4.37	8.21e-07	4.45	1.84e-08	4.17	6.72e-08	4.25

Mesh	A^y				A^z			
	L_2-error	order	L_∞-error	order	L_2-error	order	L_∞-error	order
$16 \times 32 \times 32$	1.42e-05	-	5.24e-05	-	1.53e-05	-	6.24e-05	-
$32 \times 64 \times 64$	5.82e-07	4.61	2.24e-06	4.55	6.31e-07	4.60	2.45e-06	4.67
$64 \times 128 \times 128$	2.88e-08	4.34	1.11e-07	4.33	3.06e-08	4.37	1.16e-07	4.41

3.5.2 2D rotated shock tube problem

Next we consider a 1D shock tube problem rotated by an angle of α in a 2D domain. The initial conditions are

$$(\rho, u^\perp, u^\parallel, u^z, p, B^\perp, B^\parallel, B^z) = \begin{cases} (1, -0.4, 0, 0, 1, 0.75, 1, 0) & \text{if} \quad \xi < 0, \\ (0.2, -0.4, 0, 0, 0.1, 0.75, -1, 0) & \text{if} \quad \xi > 0, \end{cases} \tag{3.53}$$

where

$$\xi = x\cos\alpha + y\sin\alpha \quad \text{and} \quad \eta = -x\sin\alpha + y\cos\alpha, \tag{3.54}$$

and $u^\perp$ and $B^\perp$ are vector components that are perpendicular to the shock interface, and $u^\parallel$ and $B^\parallel$ are components that are parallel to the shock interface. The initial magnetic

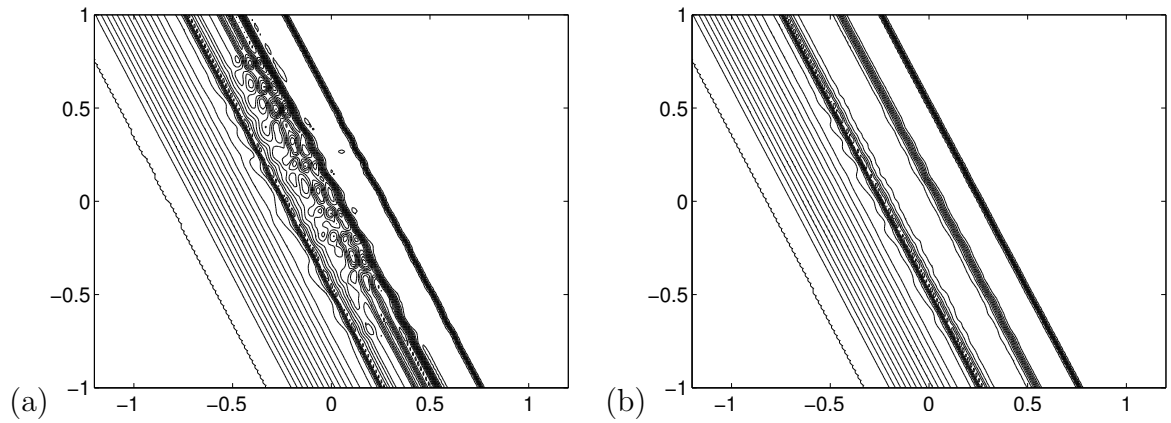

Figure 3.2: The rotated shock tube problem. Shown in these panels are ρ of (a) the base WENO scheme and (b) the WENO-CT2D scheme. 30 equally spaced contours are shown for each graph in the ranges $\rho \in [0.1795, 1]$.

potential is

$$A^z(0,\xi) = \begin{cases} 0.75\,\eta - \xi & \text{if} \quad \xi \leq 0, \\ 0.75\,\eta + \xi & \text{if} \quad \xi \geq 0. \end{cases} \tag{3.55}$$

We solve this problem on the computational domain $(x, y) \in [-1.2, 1.2] \times [-1, 1]$ with a 180×150 mesh. We take $\alpha = \tan^{-1}(0.5)$. Zero-order extrapolation boundary conditions are used on the left and right boundaries. On the top and bottom boundaries all the conserved quantities are extrapolated in the direction parallel to the shock interface. In addition, to be consistent with zero-order extrapolation boundary condition on $\mathbf{B}$, the linear extrapolation of the magnetic potential A^z is used along the corresponding directions.

Shown in Figure 3.2 are the density contours of the solutions as computed using the base WENO scheme and the WENO-CT2D scheme. From this figure we note that the solution from the base scheme suffers from unphysical oscillations that are due to to divergence errors in the magnetic field, while the WENO-CT2D does not suffer from this problem. In

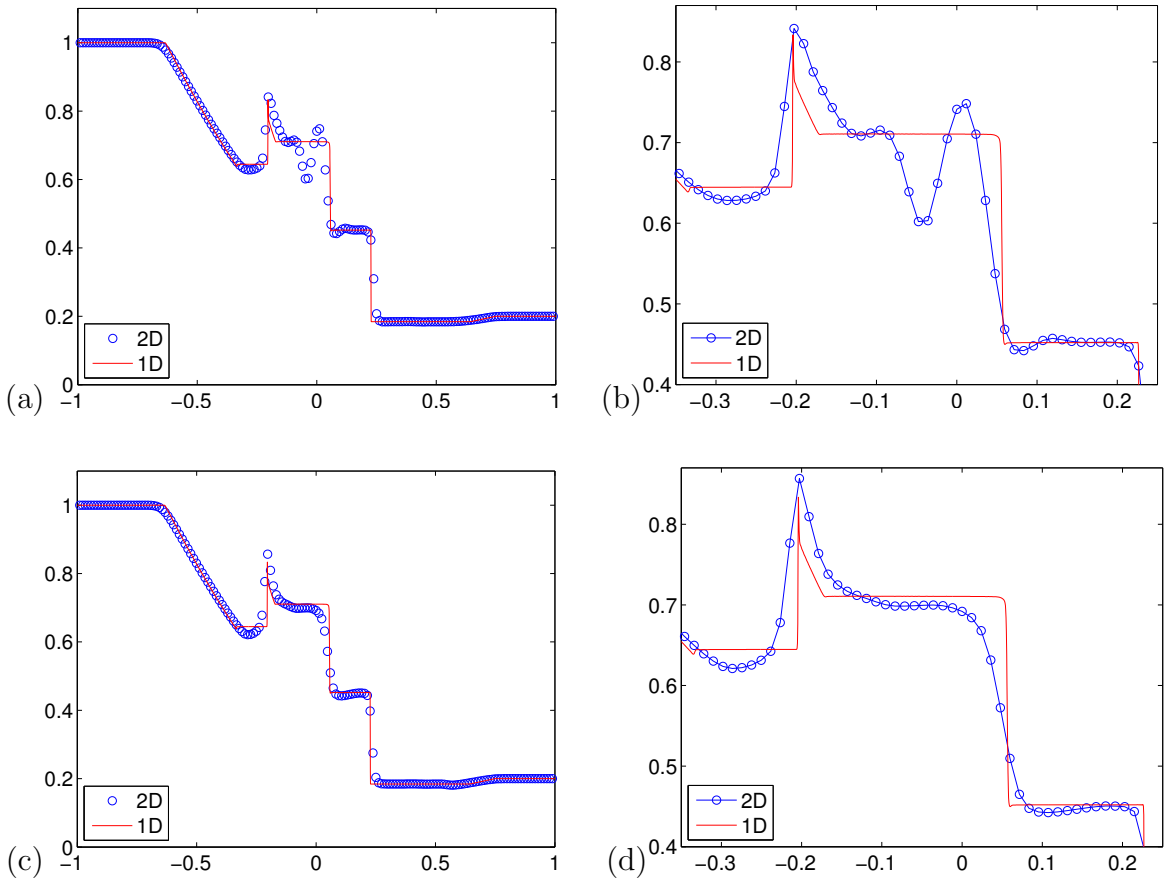

Figure 3.3: The rotated shock tube problem. Shown in these panels are (a) a 1D cut along $y = 0$ of ρ as computed with the base WENO scheme, (b) a zoomed in view of the same plot, (c) a 1D cut along $y = 0$ of ρ as computed with the WENO-CT2D scheme, and (d) a zoomed in view of the same plot. The solid line is a highly resolved 1D solution.

Figures 3.3 and 3.4 we also present a comparison of the 2D solutions along $y = 0$ compared against a 1D fifth-order WENO-HCL solution on a mesh with $N = 5000$. From these figures it is again clear that the base WENO scheme produces extra oscillations and larger errors, while the solution by the WENO-CT2D scheme are in good agreement with the 1D solution.

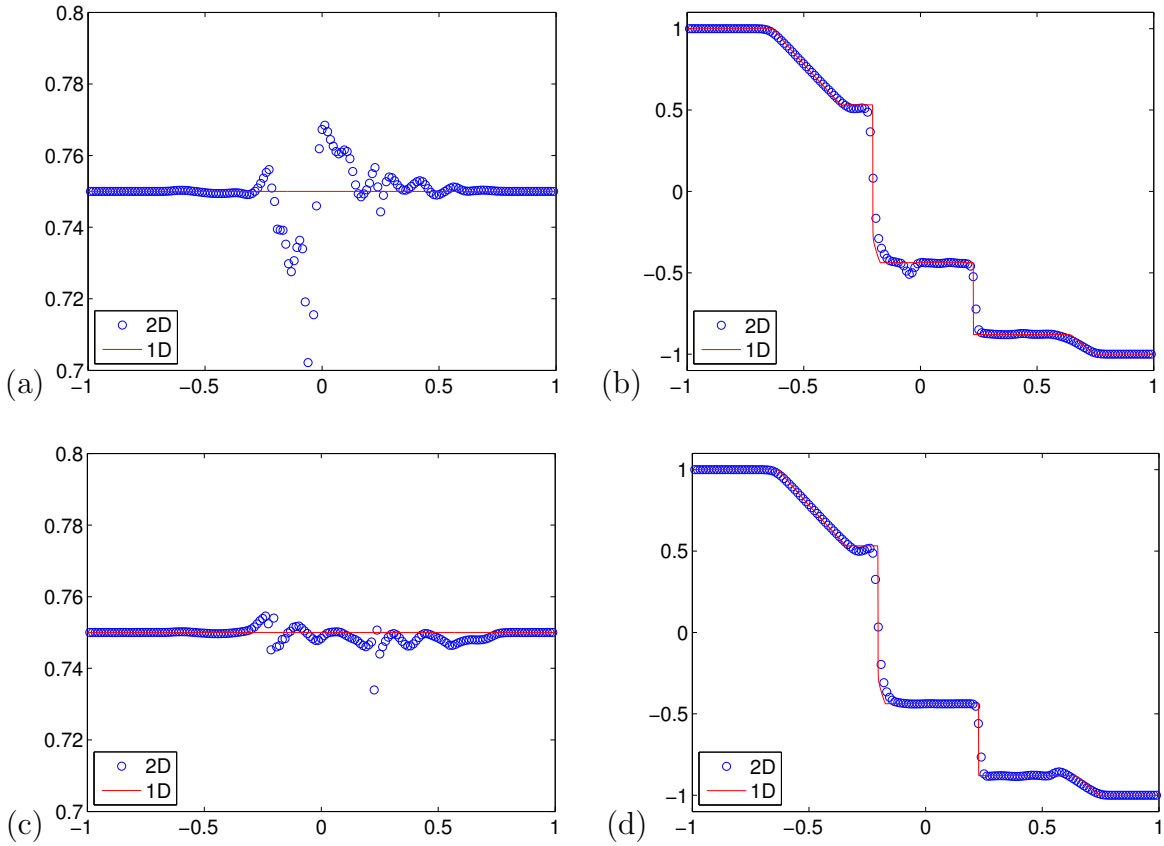

Figure 3.4: The rotated shock tube problem. Shown in these panels are 1D cuts along $y = 0$ of the magnetic field (a) perpendicular ($B^{\perp}$) and (b) parallel ($B^{\parallel}$) to the shock interface as computed with the base WENO scheme and 1D cuts along $y = 0$ of the magnetic field (c) perpendicular ($B^{\perp}$) and (d) parallel ($B^{\parallel}$) to the shock interface as computed with the WENO-CT2D dscheme. The solid line is a highly resolved 1D solution.

3.5.3 2D Orszag-Tang vortex

Next we consider the Orszag-Tang vortex problem, which is widely considered as a standard test example for MHD in the literature (e.g. [25, 60, 75, 83]), since the solution at late times in the simulation is quite sensitive to divergence errors. The problem has a smooth initial

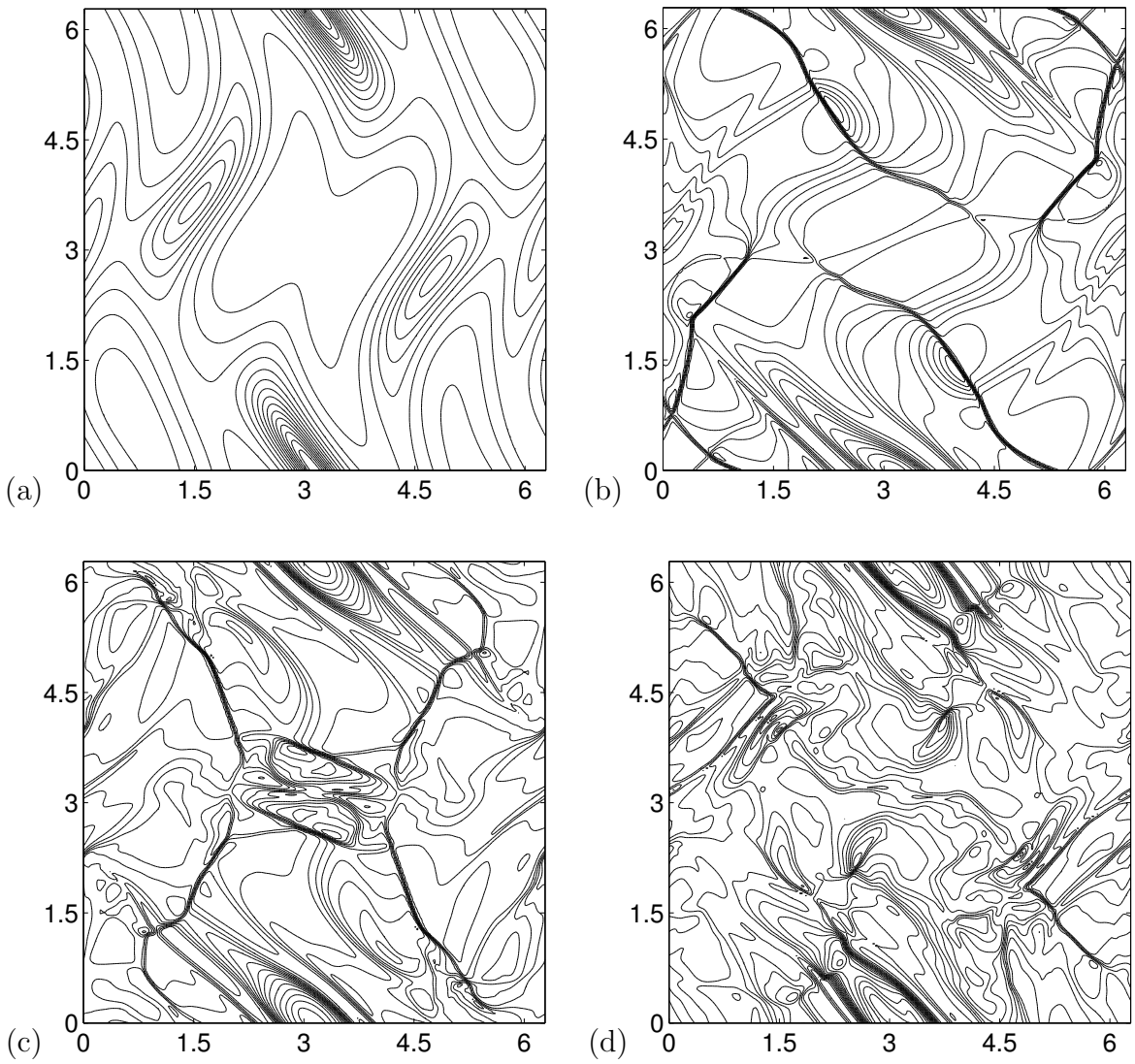

Figure 3.5: The Orszag-Tang vortex problem. Shown in these panels are ρ at times (a) $t = 0.5$, (b) $t = 2$, (c) $t = 3$, and (d) $t = 4$ as computed with the WENO-CT2D scheme on a 192×192 mesh. 15 equally spaced contours were used for each plot.

condition on the double-periodic box $[0, 2\pi] \times [0, 2\pi]$:

$$\rho(0, x, y) = \gamma^2, \quad u^x(0, x, y) = -\sin(y), \quad u^y(0, x, y) = \sin(x), \tag{3.56}$$

$$p(0, x, y) = \gamma, \quad B^x(0, x, y) = -\sin(y), \quad B^y(0, x, y) = \sin(2x), \tag{3.57}$$

$$u^z(0, x, y) = B^z(0, x, y) = 0, \tag{3.58}$$

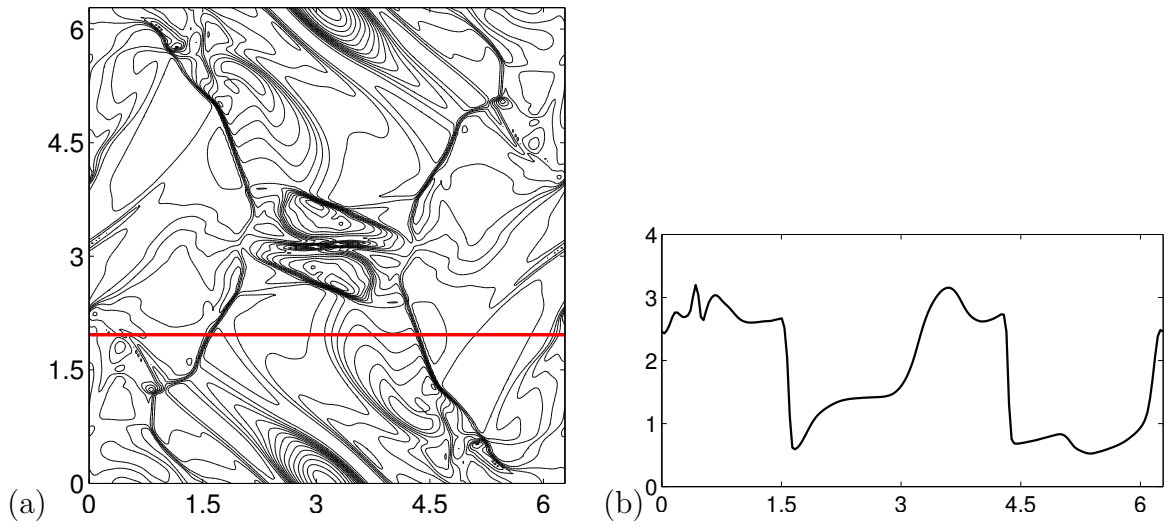

Figure 3.6: The Orszag-Tang vortex problem. Shown in these panels are (a) the thermal pressure as computed with the WENO-CT2D scheme at $t = 3$ on a 192×192 mesh and (b) a slice of the thermal pressure at $y = 0.625\pi$.

with the initial magnetic potential:

$$A^z(0, x, y) = 0.5\cos(2x) + \cos(y). \tag{3.59}$$

Periodic boundary conditions are imposed on all the boundaries. As time evolves, the solution forms several shock waves and a vortex structure in the middle of the computational domain.

We solve the MHD equations on a 192×192 mesh with the WENO-CT2D scheme. In Figure 3.5, we present the contours of density at $t = 0.5$, 2, 3, and 4. A slice of the pressure at $y = 0.625\pi$ and $t = 3$ is shown in the right panel of Figure 3.6. Although different papers display the solution at different times and resolutions, our results are in good agreement with those given in [25, 60, 75, 83]. We did not observe significant oscillations in any of the conserved quantities, even when the system is evolved out to long times. Our simulation was successfully run to $t = 30$ without the introduction of negative pressure anywhere in

the computational domain. On the other hand, the base scheme without CT step produces negative pressures at around $t = 4.0$ on a 192×192 mesh.

3.5.4 Cloud-shock interaction

Finally we consider the so-called cloud-shock interaction problem, which involves a strong shock interacting with a dense cloud that is in hydrostatic equilibrium. For this problem, we consider the 2D, 2.5D, and 3D versions of the proposed method. The 2D and 2.5D versions have the same physical setup. However, 2D means the problem is solved using the WENO-CT2D scheme, and 2.5D means that the magnetic field and the potential are solved using the WENO-CT3D scheme, i.e., with all the components of the magnetic field updated, although all the quantities are still independent of z.

3.5.4.1 2D problem

In this version we consider an MHD shock propagating toward a stationary bubble, with the same setup as the one in [60]. The computation domain is $(x, y) \in [0, 1] \times [0, 1]$ with inflow boundary condition at $x = 0$ and outflow boundary conditions on the three other sides. The initial conditions consist of a shock initialized at $x = 0.05$:

$$
\begin{aligned}
&(\rho, u^x, u^y, u^z, p, B^x, B^y, B^z)(0, x, y) \\
&= \begin{cases} (3.86859, 11.2536, 0, 0, 167.345, 0, 2.1826182, -2.1826182) & \text{if} \quad x < 0.05, \\ (1, 0, 0, 0, 1, 0, 0.56418958, 0.56418958) & \text{if} \quad x > 0.05, \end{cases}
\end{aligned} \tag{3.60}
$$

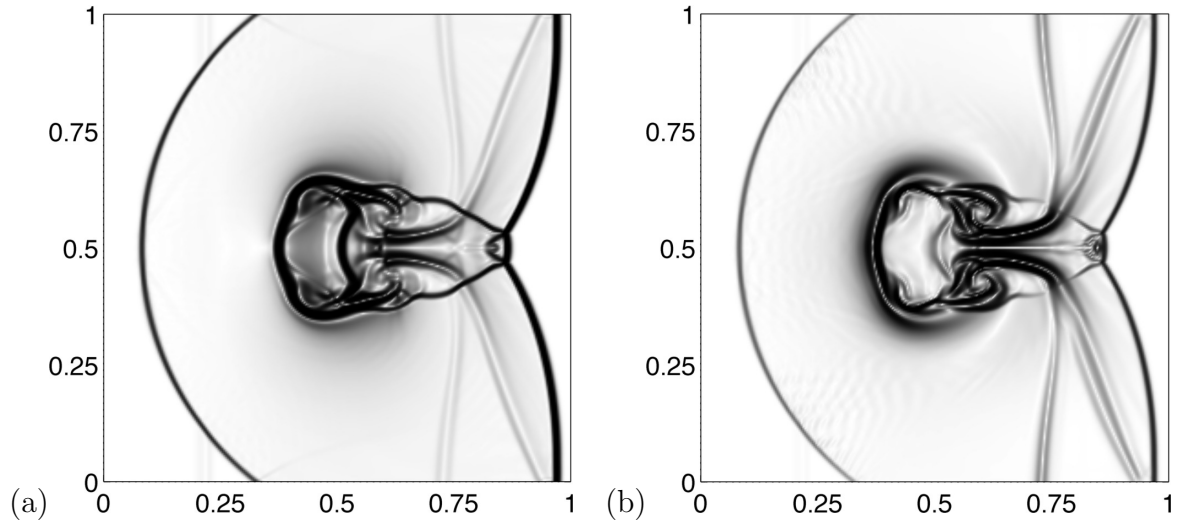

Figure 3.7: The 2D cloud-shock interaction problem. Shown in these panels are schlieren plots at time $t = 0.06$ of (a) $\ln(\rho)$ and (b) the norm of $\mathbf{B}$. The solution was obtained using the WENO-CT2D scheme on a 256×256 mesh.

and a circular cloud of density $\rho = 10$ and radius $r = 0.15$ centered at $(x, y) = (0.25, 0.5)$. The initial scalar magnetic potential is given by

$$A^z(0, x, y) = \begin{cases} -2.1826182(x - 0.05) & \text{if} \quad x \leq 0.05, \\ -0.56418958(x - 0.05) & \text{if} \quad x \geq 0.05. \end{cases} \tag{3.61}$$

The solution is computed on a 256×256 mesh. Shown in Figure 3.7 are schlieren plots of $\ln(\rho)$ and $\|\mathbf{B}\|$. In general, the solution shows good agreement with the one in [60], although the WENO-CT2D schemes shows some higher-resolution features. There is a noticeable extra structure that can be observed around $x = 0.75$ of the density plot (see Figure 3.7(a)). We also find that when the resolution of the solution using the second-order finite volume solver [60] is doubled to a mesh of 512×512, a similar structure starts to appear[2]. A similar structure can be observed in the solution of Dai and Woodward (Figure

[2]This test was done using freely available MHDCLAW [58] code.

18 in [25]) on a 512×512 mesh, although their problem setup is slightly different (i.e., they used a stationary shock instead of a stationary bubble). From another perspective, a similar structure around $x = 0.75$ can always be observed in the schlieren plots of $\|\mathbf{B}\|$ solved by different methods. Due to those facts, it is reasonable to believe that the solution should consist of this structure and that the high-order solver with less numerical dissipation can obtain this structure with fewer grid points than low-order methods.

3.5.4.2 2.5D problem

We also consider the 2D version problem with the magnetic field solved by WENO-CT3D scheme so as to compare our 3D and 2D schemes. We call this problem the 2.5D version to be consistent with [34, 35]. The problem is initialized in 2.5D with the same initial conditions as the 2D version (3.60). However, as discussed in Section 3.3, the magnetic potential evolutions of 2D and 3D are significantly different.

In 2.5D, since all quantities are independent of z, the magnetic vector potential satisfies the following evolution equation

$$\begin{aligned}
&\frac{\partial A^x}{\partial t} - u^y \frac{\partial A^y}{\partial x} - u^z \frac{\partial A^z}{\partial x} + u^z \frac{\partial A^x}{\partial y} = 0, \\
&\frac{\partial A^y}{\partial t} + u^x \frac{\partial A^y}{\partial x} - u^x \frac{\partial A^x}{\partial y} - u^z \frac{\partial A^z}{\partial y} = 0, \\
&\frac{\partial A^z}{\partial t} + u^x \frac{\partial A^z}{\partial x} + u^y \frac{\partial A^z}{\partial y} = 0.
\end{aligned} \tag{3.62}$$

The magnetic field satisfies

$$B^x = \frac{\partial A^z}{\partial y}, \quad B^y = -\frac{\partial A^z}{\partial x}, \quad \text{and} \quad B^z = \frac{\partial A^y}{\partial x} - \frac{\partial A^x}{\partial y}. \tag{3.63}$$

For this version of the cloud-shock problem, the magnetic vector potential is initialized as

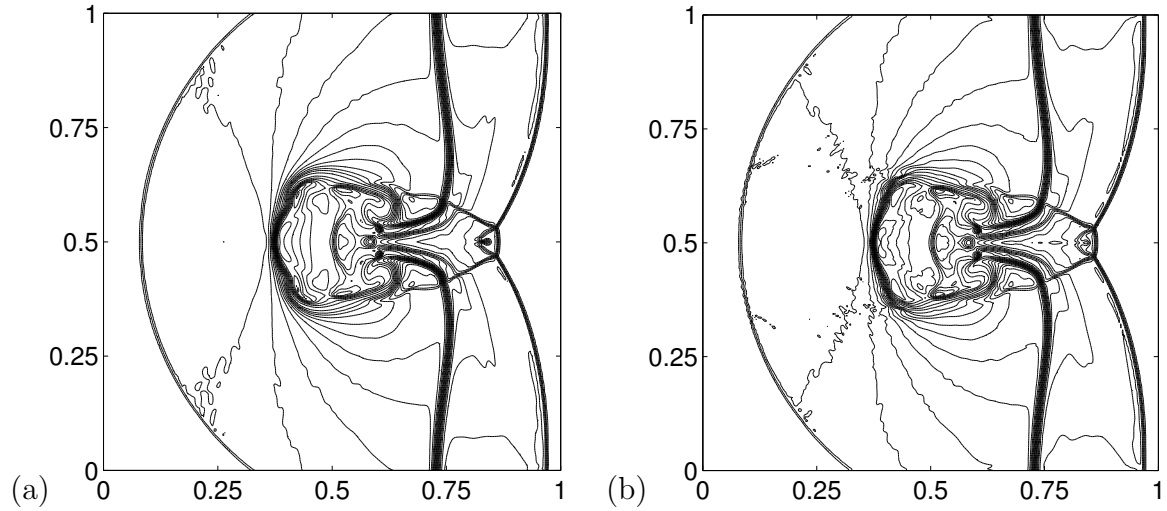

Figure 3.8: The 2D cloud-shock interaction problem. Shown in these panels are B^z at time $t = 0.06$ on a 256×256 mesh as solved with (a) the WENO-CT2D scheme and (b) the 2.5D version of the WENO-CT3D scheme. 25 equally spaced contours were used in each of these panels.

follows:

$$\mathbf{A}(0,x,y) = \begin{cases} (0, -2.1826182(x-0.05), -2.1826182(x-0.05)) & \text{if} \quad x \leq 0.05, \\ (0, 0.56418958(x-0.05), -0.56418958(x-0.05)) & \text{if} \quad x \geq 0.05. \end{cases} \tag{3.64}$$

The difference between the 2D and 2.5D schemes is essentially that B^z is not corrected in the CT step in the 2D scheme, while in the 2.5D we update B^z by partial derivatives of A^x and A^y as described above. It is also worthwhile to point out that $B^z_{,z}$ is identically zero in this case, so the update of B^z in (3.63) will not influence the divergence error. In the end, the two approaches produce very similar results. Shown in Figure 3.8 are contour plots of B^z using the two different approaches. For the WENO-CT3D scheme the diffusive limiter described in Section 3.3.3 was used with $\nu = 0.1$.

Although these methods compute B^z in the very different ways, the two solutions in Figure 3.8 are in good agreement. This result gives us confidence that the proposed 3D

scheme is able to solve the problem even with strong shocks. In addition, there are no significant oscillations observed in the 2.5D solution. These results also compare well with the results of the split finite volume CT approach of [34] and by the unsplit MOL finite volume CT approach of [35].

3.5.4.3 3D problem

The last problem we consider is a fully 3D version of the cloud-shock interaction problem. The initial conditions consist of a shock initialized at $x = 0.05$:

$$
\begin{aligned}
&(\rho, u^x, u^y, u^z, p, B^x, B^y, B^z)(0, x, y, z) = \\
&\begin{cases}
(3.86859, 11.2536, 0, 0, 167.345, 0, 2.1826182, -2.1826182) & \text{if} \quad x < 0.05, \\
(1, 0, 0, 0, 1, 0, 0.56418958, 0.56418958) & \text{if} \quad x > 0.05,
\end{cases}
\end{aligned}
\tag{3.65}
$$

and a spherical cloud of density $\rho = 10$ and radius $r = 0.15$ centered at $(x, y, z) = (0.25, 0.5, 0.5)$. The initial conditions for the magnetic potential are the same as (3.64). The solution is computed on the domain of $[0, 1]^3$. Inflow boundary conditions are imposed at $x = 0$ and outflow boundary conditions are used on all other sides. The solution is computed on a $128 \times 128 \times 128$ mesh using the WENO-CT3D scheme. In Figure 3.9 we show the density of the solution at $t = 0.06$, which is in good agreement with the solution in [34, 35], although our solution shows less oscillations and higher-resolution compared with previous work. We again observe an extra structure in the density plot, same as in our solution of the 2D problem. Here the diffusive limiter as described in Section 3.3.3 was used with $\nu = 0.1$.

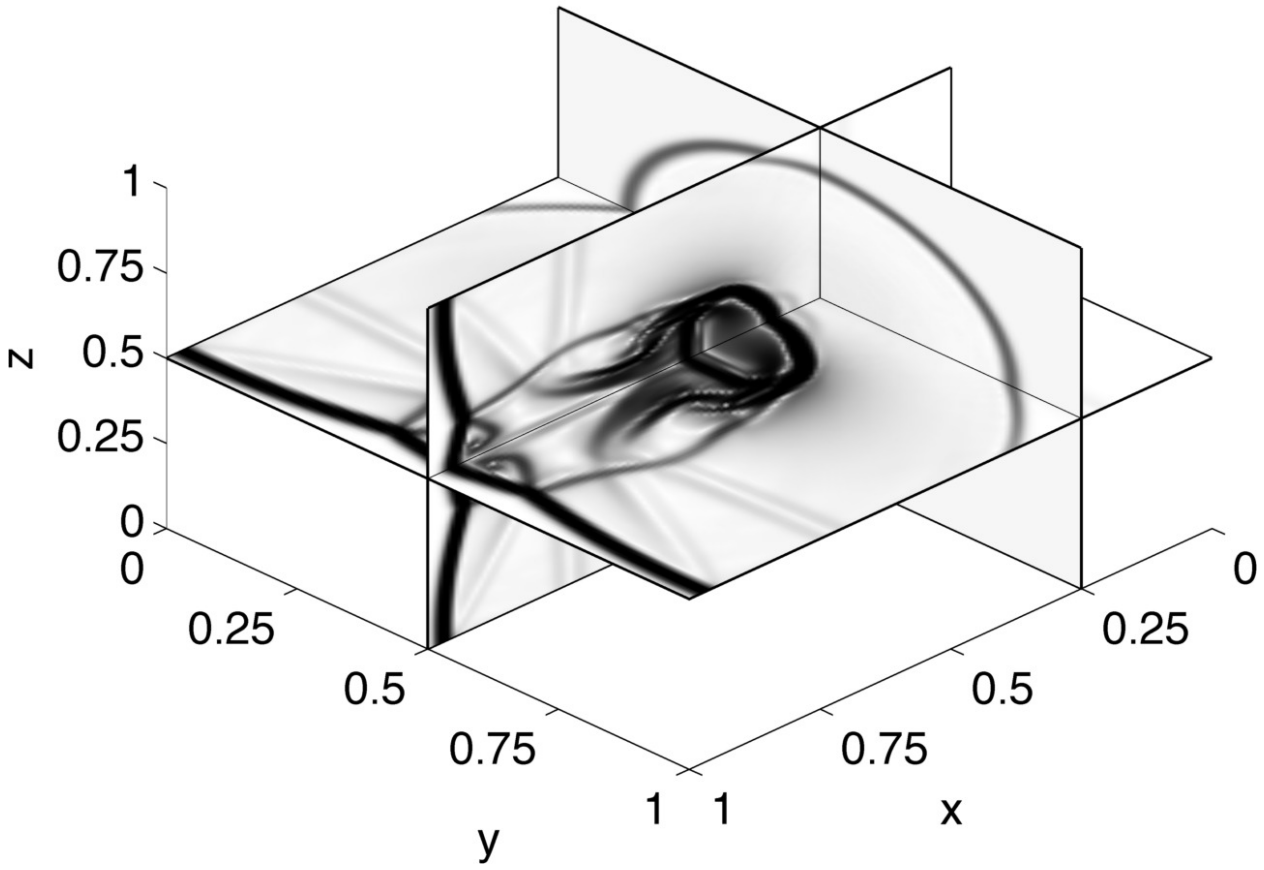

Figure 3.9: The 3D cloud-shock interaction problem. Shown in this plot is $\ln(\rho)$ as computed with the WENO-CT3D scheme on a $128 \times 128 \times 128$ mesh.

Chapter 4

Positivity-preserving limiter for ideal MHD

In this chapter, we utilize the maximum-principle-preserving flux limiting technique, originally designed for high order WENO-HCL methods for scalar hyperbolic conservation laws, to develop a positivity-preserving limiter for the FD-WENO methods for the ideal MHD equations. The resulting scheme, under the constrained transport framework, can achieve high order accuracy, a discrete divergence-free condition and positivity of the numerical solution simultaneously.

The outline of this chapter is as follows. In Section 4.1 and 4.2, we present positivity-preserving limiters for the 1D and multi-D MHD equations. In addition, we also detail the temporal discretization in this work in Section 4.2. The proposed schemes are implemented and tested on several 1D, 2D and 3D numerical examples in Section 4.4.

4.1 1D case

In this section, we describe our positivity-preserving limiter on a 1D MHD system. The divergence-free condition $\nabla \cdot \mathbf{B} = 0$ in 1D case is equivalent to $B^x = \text{constant}$. Since the

This chapter is to appear in [21]: A.J. Christlieb, Y. Liu, Q. Tang and Z. Xu. Positivity-preserving finite difference weighted ENO schemes with constrained transport for ideal magnetohydrodynamic equations. *SIAM J. Sci. Comput.,* to appear, 2015.

WENO hyperbolic conservation law solver (WENO-HCL) in [39, 40] without CT approaches will produce a solution with constant B^x, we use it as our MHD base scheme in 1D, to which we apply a positivity-preserving limiter.

The MHD equations in 1D (3.1) has been discussed in Section 3.1. Again, we let $q_i(t)$ be the numerical solution at the grid point x_i. The finite difference WENO-HCL schemes solve (3.1) by a conservative form:

$$\frac{dq_i(t)}{dt} + \frac{1}{\Delta x}\left(\hat{\mathbf{F}}_{i+\frac{1}{2}} - \hat{\mathbf{F}}_{i-\frac{1}{2}}\right) = 0, \tag{4.1}$$

where $\hat{\mathbf{F}}_{i+\frac{1}{2}}$ is defined as a high-order numerical flux constructed by WENO-HCL. The design of $\hat{\mathbf{F}}_{i+\frac{1}{2}}$ has been addressed in Section 3.1. One numerical difficulty is that the wave speeds of the MHD system involve the term $\frac{1}{\rho}$. To avoid the possibility of an infinite wave speed during the computation, we assume there is a small lower bound ϵ_0 for both density and pressure in the exact solution of the problem we considered.

The semi-discretized equation (4.1) can be further discretized in time by high-order time integrators. While our proposed scheme can be applied with any SSP-RK method, we take the third-order SSP-RK method (1.13) as an illustrative example. Here we let

$$L(q_i^n) = -\frac{1}{\Delta x}(\hat{\mathbf{F}}^n_{i+\frac{1}{2}} - \hat{\mathbf{F}}^n_{i-\frac{1}{2}}). \tag{4.2}$$

If we use $\hat{\mathbf{F}}^n_{i+\frac{1}{2}}$, $\hat{\mathbf{F}}^{(1)}_{i+\frac{1}{2}}$ and $\hat{\mathbf{F}}^{(2)}_{i+\frac{1}{2}}$ to denote the numerical fluxes reconstructed based on q^n, $q^{(1)}$ and $q^{(2)}$, the final stage of RK discretization (1.13) can be rewritten as

$$q_i^{n+1} = q_i^n - \lambda(\hat{\mathbf{F}}^{rk}_{i+\frac{1}{2}} - \hat{\mathbf{F}}^{rk}_{i-\frac{1}{2}}), \tag{4.3}$$

where

$$\lambda = \frac{\Delta t}{\Delta x}, \qquad \hat{\mathbf{F}}^{rk}_{i+\frac{1}{2}} = \frac{1}{6}\left(\hat{\mathbf{F}}^{n}_{i+\frac{1}{2}} + 4\hat{\mathbf{F}}^{(2)}_{i+\frac{1}{2}} + \hat{\mathbf{F}}^{(1)}_{i+\frac{1}{2}}\right). \tag{4.4}$$

$\hat{\mathbf{F}}^{rk}_{i+\frac{1}{2}}$ can be viewed as a linear combination of high-order numerical fluxes from different stages. Following the ideas in [78, 79], we need to modify the numerical flux $\hat{\mathbf{F}}^{rk}_{i+\frac{1}{2}}$ by a positivity-preserving flux to design a high-order positivity-preserving MHD scheme.

Cheng *et al.* [19] proved the simple Lax–Friedrichs numerical flux coupled with forward Euler time discretization is positivity-preserving for the 1D MHD equations (3.1) under the restriction CFL$\leq$ 0.5. When the Lax–Friedrichs scheme is used to solve the high-order solution q^n from t^n to t^{n+1}, we have

$$\hat{q}_i^{n+1} = q_i^n - \lambda(\hat{\mathbf{f}}_{i+\frac{1}{2}} - \hat{\mathbf{f}}_{i-\frac{1}{2}}), \tag{4.5}$$

where $\hat{q}_i^{n+1}$ is introduced to denote the low-order solution at x_i and $t = t^{n+1}$, and the Lax–Friedrichs flux is formulated as

$$\hat{\mathbf{f}}_{i+\frac{1}{2}} = \frac{1}{2}\left(\mathbf{f}(q^n_{j+1}) + \mathbf{f}(q^n_i) - \alpha(q^n_{j+1} - q^n_i)\right), \tag{4.6}$$

where the maximal wave speed α is defined by

$$\alpha = \max_i \left(|u^x| + c_f\right). \tag{4.7}$$

Here c_f is the fast speed of the MHD system, see Section 2.2.

The density and pressure computed by the first-order scheme (4.5) satisfy

$$\begin{cases} \hat{\rho}_i^{n+1} > 0, \\ \hat{p}_i^{n+1} > 0. \end{cases} \tag{4.8}$$

We can use the first-order solution $\hat{q}^{n+1}$ to define the numerical lower bounds for the density and pressure for the high-order solution q^{n+1}, which are

$$\epsilon_\rho^{n+1} = \min_i(\hat{\rho}_i^{n+1}, \epsilon_0), \tag{4.9}$$

$$\epsilon_p^{n+1} = \min_i(\hat{p}_i^{n+1}, \epsilon_0). \tag{4.10}$$

Throughout the simulations for this work, we take $\epsilon_0 = 10^{-13}$. It can be certainly taken as a smaller number if it is required by the problem and allowed by the machine precision.

Following [78, 79], to guarantee the positivity of the high-order solutions by the WENO scheme (4.3), we need to find a modification of the numerical flux as follows:

$$\tilde{\mathbf{F}}_{i+\frac{1}{2}} = \theta_{i+\frac{1}{2}}(\hat{\mathbf{F}}^{rk}_{i+\frac{1}{2}} - \hat{\mathbf{f}}_{i+\frac{1}{2}}) + \hat{\mathbf{f}}_{i+\frac{1}{2}}, \tag{4.11}$$

where the limiting parameter $\theta_{i+\frac{1}{2}} \in [0, 1]$. We seek a combination of $\theta_{i+\frac{1}{2}}$, such that the solutions satisfy

$$\begin{cases} \rho_i^{n+1} \geq \epsilon_\rho^{n+1}, \\ p_i^{n+1} \geq \epsilon_p^{n+1}. \end{cases} \tag{4.12}$$

Our positivity-preserving limiting technique follows a two-step procedure. First, as out-

lined below, we describe a strategy to guarantee the computed density positive. To facilitate the discussion, we denote the first-order flux of the density in $\hat{\mathbf{f}}$ as $\hat{f}^{\rho}$, whereas f^{ρ} and $\tilde{f}^{\rho}$ are the corresponding flux components in $\hat{\mathbf{F}}^{rk}$ and $\tilde{\mathbf{F}}$, respectively.

To preserve positive density, we need to find upper bounds $\Lambda^{\rho}_{\pm\frac{1}{2},I_i}$ of the limiting parameters $\theta_{i\pm\frac{1}{2}}$ at each cell I_i, such that, for any combination $(\theta_{i-\frac{1}{2}}, \theta_{i+\frac{1}{2}}) \in [0, \Lambda^{\rho}_{-\frac{1}{2},I_i}] \times [0, \Lambda^{\rho}_{+\frac{1}{2},I_i}]$, the following inequality holds:

$$\rho_i^{n+1}(\theta_{i-\frac{1}{2}}, \theta_{i+\frac{1}{2}}) = \rho_i^n - \lambda(\tilde{f}^{\rho}_{i+\frac{1}{2}} - \tilde{f}^{\rho}_{i-\frac{1}{2}}) \geq \epsilon_{\rho}^{n+1}, \tag{4.13}$$

where $\tilde{f}^{\rho}_{i+\frac{1}{2}} = \theta_{i+\frac{1}{2}}(f^{\rho}_{i+\frac{1}{2}} - \hat{f}^{\rho}_{i+\frac{1}{2}}) + \hat{f}^{\rho}_{i+\frac{1}{2}}$, Since we know $\hat{\rho}_i^{n+1} = \rho_i^n - \lambda(\hat{f}^{\rho}_{i+\frac{1}{2}} - \hat{f}^{\rho}_{i-\frac{1}{2}})$, (4.13) is equivalent to

$$\hat{\rho}_i^{n+1} - \lambda(\theta_{i+\frac{1}{2}}(f^{\rho}_{i+\frac{1}{2}} - \hat{f}^{\rho}_{i+\frac{1}{2}}) - \theta_{i-\frac{1}{2}}(f^{\rho}_{i-\frac{1}{2}} - \hat{f}^{\rho}_{i-\frac{1}{2}})) \geq \epsilon_{\rho}^{n+1}. \tag{4.14}$$

Due to the positivity-preserving property of the first-order scheme and the definition of ϵ_{ρ}^{n+1} (4.9), we have $\hat{\rho}_i^{n+1} \geq \epsilon_{\rho}^{n+1}$. Thus, the inequality (4.14) can be rewritten as,

$$\lambda\theta_{i-\frac{1}{2}}(f^{\rho}_{i-\frac{1}{2}} - \hat{f}^{\rho}_{i-\frac{1}{2}}) - \lambda\theta_{i+\frac{1}{2}}(f^{\rho}_{i+\frac{1}{2}} - \hat{f}^{\rho}_{i+\frac{1}{2}}) \geq \epsilon_{\rho}^{n+1} - \hat{\rho}_i^{n+1} \tag{4.15}$$

with the right-hand side $\epsilon_{\rho}^{n+1} - \hat{\rho}_i^{n+1} \leq 0$. For abbreviation, we introduce a notation $\Delta f_{i+\frac{1}{2}} = f^{\rho}_{i+\frac{1}{2}} - \hat{f}^{\rho}_{i+\frac{1}{2}}$.

Following the same idea in [78, 79], we will determine the upper bounds of the parameter $\theta_{i\pm\frac{1}{2}}$ by a case-by-case discussion based on the signs of $\Delta f_{i-\frac{1}{2}}$ and $\Delta f_{i+\frac{1}{2}}$. In particular, we decouple the inequalities (4.15) based on the following four cases:

- If $\Delta f_{i-\frac{1}{2}} \geq 0$ and $\Delta f_{i+\frac{1}{2}} \leq 0$, then

$$(\Lambda^{\rho}_{-\frac{1}{2},I_i}, \Lambda^{\rho}_{+\frac{1}{2},I_i}) = (1,1).$$

- If $\Delta f_{i-\frac{1}{2}} \geq 0$ and $\Delta f_{i+\frac{1}{2}} > 0$, then

$$(\Lambda^{\rho}_{-\frac{1}{2},I_i}, \Lambda^{\rho}_{+\frac{1}{2},I_i}) = \left(1, \min\left(1, \frac{\epsilon_{\rho}^{n+1} - \hat{\rho}_i^{n+1}}{-\lambda \Delta f_{i+\frac{1}{2}}}\right)\right).$$

- If $\Delta f_{i-\frac{1}{2}} < 0$ and $\Delta f_{i+\frac{1}{2}} \leq 0$, then

$$(\Lambda^{\rho}_{-\frac{1}{2},I_i}, \Lambda^{\rho}_{+\frac{1}{2},I_i}) = \left(\min\left(1, \frac{\epsilon_{\rho}^{n+1} - \hat{\rho}_i^{n+1}}{\lambda \Delta f_{i-\frac{1}{2}}}\right), 1\right).$$

- If $\Delta f_{i-\frac{1}{2}} < 0$ and $\Delta f_{i+\frac{1}{2}} > 0$,

  - if the inequality (4.15) is satisfied with $(\theta_{i-\frac{1}{2}}, \theta_{i+\frac{1}{2}}) = (1,1)$ then

$$(\Lambda^{\rho}_{-\frac{1}{2},I_i}, \Lambda^{\rho}_{+\frac{1}{2},I_i}) = (1,1).$$

  - otherwise, we choose

$$(\Lambda^{\rho}_{-\frac{1}{2},I_i}, \Lambda^{\rho}_{+\frac{1}{2},I_i}) = \left(\frac{\epsilon_{\rho}^{n+1} - \hat{\rho}_i^{n+1}}{\lambda \Delta f_{i-\frac{1}{2}} - \lambda \Delta f_{i+\frac{1}{2}}}, \frac{\epsilon_{\rho}^{n+1} - \hat{\rho}_i^{n+1}}{\lambda \Delta f_{i-\frac{1}{2}} - \lambda \Delta f_{i+\frac{1}{2}}}\right).$$

This procedure has been discussed in [78, 79]. It is easy to show when $(\theta_{i-\frac{1}{2}}, \theta_{i+\frac{1}{2}}) \in [0, \Lambda^{\rho}_{-\frac{1}{2},I_i}] \times [0, \Lambda^{\rho}_{+\frac{1}{2},I_i}]$ with the bounds $\Lambda^{\rho}_{\pm\frac{1}{2},I_i}$ obtained by the above strategy that, the inequality (4.15) holds, i.e., the density ρ_i^{n+1} is positive at each grid x_i. We define this set

as S_{ρ,I_i}:

$$S_{\rho,I_i} = [0, \Lambda^{\rho}_{-\frac{1}{2},I_i}] \times [0, \Lambda^{\rho}_{+\frac{1}{2},I_i}]. \tag{4.16}$$

We next describe a strategy to obtain positive pressure. First we discuss some properties of the pressure function

$$p(q) = (\gamma - 1)\left(\mathcal{E} - \frac{1}{2}\frac{(\rho u^x)^2 + (\rho u^y)^2 + (\rho u^z)^2}{\rho} - \frac{1}{2}\left((B^x)^2 + (B^y)^2 + (B^z)^2\right)\right). \tag{4.17}$$

We note the pressure function is concave with respect to $q = (\rho, \rho u^x, \rho u^y, \rho u^z, \mathcal{E}, B^x, B^y, B^z)^T$.

Similar as the function $\rho_i^{n+1}(\theta_{i-\frac{1}{2}}, \theta_{i+\frac{1}{2}})$, we can define a function $p_i^{n+1}(\theta_{i-\frac{1}{2}}, \theta_{i+\frac{1}{2}})$ as follows:

$$p_i^{n+1}(\theta_{i-\frac{1}{2}}, \theta_{i+\frac{1}{2}}) := p(q_i^{n+1}(\theta_{i-\frac{1}{2}}, \theta_{i+\frac{1}{2}})). \tag{4.18}$$

We need the following lemma to construct the limiter.

Lemma 4.1.1. *The pressure function satisfies*

$$p\left(q_i^{n+1}\left(\alpha\overrightarrow{\theta}^1 + (1-\alpha)\overrightarrow{\theta}^2\right)\right) \geq \alpha p\left(q_i^{n+1}\left(\overrightarrow{\theta}^1\right)\right) + (1-\alpha)p\left(q_i^{n+1}\left(\overrightarrow{\theta}^2\right)\right) \tag{4.19}$$

for any $\alpha \in [0,1]$ *and* $\overrightarrow{\theta}^1, \overrightarrow{\theta}^2 \in S_{\rho,I_i}$.

The proof of this lemma is straightforward, as long as we use the concave property of $p(q)$ and note that the solution q_i^{n+1} is a linear function of its limiting parameters, i.e.,

$$q_i^{n+1}\left(\alpha\overrightarrow{\theta}^1 + (1-\alpha)\overrightarrow{\theta}^2\right) = \alpha q_i^{n+1}\left(\overrightarrow{\theta}^1\right) + (1-\alpha)q_i^{n+1}\left(\overrightarrow{\theta}^2\right).$$

A similar lemma for the Euler equations has been use in the past [20, 78].

We want to identify a subset of the set S_{ρ,I_i}, denoted by S_{p,I_i}, such that $p_i^{n+1}(\theta_{i-\frac{1}{2}}, \theta_{i+\frac{1}{2}})$ is positive, i.e.,

$$S_{p,I_i} = \{(\theta_{i-\frac{1}{2}}, \theta_{i+\frac{1}{2}}) \in [0, \Lambda^{\rho}_{-\frac{1}{2},I_i}] \times [0, \Lambda^{\rho}_{+\frac{1}{2},I_i}] : p_i^{n+1}(\theta_{i-\frac{1}{2}}, \theta_{i+\frac{1}{2}}) \geq \epsilon_p^{n+1}\}. \tag{4.20}$$

Due to Lemma 4.1.1, S_{p,I_i} is a convex set. To determine S_{p,I_i}, we can only focus on its vertices.

If we denote the four vertices of S_{ρ,I_i} to be $P^{k_1,k_2} = (k_1\Lambda^{\rho}_{-\frac{1}{2},j}, k_2\Lambda^{\rho}_{+\frac{1}{2},j})$, with k_1, k_2 being 0 or 1, similarly we can define the vertices of S_{p,I_i} to be $\hat{P}^{k_1,k_2}$.

We determine the $\hat{P}^{k_1,k_2}$ based on the following strategy. For $(k_1, k_2) \neq (0, 0)$, if $p_i^{n+1}(P^{k_1,k_2}) \geq \epsilon_p^{n+1}$, we let $\hat{P}^{k_1,k_2} = P^{k_1,k_2}$; otherwise we find a scalar parameter of r such that $p_i^{n+1}(rP^{k_1,k_2}) \geq \epsilon_p^{n+1}$ and let $\hat{P}^{k_1,k_2} = rP^{k_1,k_2}$. The resulting three vertices $\hat{P}^{k_1,k_2}$ with the origin $(0, 0)$ form S_{p,I_i}.

Next, we can identify a rectangle inside S_{p,I_i} denoted by

$$R_{\rho,p,I_i} = [0, \Lambda_{-\frac{1}{2},I_i}] \times [0, \Lambda_{+\frac{1}{2},I_i}], \tag{4.21}$$

where

$$\Lambda_{-\frac{1}{2},I_i} = \min_{k_2=0,1}(\hat{P}^{1,k_2}), \quad \Lambda_{+\frac{1}{2},I_i} = \min_{k_1=0,1}(\hat{P}^{k_1,1}). \tag{4.22}$$

After repeating this procedure for all j, we let

$$\theta_{i+\frac{1}{2}} = \min(\Lambda_{+\frac{1}{2},I_i}, \Lambda_{-\frac{1}{2},I_{i+1}}), \tag{4.23}$$

and this finishes our discussion for the 1D limiter.

Remark 4.1.2. *The limiting technique here is used only to guarantee the positivity of the solution at the final stage of RK methods. If there is negative density or pressure in the intermediate stage, in this work we take the absolute value of the density and pressure in the code where a positive solution is required. The first place that needs a positive solution is to estimate the speed waves of the system. For instance, the speed of sound is taken as* $c = \sqrt{\gamma|p|/|\rho|}$ *in the intermediate stage. The second place requiring a positive solution is to estimate the eigenvectors of the Jacobian matrix of the flux function. Those treatments will not degrade the order of accuracy, because the WENO algorithm only needs an estimate of the local eigenvalues and eigenvectors and we always use the true solution to compute the numerical flux even when it becomes negative in the intermediate stage. On the other hand, we also remark that the limiter can be applied to each stage when the positivity in the intermediate stage is required.*

Remark 4.1.3. *From the limiting steps, we can see the overall scheme has a CFL constraint of 0.5, which is same as the Lax–Friedrichs scheme. When the above limiting technique is applied to the intermediate stages, there is no extra restriction because the time step of the intermediate stage is typically no greater than* Δt.

Remark 4.1.4. *One numerical difficulty is to satisfy* $p(rP^{k_1,k_2}) \geq \epsilon_p^{n+1}$. *This can be done by solving a root* r *for the equation* $p(rP^{k_1,k_2}) = \epsilon_p^{n+1}$. *Through a simple derivation, it can*

be easily shown that the solution $q_i^{n+1}(rP^{k_1,k_2})$ *satisfies*

$$q_i^{n+1}(rP^{k_1,k_2}) = rq_i^{n+1}(P^{k_1,k_2}) + (1-r)\hat{q}_i^{n+1},$$

where $\hat{q}_i^{n+1}$ *is again used to denote the solution solved by the first-order flux* $\hat{\mathbf{f}}_{i+\frac{1}{2}}$. *This property is independent from the dimension, which makes it naturally extendable for the multi-D cases. More importantly,* $q_i^{n+1}(P^{k_1,k_2})$ *and* $\hat{q}_i^{n+1}$ *are both computationally cheap to evaluate. So with* $q_i^{n+1}(P^{k_1,k_2})$ *and* $\hat{q}_i^{n+1}$ *known, we can solve a root* r *for the equation*

$$p(rq_i^{n+1}(P^{k_1,k_2}) + (1-r)\hat{q}_i^{n+1}) = \epsilon_p^{n+1}.$$

In the MHD equation case, this equation is a cubic function of r *in general. We note that there exists at least one root in the interval* $[0,1]$, *which can always be found by Newton iteration. However, in the implementation, we only used a simple bisection method with a maximum of 10 iterations to find the root, because our purpose is to obtain a positive pressure* $p(rq_i^{n+1}(P^{k_1,k_2}))$ *instead of finding an accurate* r. *During the numerical simulations, we found the effect of the number of iterations on the solution quality and accuracy is negligible. A similar approach to find a limiting parameter can be found in the design of the positivity-preserving MHD scheme [5].*

4.2 Multi-D case

In this section, we briefly describe the positivity-preserving limiter in the multi-D case. To control the divergence error, our base scheme is taken as the WENO-CT scheme outlined in Chapter 3. In the discussion below, we only focus on the 2D case, keeping in mind that the

extension to 3D case is quite straightforward.

The 2D MHD system (2.1) can be rewritten as:

$$\frac{\partial q}{\partial t} + \frac{\partial \mathbf{f}(q)}{\partial x} + \frac{\partial \mathbf{g}(q)}{\partial y} = 0. \tag{4.24}$$

We need to solve (4.24) to get the update for the conserved quantities. If a general RK method is used as the time integrator, the WENO-HCL scheme solves (4.24) by a conservative form:

$$q_{ij}^{n+1} = q_{ij}^{n} - \lambda_x(\hat{\mathbf{F}}^{rk}_{i+\frac{1}{2}j} - \hat{\mathbf{F}}^{rk}_{i-\frac{1}{2}j}) - \lambda_y(\hat{\mathbf{G}}^{rk}_{ij+\frac{1}{2}} - \hat{\mathbf{G}}^{rk}_{ij-\frac{1}{2}}), \tag{4.25}$$

where $\hat{\mathbf{F}}^{rk}$ and $\hat{\mathbf{G}}^{rk}$ are linear combinations of high-order numerical fluxes from three RK stages and $\lambda_\alpha = \frac{\Delta t}{\Delta \alpha}$. Let $\hat{\mathbf{f}}_{i+\frac{1}{2}j}$ and $\hat{\mathbf{g}}_{ij+\frac{1}{2}}$ again be the first-order Lax–Friedrichs fluxes. Then we modify the high-order numerical fluxes $\hat{\mathbf{F}}^{rk}$ and $\hat{\mathbf{G}}^{rk}$ by the Lax–Friedrichs fluxes $\hat{\mathbf{f}}_{i+\frac{1}{2}j}$ and $\hat{\mathbf{g}}_{ij+\frac{1}{2}}$ to achieve the positivity of the solution, i.e.,

$$\tilde{\mathbf{F}}_{i+\frac{1}{2}j} = \theta_{i+\frac{1}{2}j}(\hat{\mathbf{F}}^{rk}_{i+\frac{1}{2}j} - \hat{\mathbf{f}}_{i+\frac{1}{2}j}) + \hat{\mathbf{f}}_{i+\frac{1}{2}j}, \tag{4.26}$$

$$\tilde{\mathbf{G}}_{ij+\frac{1}{2}} = \theta_{ij+\frac{1}{2}}(\hat{\mathbf{G}}^{rk}_{ij+\frac{1}{2}} - \hat{\mathbf{g}}_{ij+\frac{1}{2}}) + \hat{\mathbf{g}}_{ij+\frac{1}{2}}. \tag{4.27}$$

For each grid x_{ij}, we use a two-step strategy similar to the 1D case. Firstly, we follow a similar strategy to guarantee the computed density positive, i.e., to find four upper bounds $\Lambda^{\rho}_{L,I_{ij}}$, $\Lambda^{\rho}_{R,I_{ij}}$, $\Lambda^{\rho}_{U,I_{ij}}$ and $\Lambda^{\rho}_{D,I_{ij}}$ such that for any $(\theta_{i-\frac{1}{2}j}, \theta_{i+\frac{1}{2}j}, \theta_{ij-\frac{1}{2}}, \theta_{ij+\frac{1}{2}}) \in S_{\rho,I_{ij}}$,

where

$$S_{\rho,I_{ij}} = [0, \Lambda^{\rho}_{L,I_{ij}}] \times [0, \Lambda^{\rho}_{R,I_{ij}}] \times [0, \Lambda^{\rho}_{D,I_{ij}}] \times [0, \Lambda^{\rho}_{U,I_{ij}}], \tag{4.28}$$

the computed density satisfies,

$$\rho^{n+1}_{ij}(\theta_{i-\frac{1}{2}j}, \theta_{i+\frac{1}{2}j}, \theta_{ij-\frac{1}{2}}, \theta_{ij+\frac{1}{2}}) \geq \epsilon^{n+1}_{\rho}. \tag{4.29}$$

Secondly, we can find a rectangular set $R_{\rho,p,I_{ij}} = [0, \Lambda_{L,I_{ij}}] \times [0, \Lambda_{R,I_{ij}}] \times [0, \Lambda_{D,I_{ij}}] \times [0, \Lambda_{U,I_{ij}}]$, which is a subset of $S_{\rho,I_{ij}}$, such that for any $(\theta_{i-\frac{1}{2}j}, \theta_{i+\frac{1}{2}j}, \theta_{ij-\frac{1}{2}}, \theta_{ij+\frac{1}{2}}) \in R_{\rho,p,I_{ij}}$, we have,

$$p^{n+1}_{ij}(\theta_{i-\frac{1}{2}j}, \theta_{i+\frac{1}{2}j}, \theta_{ij-\frac{1}{2}}, \theta_{ij+\frac{1}{2}}) \geq \epsilon^{n+1}_{p}. \tag{4.30}$$

Here ϵ^{n+1}_{ρ} and ϵ^{n+1}_{p} are the 2D lower bounds with similar definitions as the 1D case (4.9) and (4.10). The strategy to find the set $R_{\rho,p,I_{ij}}$ is similar to the Euler equations case [78]. We omit the details here. An important different from the 1D case in Section 4.1 is, the step 4.22 in 1D case becomes

$$\Lambda_{L,I_{ij}} = \min_{k_{2,3,4}=0,1}(\hat{P}^{1,k_2,k_3,k_4}), \quad \Lambda_{R,I_{ij}} = \min_{k_{1,3,4}=0,1}(\hat{P}^{k_1,1,k_3,k_4}), \tag{4.31}$$

$$\Lambda_{D,I_{ij}} = \min_{k_{1,2,4}=0,1}(\hat{P}^{k_1,k_2,1,k_4}), \quad \Lambda_{U,I_{ij}} = \min_{k_{1,2,3}=0,1}(\hat{P}^{k_1,k_2,k_3,1}). \tag{4.32}$$

After repeating this procedure for all nodes (i, j), we let

$$\theta_{i+\frac{1}{2}j} = \min(\Lambda_{R,I_{ij}}, \Lambda_{L,I_{i+1j}}), \tag{4.33}$$

$$\theta_{ij+\frac{1}{2}} = \min(\Lambda_{U,I_{ij}}, \Lambda_{D,I_{ij+1}}). \tag{4.34}$$

This whole procedure will produce a numerical solution with positive density and pressure after Step 1 in CT framework. Followed by Step 2 and 3 with **Option 2**, we achieve high order accuracy, a discrete divergence-free condition and positivity of the numerical solution simultaneously. The overall scheme shares the same CFL constraint as the low-order Lax-Fridrichs scheme. There are no extra CFL restrictions from the limiting process.

As pointed out in [19], there is still no rigorous proof that the Lax–Friedrichs scheme or any other first-order scheme is positivity-preserving in the mutli-D case when the divergence-free constraint is considered. In this work, we still use the first-order Lax–Friedrichs scheme as the low-order correction scheme for the multi-D cases. Like [19], we take CFL ≤ 0.5 as the constraint for the positivity-preserving Lax–Friedrichs scheme in the multi-D cases. On the other hand, our limiting technique is independent from the choice of the low-order scheme. The overall scheme will be improved as long as a provable positivity-preserving scheme is found and used as the building block.

4.3 Temporal discretization

In this section we describe some details of time-stepping techniques used in this work. In Chapter 3, we use SSP-RK4 as our time integrator and also correct the magnetic field each time step. Here we make some adjustments so that the limiting schemes become more

efficient.

First, we make exclusive use of **Option 2** in this work, so as to preserve the positivity of the pressure after the magnetic field is corrected. This is a common technique in the CT framework for problems involving low-β plasma [10, 75]. Under this option, if the density and pressure after Step 1 are positive, they will remain positive in the overall computation. Therefore, with the proposed limiter, the numerical solutions maintain positive throughout the whole CT steps.

Second, since the limiter is only applied to the final stage of the RK methods in this work, the RK methods with larger CFL number (such as SSP-RK4 method used in Chapter 3) is not very stable by this treatment. So instead, we use traditional SSP-RK3 method as the tested integrator with a CFL number of 0.5 being used.

Another difference of the schemes lies in the implementation of the correction steps (Steps 2 and 3). We propose to perform the correction steps only at the end of each time step t^n instead of each stage of RK methods in Chapter 3. Thanks to this modification, we can simply focus on the final stage of the solution when implementing the limiting technique in Section 4.1. Numerical results show negligible differences between the two approaches when SSP-RK3 time-stepping is used. However, we note that this modification may result in accumulation of the divergence error especially for RK methods with large stage numbers. For those time stepping schemes, this kind of modification is not recommended and the correction steps have to be performed at each stage. Thus, if SSP-RK4 method is used for those low density and pressure problem, both the proposed limiter and the correction steps (Steps 2 and 3) have to be applied at each time step.

4.4 Numerical examples

In this section, we perform numerical simulations with the resulting positivity-preserving schemes in 1D, 2D and 3D. SSP-RK3 scheme serves as the time integrator in all the examples, whereas the fifth-order finite difference WENO-HCL scheme is used for solving the base MHD equations in different examples. In multi-D, our fourth-order CT method is used to obtain a divergence-free magnetic field. Unless otherwise stated, the gas constant is $\gamma = 5/3$ and the CFL number is 0.5.

4.4.1 Test cases in 1D

In this subsection, we test our positivity-preserving scheme with several 1D MHD examples. We note that for all the cases presented in this subsection, negative pressure or density is observed if the base MHD scheme is applied without a positivity-preserving limiter. Here, the base MHD scheme is a fifth-order WENO-HCL scheme.

4.4.1.1 Vacuum shock tube test

We first consider a 1D vacuum shock tube problem. This example is used to demonstrate that our positivity-preserving MHD solver can handle very low density and pressure. The initial condition is

$$(\rho, u^x, u^y, u^z, p, B^x, B^y, B^z) = \begin{cases} (10^{-12}, 0, 0, 0, 10^{-12}, 0, 0, 0) & \text{if} \quad x < 0, \\ (1, 0, 0, 0, 0.5, 0, 1, 0) & \text{if} \quad x > 0. \end{cases} \tag{4.35}$$

It is similar to the vacuum shock tube problem in [76]. The computational domain is $[-0.5, 0.5]$ and zero-order extrapolation boundary conditions are used. Shown in Figure

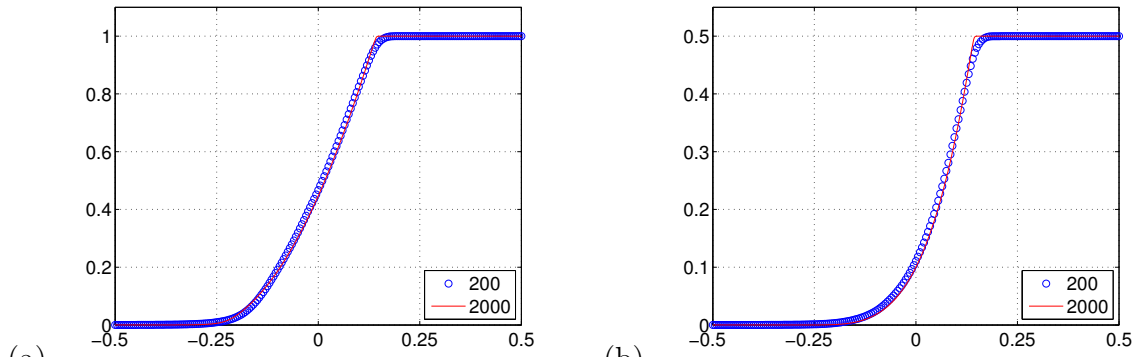

Figure 4.1: The vacuum shock tube problem. Shown in these panels are plots at time $t = 0.1$ of (a) ρ and (b) the thermal pressure. The blue circle is a solution solved on a mesh with $N = 200$. The solid line is a highly resolved solution.

4.1 are the density and pressure of the solution on a mesh with $N = 200$ and the highly resolved solution with $N = 2000$. We can observe the solutions of low resolution and high resolution are in good agreement.

4.4.1.2 Torsional Alfvén wave pulse

We also consider the torsional Alfvén wave pulse problem [9, 19]. The initial condition is

$$(\rho, u^x, u^y, u^z, p, B^x, B^y, B^z) = (1, 10, 10\cos\phi, 10\sin\phi, 0.01, -10\cos\phi, -10\sin\phi, 0), \quad (4.36)$$

where $\phi = \frac{\pi}{8}(\tanh(\frac{0.25+x}{\delta} + 1))(\tanh(\frac{0.25-x}{\delta} + 1))$ and $\delta = 0.005$. The computational domain is $[-0.5, 0.5]$ and periodic boundary conditions are used. In this test problem, the initial pressure is so small that the problem is very sensitive to the dissipation introduced by numerical schemes. Further, the existence of a strong torsional Alfvén wave discontinuity makes the problem difficult to simulate. In the simulation without the limiter, the base WENO-HCL introduced a negative pressure in a few time steps and the solutions become unphysical immediately. With the limiter, our scheme can simulate the problem stably and

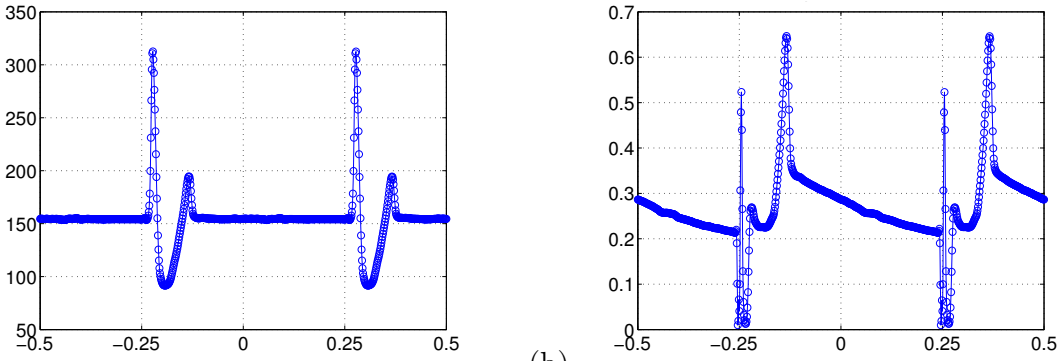

(a) (b)

Figure 4.2: The torsional Alfvén wave pulse. Shown in these panels are plots at time $t = 0.156$ of (a) the energy and (b) the thermal pressure. The solution was obtained on a mesh with $N = 800$.

the numerical results at $t = 0.156$ are shown in Figures 4.2 and 4.3 with $N = 800$. Shown in the figures are plots of the energy, the thermal pressure, u^y, u^z, B^y, and B^z. It is observed that our method successfully captures the two discontinuities and the results are comparable with those in [9, 49]. However, small bumps can still be observed around one of the discontinuities of both u^y and u^z. As pointed out in [9], this is because the MHD solver introduced too much numerical dissipation to keep the pressure positive. The primary reason is the Riemann solver around the discontinuities is not selective enough.

4.4.2 Test cases in multi-D

In this subsection, we consider several 2D and 3D examples to demonstrate the accuracy and efficiency of our positivity-preserving multi-D MHD solver in the CT framework. In the following tests, we implement fourth-order WENO-CT2D and WENO-CT3D schemes as the MHD solver, to which we apply our positivity-preserving limiter. Unless otherwise stated, we use **Option 2** for the multi-D simulation.

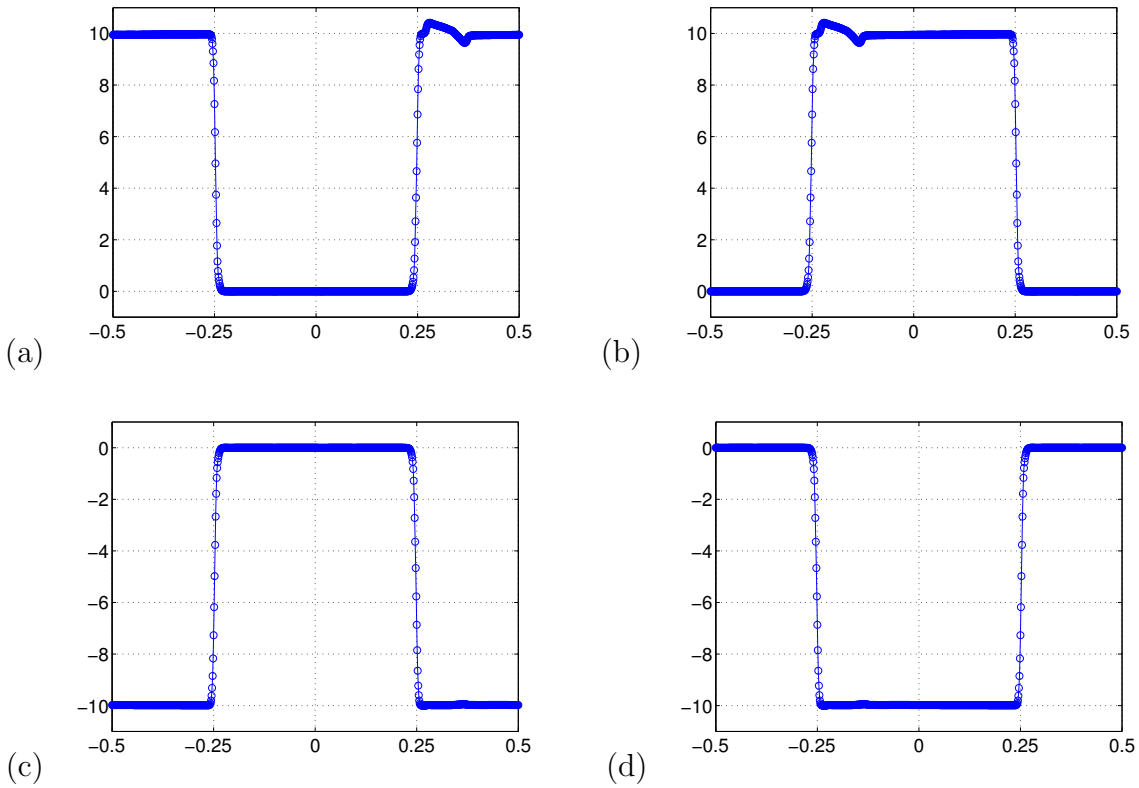

Figure 4.3: The torsional Alfvén wave pulse. Shown in these panels are plots at time $t = 0.156$ of (a) u^y, (b) u^z, (c) B^y and (d) B^z. The solution was obtained on a mesh with $N = 800$.

4.4.2.1 Smooth vortex test in MHD

We consider the smooth vortex problem with non-zero magnetic field to demonstrate the scheme can maintain the designed accuracy within the CT framework. We consider a modification of the smooth vortex problem considered in [3, 48, 80]. The initial condition is a mean flow

$$(\rho, u^x, u^y, u^z, p, B^x, B^y, B^z) = (1, 1, 1, 0, 1, 0, 0, 0), \tag{4.37}$$

with perturbations on u^x, u^y, B^x, B^y, and p:

$$(\delta u^x, \delta u^y) = \frac{\kappa}{2\pi} e^{0.5(1-r^2)}(-y, x), \qquad (\delta B^x, \delta B^y) = \frac{\mu}{2\pi} e^{0.5(1-r^2)}(-y, x),$$
$$\delta p = \frac{\mu^y(1-r^2) - \kappa^2}{8\pi^2} e^{1-r^2}.$$

The magnetic potential is initialized as

$$A^z = \frac{\mu}{2\pi} e^{0.5(1-r^2)}.$$

Here $r^2 = x^2 + y^2$.

We set the vortex strength $\mu = 5.389489439$ and $\kappa = \sqrt{2}\mu$ such that the lowest pressure in the center of the vortex is 5.3×10^{-12}. Similar to [48], we use computational domain $(x, y) \in [-10, 10] \times [-10, 10]$ such that the error from the boundary conditions will not influence the overall convergence study. The periodic boundary condition are used on all sides. Because fourth-order CT steps are used, the overall scheme is fourth-order accuracy.

The L_1-errors and L_∞-errors of the velocity and magnetic field for $t = 0.05$ are shown in Table 4.1, in which one can conclude the proposed positivity-preserving scheme can maintain fourth-order accuracy as expected. We remark that negative pressure is observed on meshes coarser than 320×320 when the limiter is not applied.

4.4.2.2 Smooth vortex test in hydrodynamics

In the previous example, we demonstrate the proposed scheme can attain the designed order of accuracy when there is very low pressure in the solution. In this example, we demonstrate the proposed scheme can also attain the designed order of the base MHD solver by the

Table 4.1: Accuracy test of the 2D vortex evolution in MHD. Shown are the L_1-errors and L_∞-errors at time $t = 0.05$ of the density as computed by the positivity-preserving WENO-CT2D scheme at various grid resolutions.

Mesh	u^x				u^y			
	L_1-error	order	L_∞-error	order	L_1-error	order	L_∞-error	order
40×40	7.38e-04	-	1.79e-02	-	8.03e-04	-	1.94e-02	-
80×80	7.20e-05	3.35	4.33e-03	2.05	7.36e-05	3.45	5.22e-03	1.90
160×160	3.46e-06	4.38	1.92e-04	4.49	3.72e-06	4.31	2.18e-04	4.58
320×320	1.80e-07	4.27	1.42e-05	3.76	1.96e-07	4.25	1.64e-05	3.73

Mesh	B^x				B^y			
	L_1-error	order	L_∞-error	order	L_1-error	order	L_∞-error	order
40×40	1.02e-03	-	1.49e-02	-	1.04e-03	-	1.57e-02	-
80×80	7.73e-05	3.73	1.27e-03	3.56	7.73e-05	3.75	1.16e-03	3.77
160×160	4.75e-06	4.03	8.25e-05	3.94	4.74e-06	4.03	7.16e-05	4.01
320×320	2.85e-07	4.06	7.66e-06	3.43	2.84e-07	4.06	6.36e-06	3.49

2D vortex evolution problem from hydrodynamics, where there are very low density and pressure. The initial condition consists of a mean flow

$$(\rho, u^x, u^y, u^z, p, B^x, B^y, B^z) = (1, 1, 1, 0, 1, 0, 0, 0), \tag{4.38}$$

and perturbations on u^x, u^y and the temperature $T = p/\rho$:

$$(\delta u^x, \delta u^y) = \frac{\epsilon}{2\pi} e^{0.5(1-r^2)}(-y, x),$$
$$\delta T = -\frac{(\gamma-1)\epsilon^2}{8\gamma\pi^2} e^{1-r^2},$$

with no perturbation in the entropy $S = p/\rho^\gamma$. Here $r^2 = x^2+y^2$. In this case, we let $\gamma = 1.4$. The computational domain is $(x, y) \in [-5, 5] \times [-5, 5]$ with periodic boundary condition on all sides. We set the vortex strength $\epsilon = 10.0828$ such that the lowest density and lowest pressure in the center of the vortex are 7.8×10^{-15} and 1.7×10^{-20} respectively. The exact

Table 4.2: Accuracy test of the 2D vortex evolution in hydrodynamics. Shown are the L_1-errors and L_∞-errors at time $t = 0.05$ of the density as computed by the positivity-preserving WENO-CT2D scheme with CT steps turned off. The solutions converge at fifth-order accuracy.

Mesh	L_1-error	order	L_∞-error	order
40×40	6.22e-03	-	2.30e-01	-
80×80	5.64e-04	3.46	3.98e-02	2.53
160×160	1.09e-05	5.69	1.16e-03	5.10
320×320	1.79e-07	5.93	2.75e-05	5.40
640×640	4.92e-09	5.19	8.71e-07	4.98

solution to this problem is just the convection of the vortex with the mean velocity.

We remark that the magnetic field is initialized as zero and the exact magnetic field will be zero for all the future time. Although the numerical solutions by the MHD solver has a nonzero magnetic field, the affect of the computed magnetic field to the whole system is insignificant compared to the other quantities. As a result, the influence of CT steps to the results is negligible for this case. We solve this problem with the positivity-preserving WENO-CT2D scheme with CT steps turned off. The L_1-errors and L_∞-errors of the density at $t = 0.05$ are shown in Table 4.2. We clearly observe a fifth-order convergence of the base schemes. We remark that negative density or pressure is observed during the computation of all the meshes in the table when the proposed limiter is not applied.

4.4.2.3 Rotated vacuum shock tube problem

In this example, we consider the vacuum shock tube problem rotated by an angle of α in a 2D domain. The initial conditions in this case are

$$(\rho, u^\perp, u^\parallel, u^z, p, B^\perp, B^\parallel, B^z) = \begin{cases} (10^{-12}, 0, 0, 0, 10^{-12}, 0, 0, 0) & \text{if} \quad \xi < 0, \\ (1, 0, 0, 0, 0.5, 0, 1, 0) & \text{if} \quad \xi > 0. \end{cases} \tag{4.39}$$

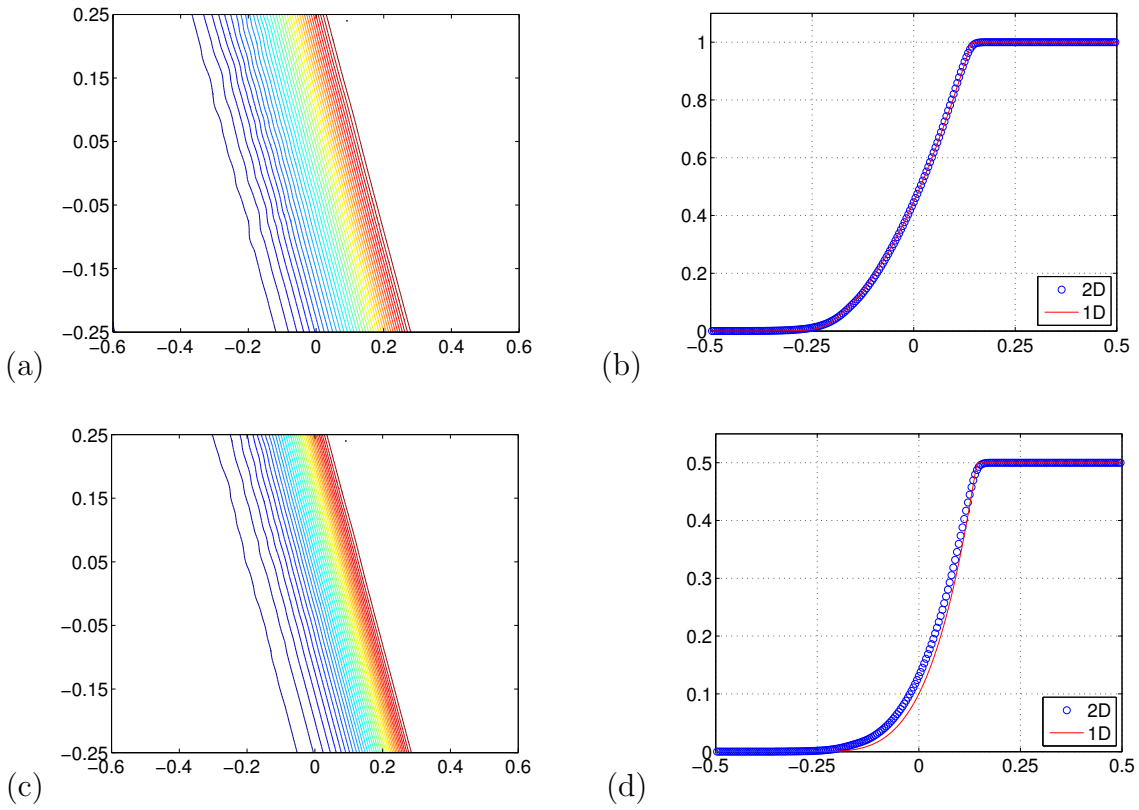

Figure 4.4: Rotated vacuum shock tube problem. Shown in these panels are plots at time $t = 0.1$ of (a) ρ, (b) ρ cut at y $= 0$, (c) the thermal pressure and (d) the thermal pressure cut at y $= 0$. 40 equally spaced contours are used for the contour plots. The solid lines in (b) and (d) are 1D highly resolved solutions. The solution was obtained on a 240×100 mesh.

where

$$\xi = x\cos\alpha + y\sin\alpha \quad \text{and} \quad \eta = -x\sin\alpha + y\cos\alpha, \tag{4.40}$$

where $u^{\perp}$ and $B^{\perp}$ are perpendicular to the shock interface, and $u^{\parallel}$ and $B^{\parallel}$ are parallel to the shock interface. The magnetic potential is initialized as

$$A^z(0,\xi) = \begin{cases} 0 & \text{if} \quad \xi \le 0, \\ -\xi & \text{if} \quad \xi \ge 0. \end{cases} \tag{4.41}$$

We solve this problem by the positivity-preserving WENO-CT2D scheme on the computational domain $(x, y) \in [-0.6, 0.6] \times [-0.25, 0.25]$ with a 240×100 mesh. $\alpha = \tan^{-1}(0.5)$. Zero-order extrapolation boundary conditions are used on the left and right boundaries. On the top and bottom boundaries, all the quantities are set to describe the exact motion of the shock.

The solutions are plotted in Figure 4.4, where the 1D cut of density and pressure at $y = 0$ is also plotted to compare with the 1D highly resolved results. We clearly observe that the 2D solution is consistent with the 1D solution. Without the limiter, negative density and pressure are observed in numerical solutions, which quickly leads to blow-up of the numerical simulation.

4.4.2.4 2D blast problem

In the blast wave problem, a strong fast magnetosonic shock formulates and propagates into the low-β plasma background, which will likely lead to negative density or pressure in numerical solutions. In this subsection, we first investigate a 2D version of the problem [8, 10, 49]. The computational domain is $(x, y) \in [-0.5, 0.5] \times [-0.5, 0.5]$ with outflow boundary conditions on all the four sides.

The initial conditions of the problem consist of an initial background:

$$(\rho, u^x, u^y, u^z, p, B^x, B^y, B^z) = (1, 0, 0, 0, 0.1, 100/\sqrt{8\pi}, 100/\sqrt{8\pi}, 0), \tag{4.42}$$

and a circular pressure pulse $p = 1000$ within a radius $r = 0.1$ from the center of the domain.

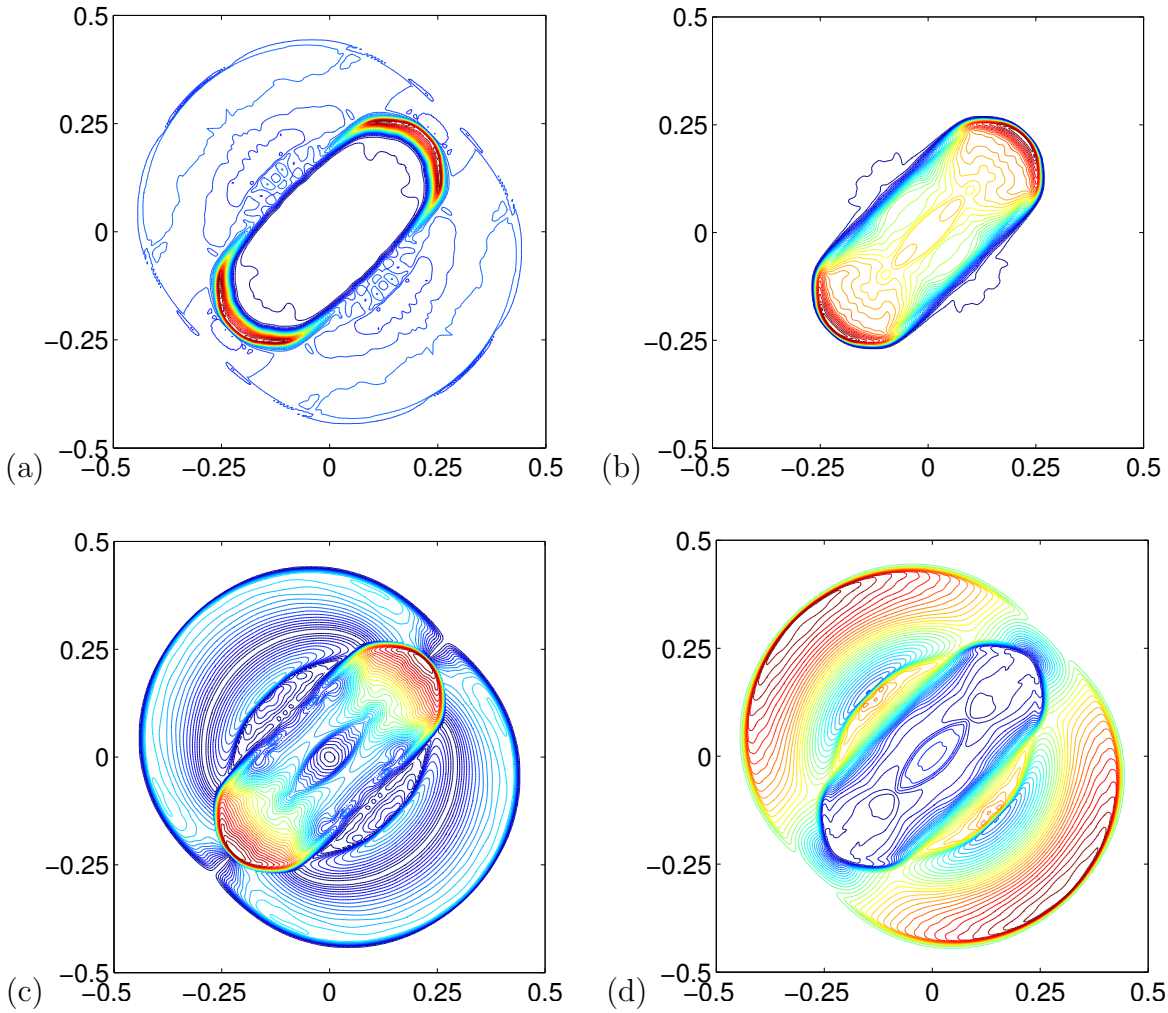

Figure 4.5: 2D blast problem. Shown in these panels are plots at time $t = 0.01$ of (a) ρ, (b) the thermal pressure, (c) the norm of $\mathbf{u}$ and (d) the magnetic pressure. 40 equally spaced contours are used for each plot. The solution was obtained on a 256×256 mesh by positivity-preserving WENO-CT scheme.

The initial scalar magnetic potential is simply given by

$$A^z = 100/\sqrt{8\pi}y - 100/\sqrt{8\pi}x. \tag{4.43}$$

The solution is computed on a 256×256 mesh. Shown in Figure 4.5 are plots of the solution.

The solution shows good agreement with those in [8, 49].

In Table 4.3, we use this example to compare four different schemes, WENO-HCL,

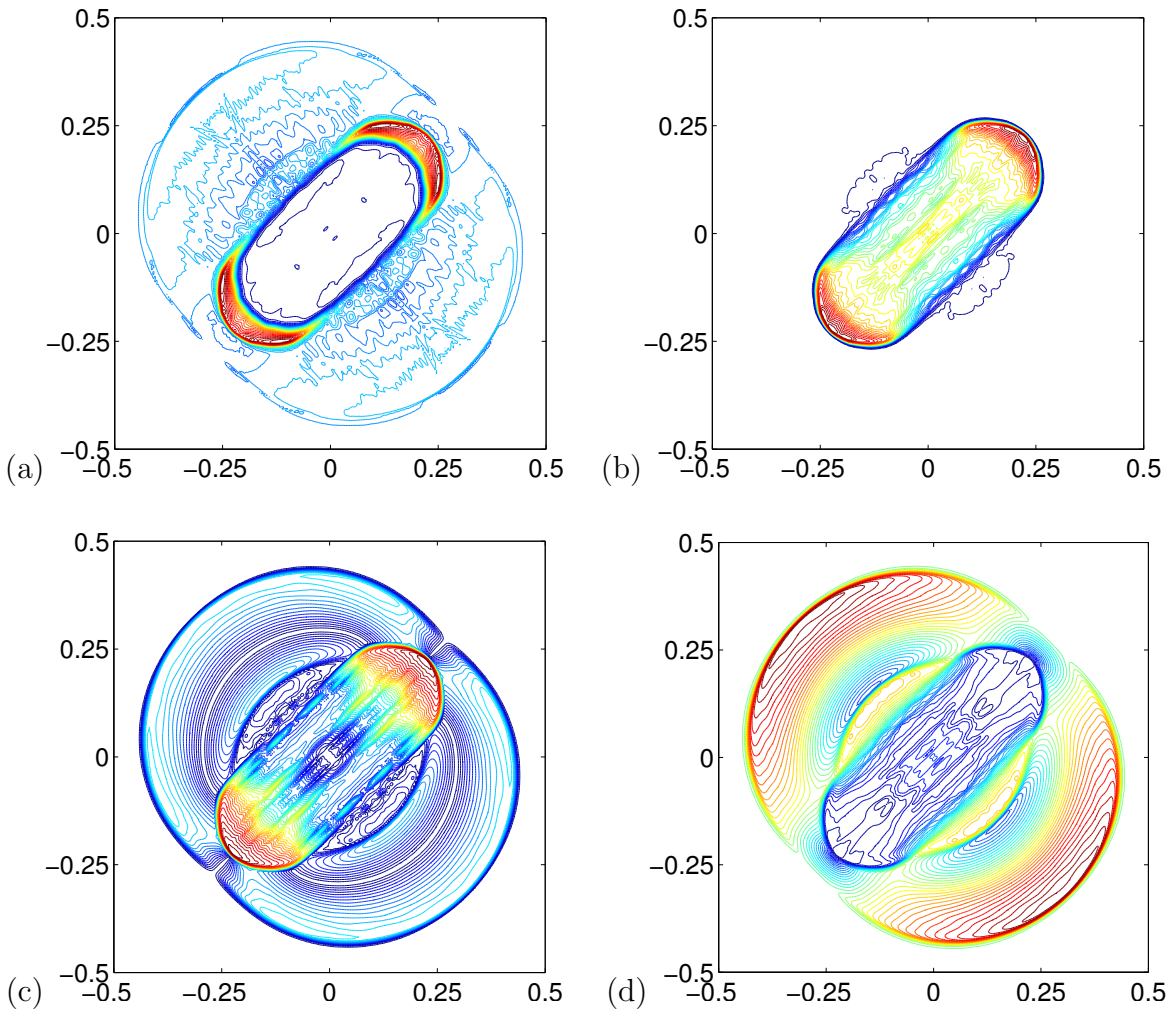

Figure 4.6: 2D blast problem. Shown in these panels are plots at time $t = 0.01$ of (a) ρ, (b) the thermal pressure, (c) the norm of $\mathbf{u}$ and (d) the magnetic pressure. 40 equally spaced contours are used for each plot. The solution was obtained on a 256×256 mesh by the WENO-HCL scheme.

WENO-CT-OP1, WENO-CT-OP2 and PP-WENO-CT-OP2. Here WENO-HCL is referred to the base WENO-HCL scheme without CT or the limiter. WENO-CT-OP1 is referred to the WENO-CT2D scheme choosing **Option 1** without the limiter. WENO-CT-OP2 is referred to the WENO-CT2D scheme choosing **Option 2** without the limiter. Finally, PP-WENO-CT-OP2 is referred to the positivity-preserving WENO-CT2D scheme with **Option 2** chosen. From Table 4.3, we observe that the base WENO-HCL scheme is unstable for

Table 4.3: Comparisons of different schemes solving the 2D blast problem. The column of **P** indicates whether the numerical solutions remain positive in the simulations. The column of **S** indicates whether the simulations run stably to $t = 0.01$. In order to make a fair comparison, the positivity of density and pressure is only checked at each time step t^n.

Mesh	WENO-HCL		WENO-CT-OP1		WENO-CT-OP2		PP-WENO-CT-OP2	
	P	**S**	**P**	**S**	**P**	**S**	**P**	**S**
150×150	No	No	No	No	No	Yes	Yes	Yes
200×200	No	Yes	No	No	No	Yes	Yes	Yes
256×256	No	Yes	No	No	No	No	Yes	Yes

the resolution 150×150 and becomes stable in the higher resolutions. WENO-CT-OP1 is unstable for each resolution and applying the positivity-preserving limiter will not be able to stabilize this because the negative pressure is from the correction step of the magnetic field. WENO-CT-OP2 is stable in the lower resolution but becomes unstable for the resolution 256×256, and negative pressure is observed in all the resolutions. Finally, the positivity-preserving WENO-CT scheme is stable for all the resolutions. From those results, it is very clear that the positivity-preserving WENO-CT scheme is the most stable method in these four methods.

Another concern for this CT framework is that the energy is not conserving in our positivity-preserving WENO-CT scheme due to **Option 2**. We also use this example to study this issue. We compare the results by the base WENO-HCL scheme and the positivity-preserving WENO-CT scheme. In Figure 4.6, we show the results by the base WENO-HCL scheme with the same resolution as Figure 4.5. The results look similar to those by the positivity-preserving WENO-CT scheme, except there are some unphysical oscillations around the center region in Figure 4.6. That is due to the divergence error in the base scheme. If we plot the divergence error in the time domain, we can clearly see that the divergence error of the positivity-preserving WENO-CT scheme stays around 10^{-12}, while the error of

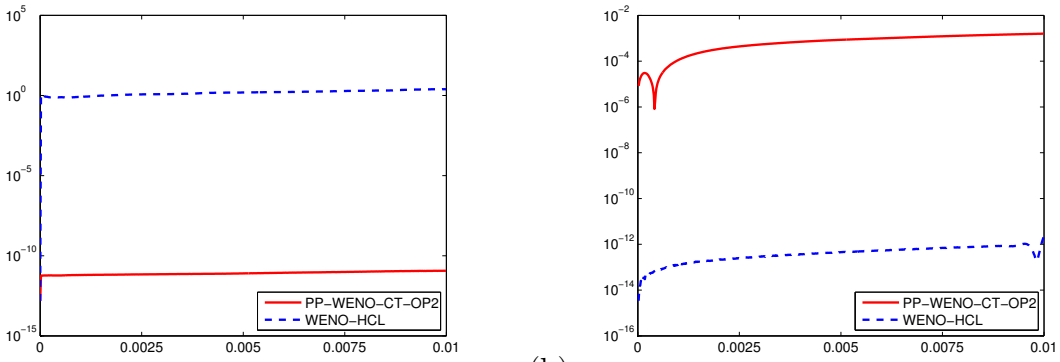

(a) (b)

Figure 4.7: Comparisons between WENO-HCL scheme and positivity-preserving WENO-CT scheme for the 2D blast problem. Shown in these panels are plots of (a) the divergence error and (b) the relative error of the total energy in the whole domain. The x-axis denotes the time $t \in [0, 0.01]$.

the WENO-HCL scheme is around 10^0 during the simulation. Here the divergence error is defined as L_1-norm of $\nabla \cdot \mathbf{B}$, where the numerical $\nabla\cdot$ operator is defined as a regular fourth-order central finite difference discretization. As a common drawback in the CT framework when **Option 2** is chosen, the correction step leads to a loss of the conservation of the total energy.

To study this issue, we compute the total energies in the whole domain solved by two schemes and compare them with the initial numerical value. The results are plotted in Figure 4.7. We can see the relative error of the positivity-preserving scheme is around 10^{-3}, while the conservative WENO-HCL scheme has an error about 10^{-12}. On the other hand, when we perform a convergence study for the total energy in the whole domain, a first-order convergence has been observed for the positivity-preserving scheme when the computed total energies are compared with the exact value, although the scheme is not energy-conserving. However, we remark that the conservation of energy is important for some problems, such as those involving nonlinear strong discontinuities. A high-order positivity-

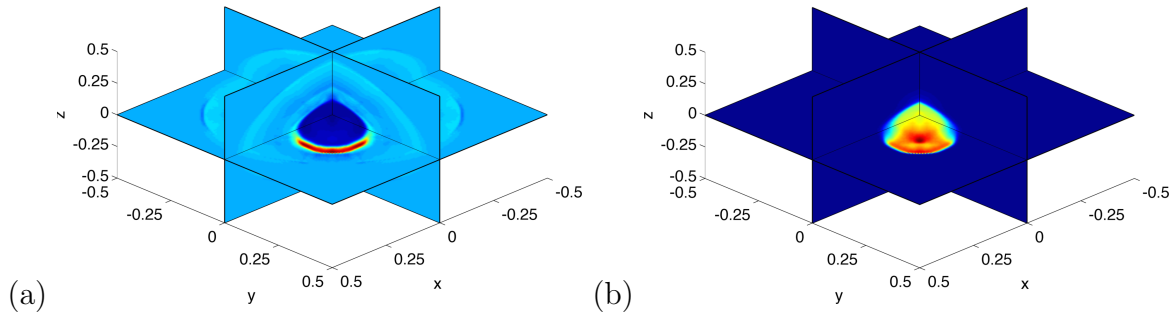

Figure 4.8: 3D blast problem. Shown in these panels are 3D plots at time $t = 0.01$ of (a) ρ and (b) the thermal pressure. The solution was obtained on a $150 \times 150 \times 150$ mesh.

preserving conservative scheme with the divergence error being controlled will be part of our future work. However, it is very difficult, if not impossible, in the CT framework to satisfy all the requirements simultaneously. A better way to control the divergence error is needed for this purpose.

4.4.2.5 3D blast problem

The last problem we investigate is a fully 3D version of the blast problem. It is used to test the behavior of the positivity-preserving WENO-CT3D scheme. The initial conditions consist of an initial background,

$$(\rho, u^x, u^y, u^z, p, B^x, B^y, B^z) = (1, 0, 0, 0, 0.1, 100/\sqrt{8\pi}, 100/\sqrt{8\pi}, 0), \tag{4.44}$$

and a spherical pressure pulse $p = 1000$ within a radius $r = 0.1$ from the center of the domain. The initial conditions for the magnetic potential are

$$\mathbf{A}(0, x, y, z) = (0, 0, 100/\sqrt{8\pi}y - 100/\sqrt{8\pi}x). \tag{4.45}$$

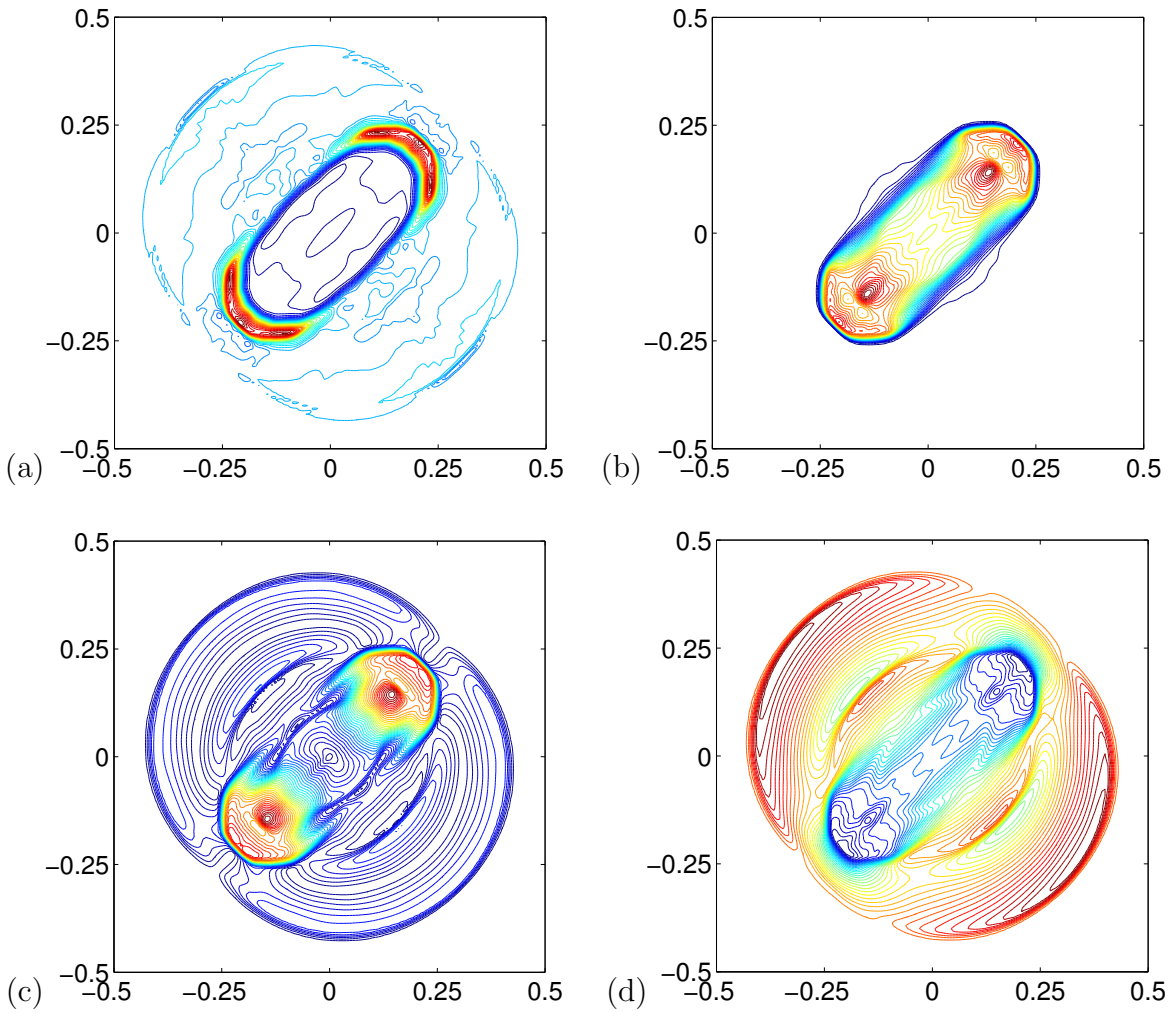

Figure 4.9: 3D blast problem. Shown in these panels are plots at time $t = 0.01$ and cut at $z = 0$ of (a) ρ, (b) the thermal pressure, (c) the norm of $\mathbf{u}$ and (d) the magnetic pressure. 40 equally spaced contours are used for each plot. The solution was obtained on a $150\times150\times150$ mesh.

The computational domain is $[-0.5, 0.5]^3$. Outflow boundary conditions are used on all sides. The numerical simulation is performed on a $150 \times 150 \times 150$ mesh. To distinguish this 3D case from the 2D blast case, we present the 3D plots of the density and pressure in Figure 4.8, which clearly indicates its spherical structures. In Figure 4.9 we show the results of the solutions cut at $z = 0$. The solution is comparable to the 3D results in [31, 53, 85]. We note that negative pressure is observed at time $t = 0.0033$ if the positivity-preserving

limiter is not applied.

Chapter 5

Conclusion and future work

5.1 Conclusion

In this work we developed a class of finite difference methods for solving the ideal MHD equations. A summary of the key features of the proposed numerical method are listed below:

1. All quantities, including all components of the magnetic field and magnetic potential, are treated as point values on the same mesh (i.e., there is no mesh staggering).

2. The base scheme is the fifth-order FD-WENO scheme of Jiang and Shu [39]. With this method we are able to achieve high-order using dimension-by-dimension finite difference operators, instead of the more complicated spatial integration and multidimensional reconstructions used by Helzel *et al.* [35].

3. The corrected magnetic field is computed via fourth-order accurate central finite difference operators that approximate the curl of the magnetic vector potential. These operators are chosen to produce a corrected magnetic field that exactly satisfies a discrete divergence-free condition.

4. All time-stepping is done with the SSP-RK methods. In Chapter 3, we use a fourth-order version and in Chapter 4 we use a third-order version.

5. Using a particular gauge condition, the magnetic vector potential is made to satisfy a weakly hyperbolic, non-conservative, hyperbolic system. This system is solved using a modified version of the FD-WENO scheme developed for Hamilton–Jacobi equations [38]. For 3D problems, special limiters based on artificial resistivity are introduced to help control unphysical oscillations in the magnetic field.

6. A positivity-preserving limiter is proposed and applied by modifying high-order WENO-HCL flux with the first-order Lax–Friedrichs flux so as to produce positive density and pressure.

In Chapter 3 the numerical methods were tested on several 2D, 2.5D, and 3D test problems, all of which demonstrate the robustness of our approach. On smooth problems, we achieve fourth-order accuracy in all components, including the magnetic field and the magnetic potential. For problems with shocks, we are able to accurately capture the shock waves without introducing unphysical oscillations in any of the solution components. In addition, the cloud-shock interaction problems also indicated that there is a possible advantage of using a high-order method compared to traditional second-order methods. For instance, using a 128×128 mesh in our methods, we are able to see the same structures that can only be observed by a second-order finite volume methods on much finer grid resolutions. This phenomenon is observed in both 2D and 3D. Another advantage of the proposed methods is that they do not involve any multidimensional reconstructions in any step, while traditional high-order finite volume methods commonly need several multidimensional reconstructions in each grid cell. For instance, for the same resolution on a 3D simulation, our finite difference code uses less CPU time than the third-order finite volume code in [35].

In Chapter 4 we demonstrated the effectiveness and efficiency of the resulting positivity-preserving schemes with 1D, 2D and 3D problems. Through smooth problems, we showed the proposed limiter will maintain the designed order of accuracy of the base schemes. We also tested the schemes with several practical problems such as the low-β problems and found the proposed limiter can increase the numerical stability of the schemes. In particular, we also studied the effect of energy correction steps in the constrained transport method by a blast wave problem.

5.2 Future work

The numerical schemes as developed so far can only be used to solve problems on either a uniform grid or on a smoothly varying mapped grid, which is a common disadvantage of FD ENO/WENO schemes. Thus, our methods are less flexible compared to the finite volume CT methods developed in [35], in which the scheme has been successfully extended to non-smoothly varying grids. However, a promising approach for overcoming this restriction is to place the existing WENO-CT method for ideal MHD into an AMR framework. Since our methods are fully explicit and fully unstaggered, it is possible to incorporate them into the WENO-AMR framework developed by Shen *et al.* [66]. To better achieve the goal, currently we are working on a high-order single-step single-stage ideal MHD solver by extending the work in [63].

In addition to AMR application, we are also interested in including non-ideal terms, such as Hall term and resistivity term, into the ideal MHD solver so that it can simulate more physical phenomena such as magnetic reconnection. The non-ideal term will potentially become very stiff if its effect is significant for the system. Consequently, this term needs

to be treated implicitly and one may need other time stepping approaches such as implicit-explicit time integration methods and fully implicit methods. Recently, we have been also applying the proposed schemes to several practical problems, such as simulating gas-puff Z-pinch plasmas.

APPENDIX

WENO reconstruction

The main idea of WENO reconstruction is to compute a finite difference stencil using a weighted average of several smaller stencils. The weights are chosen based on the smoothness of the solution on each of the smaller stencils. The full procedure can be found in [39, 64, 67, 68]. For completeness, we also include a brief description of the 5^{th}-order WENO reconstruction as used in this work and define the operator Φ_{WENO5} that was used in Section 3.1.

We consider the problem on a uniform grid with $N+1$ grid points,

$$a = x_{\frac{1}{2}} < x_{\frac{3}{2}} < \cdots < x_{N+\frac{1}{2}} = b, \tag{1}$$

and let the cell averages of some function $h(x)$ on the interval $I_i = \left(x_{i-\frac{1}{2}}, x_{i+\frac{1}{2}}\right)$ be denoted by

$$\bar{h}_i = \frac{1}{\Delta x} \int_{x_{i-\frac{1}{2}}}^{x_{i+\frac{1}{2}}} h(x)\, dx. \tag{2}$$

We would like to approximate the value of $h(x)$ at the half node $x_{i+\frac{1}{2}}$ by WENO reconstruction on the stencil: $S = \{I_{i-2}, I_{i-1}, \ldots, I_{i+2}\}$. There are three sub-stencils for node $x_{i+\frac{1}{2}}$: $S_0 = \{I_{i-2}, I_{i-1}, I_i\}$, $S_1 = \{I_{i-1}, I_i, I_{i+1}\}$ and $S_2 = \{I_i, I_{i+1}, I_{i+2}\}$. Through a simple Taylor expansions of $h(x)$, we can obtain 3^{rd}-order accurate approximations of $h^{(i)}_{i+\frac{1}{2}}$ on each

sub-stencil S_i as follows:

$$h^{(0)}_{i+\frac{1}{2}} = \frac{1}{3}\bar{h}_{i-2} - \frac{7}{6}\bar{h}_{i-1} + \frac{11}{6}\bar{h}_i, \tag{3}$$

$$h^{(1)}_{i+\frac{1}{2}} = -\frac{1}{6}\bar{h}_{i-1} + \frac{5}{6}\bar{h}_i + \frac{1}{3}\bar{h}_{i+1}, \tag{4}$$

$$h^{(2)}_{i+\frac{1}{2}} = \frac{1}{3}\bar{h}_i + \frac{5}{6}\bar{h}_{i+1} - \frac{1}{6}\bar{h}_{i+2}. \tag{5}$$

The approximation $h_{i+\frac{1}{2}}$ is then defined as a linear convex combination of the above three approximations:

$$h_{i+\frac{1}{2}} = w_0\, h^{(0)}_{i+\frac{1}{2}} + w_1\, h^{(1)}_{i+\frac{1}{2}} + w_2\, h^{(2)}_{i+\frac{1}{2}}, \tag{6}$$

where the nonlinear weights are defined as

$$w_j = \frac{\tilde{w}_j}{\tilde{w}_0 + \tilde{w}_1 + \tilde{w}_2}, \tag{7}$$

$$\tilde{w}_0 = \frac{1}{(\epsilon + \beta_0)^2}, \quad \tilde{w}_1 = \frac{6}{(\epsilon + \beta_1)^2}, \quad \tilde{w}_2 = \frac{3}{(\epsilon + \beta_2)^2}. \tag{8}$$

In our computations we take $\epsilon = 10^{-6}$ and the smoothness indicator parameters, β_i, are chosen as in [39]:

$$\beta_0 = \frac{13}{12}(\bar{h}_{i-2} - 2\bar{h}_{i-1} + \bar{h}_i)^2 + \frac{1}{4}(\bar{h}_{i-2} - 4\bar{h}_{i-1} + 3\bar{h}_i)^2, \tag{9}$$

$$\beta_1 = \frac{13}{12}(\bar{h}_{i-1} - 2\bar{h}_i + \bar{h}_{i+1})^2 + \frac{1}{4}(\bar{h}_{i-1} - \bar{h}_{i+1})^2, \tag{10}$$

$$\beta_2 = \frac{13}{12}(\bar{h}_i - 2\bar{h}_{i+1} + \bar{h}_{i+2})^2 + \frac{1}{4}(3\bar{h}_i - 4\bar{h}_{i+1} + \bar{h}_{i+2})^2. \tag{11}$$

From these we define Φ_{WENO5} in Section 3.1 as follows:

$$\Phi_{\text{WENO5}}(\bar{h}_{i-2}, \bar{h}_{i-1}, \bar{h}_i, \bar{h}_{i+1}, \bar{h}_{i+2}) := w_0\, h^{(0)}_{i+\frac{1}{2}} + w_1\, h^{(1)}_{i+\frac{1}{2}} + w_2\, h^{(2)}_{i+\frac{1}{2}}. \tag{12}$$

The approximation value $h_{i+\frac{1}{2}}$ has the following properties:

1. If $h(x)$ is smooth in the full stencil S, $h_{i+\frac{1}{2}}$ is a 5^{th}-order accurate approximation to the value $h\left(x_{i+\frac{1}{2}}\right)$.

2. If $h(x)$ is not smooth or has discontinuity in the full stencil S, the nonlinear weights are computed in such a way that $h_{i+\frac{1}{2}}$ is mainly reconstructed from the locally smoothest sub-stencil. Consequently, the spurious oscillations can be effectively controlled.

BIBLIOGRAPHY

BIBLIOGRAPHY

[1] D.S. Balsara. Divergence-free adaptive mesh refinement for magnetohydrodynamics. *J. Comput. Phys.*, 174:614–648, 2001.

[2] D.S. Balsara. Total variation diminishing scheme for relativistic magnetohydrodynamics. *Astrophys. J. Suppl.*, 132:83–101, 2001.

[3] D.S. Balsara. Second-order-accurate schemes for magnetohydrodynamics with divergence-free reconstruction. *Astrophys. J. Suppl.*, 151:149–184, 2004.

[4] D.S. Balsara. Divergence-free reconstruction of magnetic fields and WENO schemes for magnetohydrodynamics. *J. Comput. Phys.*, 228:5040—5056, 2009.

[5] D.S. Balsara. Self-adjusting, positivity preserving high order schemes for hydrodynamics and magnetohydrodynamics. *J. Comput. Phys.*, 231:7504–7517, 2012.

[6] D.S. Balsara and J. Kim. A comparison between divergence-cleaning and staggered-mesh formulations for numerical magnetohydrodynamics. *Astrophys. J.*, 602:1079–1090, 2004.

[7] D.S. Balsara, C. Meyer, M. Dumbser, H. Du, and Z. Xu. Efficient implementation of ADER schemes for Euler and magnetohydrodynamical flows on structured meshes – Speed comparisons with Runge–Kutta methods. *J. Comput. Phys.*, 235:934–969, 2013.

[8] D.S. Balsara, T. Rumpf, M. Dumbser, and C.-D. Munz. Efficient, high accuracy ADER-WENO schemes for hydrodynamics and divergence-free magnetohydrodynamics. *J. Comput. Phys.*, 228:2480—2516, 2009.

[9] D.S. Balsara and D. Spicer. Maintaining pressure positivity in magnetohydrodynamic simulations. *J. Comput. Phys.*, 148(1):133–148, 1999.

[10] D.S. Balsara and D. Spicer. A staggered mesh algorithm using high order Godunov fluxes to ensure solenoidal magnetic fields in magnetohydrodynamic simulations. *J. Comput. Phys.*, 149(2):270–292, 1999.

[11] T.J. Barth. Numerical methods for gasdynamic systems on unstructured meshes. In *An introduction to recent developments in theory and numerics for conservation laws*, pages 195–285. Springer, 1999.

[12] J. Bell, M. Berger, J. Saltzman, and M. Welcome. Three-dimensional adaptive mesh refinement for hyperbolic conservation laws. *SIAM J. Sci. Comput.*, 15(1):127–138, 1994.

[13] M.J. Berger and P. Colella. Local adaptive mesh refinement for shock hydrodynamics. *J. Comput. Phys.*, 82:64–84, 1989.

[14] M.J. Berger and R.J. LeVeque. Adaptive mesh refinement using wave-propagation algorithms for hyperbolic systems. *SIAM J. Numer. Anal.*, 35:2298–2316, 1998.

[15] M.J. Berger and J. Oliger. Adaptive mesh refinement for hyperbolic partial differential equations. *J. Comput. Phys.*, 53:484–512, 1984.

[16] J.U. Brackbill and D.C. Barnes. The effect of nonzero $\nabla \cdot B$ on the numerical solution of the magnetohydrodynamic equations. *J. Comput. Phys.*, 35:426–430, 1980.

[17] M. Brio and C.C. Wu. An upwind differencing scheme for the equations of ideal magnetohydrodynamics. *J. Comput. Phys.*, 75:400–422, 1988.

[18] P. Cargo and G. Gallice. Roe matrices for ideal MHD and systematic construction of Roe matrices for systems of conservation laws. *J. Comput. Phys.*, 136:446–466, 1997.

[19] Y. Cheng, F. Li, J. Qiu, and L. Xu. Positivity-preserving DG and central DG methods for ideal MHD equations. *J. Comput. Phys.*, 238:255–280, 2013.

[20] A.J. Christlieb, Y. Liu, Q. Tang, and Z. Xu. High order parametrized maximum-principle-preserving and positivity-preserving WENO schemes on unstructured meshes. *J. Comput. Phys.*, 281(0):334–351, 2015.

[21] A.J. Christlieb, Y. Liu, Q. Tang, and Z. Xu. Positivity-preserving finite difference weighted ENO schemes with constrained transport for ideal magnetohydrodynamic equations. *SIAM J. Sci. Comput.*, to appear, 2015. `http://arxiv.org/abs/1406.5098`.

[22] A.J. Christlieb, J.A. Rossmanith, and Q. Tang. Finite difference weighted essentially non-oscillatory schemes with constrained transport for ideal magnetohydrodynamics. *J. Comput. Phys.*, 268:302–325, 2014.

[23] B. Cockburn and C.-W. Shu. TVB Runge-Kutta local projection discontinuous Galerkin finite element method for scalar conservation laws II: General framework. *Math. Comp.*, 52:411–435, 1989.

[24] C. Dafermos. *Hyperbolic Conservation Laws in Continuum Physics*. Springer, 2010.

[25] W. Dai and P.R. Woodward. A simple finite difference scheme for multidimensional magnetohydrodynamical equations. *J. Comput. Phys.*, 142(2):331–369, 1998.

[26] A. Dedner, F. Kemm, D. Kröner, C.-D. Munz, T. Schnitzer, and M. Wesenberg. Hyperbolic divergence cleaning for the MHD equations. *J. Comput. Phys.*, 175:645–673, 2002.

[27] C.R. DeVore. Flux-corrected transport techniques for multidimensional compressible magnetohydrodynamics. *J. Comput. Phys.*, 92:142–160, 1991.

[28] C. Evans and J.F. Hawley. Simulation of magnetohydrodynamic flow: A constrained transport method. *Astrophys. J.*, 332:659–677, 1988.

[29] M. Fey and M. Torrilhon. A constrained transport upwind scheme for divergence-free advection. In T.Y. Hou and E. Tadmor, editors, *Hyperbolic Problems: Theory, Numerics, and Applications*, pages 529–538. Springer, 2003.

[30] S. Fromang, P. Hennebelle, and R. Teyssier. A high order godunov scheme with constrained transport and adaptive mesh refinement for astrophysical magnetohydrodynamics. *Astronomy and Astrophysics*, 457(2):371–384, 2006.

[31] T.A. Gardiner and J.M. Stone. An unsplit Godunov method for ideal MHD via constrained transport in three dimensions. *J. Comput. Phys.*, 227(8):4123–4141, 2008.

[32] H. Grad. On the kinetic theory of rarefied gases. *Comm. Pure Appl. Math.*, 2(4):331–407, 1949.

[33] A. Harten, B. Engquist, S. Osher, and S.R. Chakravarthy. Uniformly high order accurate essentially non-oscillatory schemes, III. *J. Comput. Phys.*, 71(2):231–303, 1987.

[34] C. Helzel, J.A. Rossmanith, and B. Taetz. An unstaggered constrained transport method for the 3D ideal magnetohydrodynamic equations. *J. Comput. Phys.*, 227:9527–9553, 2011.

[35] C. Helzel, J.A. Rossmanith, and B. Taetz. A high-order unstaggered constrained-transport method for the three-dimensional ideal magnetohydrodynamic equations based on the method of lines. *SIAM J. Sci. Comput.*, 35(2):A623–A651, 2013.

[36] X.Y. Hu, N.A. Adams, and C.-W. Shu. Positivity-preserving method for high-order conservative schemes solving compressible Euler equations. *J. Comput. Phys.*, 242:169–180, 2013.

[37] P. Janhunen. A positive conservative method for magnetohydrodynamics based on HLL and Roe methods. *J. Comput. Phys.*, 160(2):649–661, 2000.

[38] G.-S. Jiang and D. Peng. Weighted ENO schemes for Hamilton–Jacobi equations. *SIAM J. Sci. Comput.*, 21(6):2126–2143, 2000.

[39] G.-S. Jiang and C.-W. Shu. Efficient implementation of weighted ENO schemes. *J. Comput. Phys.*, 126:202–228, 1996.

[40] G.-S. Jiang and C.-C. Wu. A high-order WENO finite difference scheme for the equations of ideal magnetohydrodynamics. *J. Comput. Phys.*, 150(2):561–594, 1999.

[41] E.A. Johnson. *Gaussian-Moment Relaxation Closures for Verifiable Numerical Simulation of Fast Magnetic Reconnection in Plasma*. PhD thesis, University of Wisconsin, 2012.

[42] S. Kawai. Divergence-free-preserving high-order schemes for magnetohydrodynamics: An artificial magnetic resistivity method. *J. Comput. Phys.*, 251:292—318, 2013.

[43] D.I. Ketcheson. Highly efficient strong stability-preserving Runge-Kutta methods with low-storage implementations. *SIAM J. Sci. Comput.*, 30:2113–2136, 2008.

[44] A.M. Khokhlov. Fully threaded tree algorithms for adaptive refinement fluid dynamics simulations. *J. Comput. Phys.*, 143(2):519–543, 1998.

[45] R.J. LeVeque. Wave propagation algorithms for multi-dimensional hyperbolic systems. *J. Comput. Phys.*, 131:327–335, 1997.

[46] C.D. Levermore. Moment closure hierarchies for kinetic theories. *J. Stat. Phys.*, 83(5-6):1021–1065, 1996.

[47] F. Li and C.-W. Shu. Locally divergence-free discontinuous Galerkin methods for MHD equations. *J. Sci. Comput.*, 22:413–442, 2005.

[48] F. Li and L. Xu. Arbitrary order exactly divergence-free central discontinuous Galerkin methods for ideal MHD equations. *J. Comput. Phys.*, 231(6):2655–2675, 2012.

[49] F. Li, L. Xu, and S. Yakovlev. Central discontinuous Galerkin methods for ideal MHD equations with the exactly divergence-free magnetic field. *J. Comput. Phys.*, 230:4828–4847, 2011.

[50] X.D. Liu, S. Osher, and T. Chan. Weighted essentially non-oscillatory schemes. *J. Comput. Phys.*, 115(1):200–212, 1994.

[51] P. Londrillo and L. Del Zanna. High-order upwind schemes for multidimensional magnetohydrodynamics. *Astrophys. J.*, 530:508–524, 2000.

[52] P. Londrillo and L. Del Zanna. On the divergence-free condition in Godunov-type schemes for ideal magnetohydrodynamics: the upwind constrained transport method. *J. Comput. Phys.*, 195:17–48, 2004.

[53] A. Mignone and P. Tzeferacos. A second-order unsplit Godunov scheme for cell-centered MHD: the CTU-GLM scheme. *J. Comput. Phys.*, 229:2117–2138, 2010.

[54] G.K. Parks. *Physics of Space Plasmas: An Introduction*. Westview Press, 2004.

[55] S. Popinet. Gerris: a tree-based adaptive solver for the incompressible Euler equations in complex geometries. *J. Comput. Phys.*, 190(2):572–600, 2003.

[56] K.G. Powell. An approximate Riemann solver for magnetohydrodynamics (that works in more than one dimension). Technical Report 94-24, ICASE, Langley, VA, 1994.

[57] K.G. Powell, P.L. Roe, T.J. Linde, T.I. Gombosi, and D.L. De Zeeuw. A solution-adaptive upwind scheme for ideal magnetohydrodynamics. *J. Comput. Phys.*, 154:284–309, 1999.

[58] J.A. Rossmanith. The MHDCLAW software package. Available from `http://www.public.iastate.edu/~rossmani/claw/MHDCLAW`.

[59] J.A. Rossmanith. A high-resolution constrained transport method with adaptive mesh refinement for ideal MHD. *Comp. Phys. Comm.*, 164:128–133, 2004.

[60] J.A. Rossmanith. An unstaggered, high-resolution constrained transport method for magnetohydrodynamic flows. *SIAM J. Sci. Comput.*, 28:1766–1797, 2006.

[61] J.A. Rossmanith. High-order discontinuous Galerkin finite element methods with globally divergence-free constrained transport for ideal MHD. *preprint, arXiv:1310.4251*, 2013.

[62] D.S. Ryu, F. Miniati, T.W. Jones, and A. Frank. A divergence-free upwind code for multidimensional magnetohydrodynamic flows. *Astrophys. J.*, 509(1):244–255, 1998.

[63] D.C. Seal, Y. Güçlü, and A.J. Christlieb. The Picard integral formulation of weighted essentially non-oscillatory schemes. *SIAM J. Numer. Anal.*, to appear, 2014. `http://arxiv.org/abs/1403.1282`.

[64] D.C. Seal, Y. Guclu, and A.J. Christlieb. High-order multiderivative time integrators for hyperbolic conservation laws. *J. Sci. Comput.*, 60(1):101–140, 2014.

[65] D.C. Seal, Q. Tang, Z. Xu, and A.J. Christlieb. An explicit high-order single-stage single-step positivity-preserving finite difference WENO method for the compressible euler equations,. *J. Sci. Comput.*, in revision, 2015. `http://arxiv.org/abs/1411.0328`.

[66] C. Shen, J.-M. Qiu, and A.J. Christlieb. Adaptive mesh refinement based on high order finite difference WENO scheme for multi-scale simulations. *J. Comput. Phys.*, 230(10):3780–3802, 2011.

[67] C.-W. Shu. Essentially non-oscillatory and weighted essentially non-oscillatory schemes for hyperbolic conservation laws. In *Advanced Numerical Approximation of Nonlinear Hyperbolic Equations*, pages 325–432. Springer, 1998.

[68] C.-W. Shu. High order weighted essentially nonoscillatory schemes for convection dominated problems. *SIAM Rev.*, 51(1):82–126, 2009.

[69] C.-W. Shu and S. Osher. Efficient implementation of essentially non-oscillatory shock-capturing schemes. *J. Comput. Phys.*, 77:439–471, 1988.

[70] C.-W. Shu and S. Osher. Efficient implementation of essentially non-oscillatory shock-capturing schemes, II. *J. Comput. Phys.*, 83(1):32–78, 1989.

[71] H. De Sterck. Multi-dimensional upwind constrained transport on unstructured grids for "shallow water" magnetohydrodynamics. In *Proceedings of the 15th AIAA Computational Fluid Dynamics Conference, Anaheim, California*, page 2623. AIAA, 2001.

[72] H. Struchtrup and M. Torrilhon. Regularization of Grad's 13 moment equations: derivation and linear analysis. *Phys. Fluids*, 15(9):2668–2680, 2003.

[73] M. Torrilhon. Locally divergence-preserving upwind finite volume schemes for magnetohydrodynamics. *SIAM J. Sci. Comput.*, 26:1166–1191, 2005.

[74] M. Torrilhon. Hyperbolic moment equations in kinetic gas theory based on multi-variate Pearson-IV-distributions. *Comm. Comput. Phys.*, 7(4):639–673, 2010.

[75] G. Tóth. The $\nabla \cdot B = 0$ constraint in shock-capturing magnetohydrodynamics codes. *J. Comput. Phys.*, 161:605–652, 2000.

[76] K. Waagan. A positive MUSCL-Hancock scheme for ideal magnetohydrodynamics. *J. Comput. Phys.*, 228(23):8609–8626, 2009.

[77] R. Wang and R. Spiteri. Linear instability of the fifth-order WENO method. *SIAM J. Numer. Anal.*, 45(5):1871–1901, 2007.

[78] T. Xiong, J.-M. Qiu, and Z. Xu. Parametrized positivity preserving flux limiters for high order finite difference WENO scheme solving compressible Euler equations. *preprint, arXiv:1403.0594*, 2014.

[79] Z. Xu. Parametrized maximum principle preserving flux limiters for high order schemes solving hyperbolic conservation laws: one-dimensional scalar problem. *Math. Comp.*, 83(289):2213–2238, 2014.

[80] Z. Xu and D. Balsara. Divergence-free WENO reconstruction-based finite volume scheme for solving ideal MHD equations on triangular meshes. *preprint, arXiv:1110.0860*, 2011.

[81] S. Yakovlev, L. Xu, and F. Li. Locally divergence-free central discontinuous Galerkin methods for ideal MHD equations. *J. Comput. Sci.*, 4(1):80–91, 2013.

[82] K.S. Yee. Numerical solutions of initial boundary value problems involving Maxwell's equations in isotropic media. *IEEE Trans. Antennas Propag.*, AP-14:302–307, 1966.

[83] A.L. Zachary, A. Malgoli, and P. Colella. A higher-order Godunov method for multidimensional ideal magnetohydrodynamics. *SIAM J. Sci. Comput.*, 15:263–284, 1994.

[84] X. Zhang and C.-W. Shu. On positivity preserving high order discontinuous Galerkin schemes for compressible Euler equations on rectangular meshes. *J. Comput. Phys.*, 229:8918–8934, 2010.

[85] U. Ziegler. A central-constrained transport scheme for ideal magnetohydrodynamics. *J. Comput. Phys.*, 196(2):393–416, 2004.